UNIVERSITÀ DEGLI STUDI DI UDINE

DOCTOR OF PHILOSOPHY THESIS

Dottore di Ricerca dell'Università di Udine

Dipartimento di Ingegneria Elettrica, Gestionale e Meccanica
Corso di Dottorato in Ingegneria Industriale e dell'Informazione, XXIV ciclo

Andrea MICELLI

3D sensors for the Insertable B-Layer of the ATLAS experiment at the CERN LHC

Tutors:
Luca SELMI
Marina COBAL

Jury
Prof. Roberto RINALDO, President
Prof. Cinzia Da VIA, Referee
Dr. Claudia GEMME, Referee
Prof. Luca SELMI, Tutor
Prof. Marina COBAL, Tutor

Università degli Studi Di Udine

Tesi di Dottorato di Ricerca

Per ottenere il titolo di

Dottore di Ricerca dell'Università di Udine

Dipartimento di Ingegneria Elettrica, Gestionale e Meccanica
Corso di Dottorato in Ingegneria Industriale e dell'Informazione, XXIV ciclo

Andrea MICELLI

3D sensors for the Insertable B-Layer of the ATLAS experiment at the CERN LHC

Commissione esaminatrice
Prof. Roberto RINALDO, Presidente
Prof. Cinzia Da VIÀ, Esaminatrice
Dr. Claudia GEMME, Esaminatrice
Prof. Marina COBAL, Tutor
Prof. Luca SELMI, Co-Tutor

to my family

Sommario

Gli studi realizzati e presentati in questa tesi di dottorato, iniziata nel 2009, sono stati possibili grazie alla collaborazione tra il laboratorio di ricerca CERN in Svizzera, l'Università degli Studi di Udine, l'INFN (Istituto Nazionale di Fisica Nucleare) di Udine e Genova e il gruppo di ricerca ATLAS sui sensori 3D.
Scopo principale del CERN è quello di fornire gli strumenti necessari ai ricercatori operanti nel campo della fisica della alte energie. Questi strumenti sono gli acceleratori, che portano le particelle ad una velocità prossima a quella della luce e le fanno poi collidere per produrre altre particelle attraverso la trasformazione dell'energia in massa. I rivelatori, costruiti nei punti di collisione, permettono di ricostruire ed identificare le nuove particelle così prodotte (già conosciute e classificate o ancora sconosciute).

Al momento il più potente acceleratore è il Large Hadron Collider (LHC) il quale collide protoni contro protoni ed attualmente funziona a un'energia di 7 TeV nel centro di massa, ma è previsto raggiungere i 14 TeV[1]. LHC è in funzione dal 2009 è l'obiettivo principale di scoprire il bosone di Higgs (una nuova particella prevista dal Modello Standard[2]) ed in generale nuova fisica oltre quella già conosciuta. Uno degli esperimenti all'LHC è l'esperimento ATLAS. ATLAS è localizzato in uno dei quattro punti in cui avvengono le collisioni ed è costituito da vari sotto-rivelatori in forma di cilindri concentrici, ognuno con lo scopo di identificare e misurare un certo tipo particelle. La parte più interna è chiamata rivelatore a Pixel Detector ed è dedicata al tracciamento delle particelle cariche. Questo rivelatore è il più vicino al punto di collisione dei fasci, e sarà soggetto ad una elaborata esposizione a radiazione. A causa dell'assorbimento di questi alti livelli di radiazione, le performance del B-Layer (uno dei tre strati di sensori al silicio di cui è composto il rivelatore a Pixel) diminuiranno. Si dorvà quindi introdurre un layer addizionale di Pixel di Silicio (Insertable B-Layer o IBL). Le tre tecnologie inizialmente proposte per il progetto di upgrade del rivelatore a Pixel, pianificato per il 2013 sono state: diamante, planare e 3D. Con la sensor review di Luglio si è proposto di costruire un rivelatore misto planare (75%) e 3D (25%).

Il lavoro di questa tesi è concentrato sui sensori 3D proposti per il progetto IBL. In particolare, il candidato ha dato un contributo significativo alle misure di laboratorio per caratterizzare le performance dei sensori con l'elettronica di lettura. Queste misure, insieme ai test eseguiti su fascio, è stato un importante

---

[1] 1 TeV = 10^{17} eV.

[2] Il Modello Standard è una teoria che descrive i principali componenti della materia e le loro interazioni.

passo per definire le
performance dei vari sensori. La tesi è divisa in quattro parti principali:

Parte I (Cap. 1, 2)

Nel primo capitolo vengono introdotti i semiconduttori, la giunzione p-n, il design dei sensori usati per costruire rivelatori di particelle negli esperimenti agli acceleratori ed il loro principio di funzionamento. Il secondo capitolo introduce il laboratorio CERN e gli esperimenti presenti all'acceleratore LHC. Una sezione separata è dedicata all'esperimento ATLAS, ed in essa vengono illustrati i dettagli sulla sua parte più interna, il rivelatore a Pixel.

Parte II (Cap. 3, 4)

La seconda parte introduce il progetto IBL, con le motivazioni alla sua base. Una sezione dedicata descrive la nuova elettronica e le tecnologie di sensori proposti per lo sviluppo di questo progetto. La sezione sui sensori riassume due delle tipologie di sensori pensate per l'IBL (diamante e planare), mentre i rivelatori al silicio 3D sono descritti nel quarto capitolo. All'interno di questo capitolo si riporta un breve sommario sulla storia dell'evoluzione dal progetto originale proposto da Parker et al. nel 1997. Sono inoltre descritte le caratteristiche, i vantaggi e gli svantaggi di questa nuova tecnologia. In particolare, vengono descritti con maggior dettaglio i due layout, proposti rispettivamente dai centri di ricerca FBK di Trento e CNM di Barcellona. Alla fine del Capitolo 4 viene presentata una lista dei sensori sui quali il candidato ha effettuato le misure di caratterizzazione.

Parte III (Cap. 5, 6, 7)

Questa parte è il cuore della tesi: nel Capitolo 5 vengono descritte le misure e gli studi di laboratorio, il software e l'hardware impiegato. Gli studi sul Front-End FE-I4 ed i risultati per il lotto 3D ATLAS09 (fabbricato a Trento). Questo lotto è stato usato per fornire le informazioni e presentare i risultati alla riunione ATLAS Sensor Review istituita, per prendere la decisione finale su quale tipo di tecnologia usare per costruire l'IBL. I risultati presentati nel capitolo sono stati utilizzati dalla comunità 3D di ATLAS per dimostrare che questa tecnologia era finalmente pronta e rappresentava un buon, se non il migliore, candidato per il progetto IBL.
Il Capitolo 6 descrive i risultati ottenuti ai test su fascio nel 2011. I principali parametri studiati sono stati l'efficenza, la raccolta di carica e la dimensione dei cluster.
Infine, nel Capitolo 7, si riportano le conclusioni assieme ad un riassunto del lavoro fatto per la Sensors Review di Luglio 2011 e per la riunione dell'esperimento ATLAS in Giugno e Settembre.

Summary

The studies presented in this PhD thesis has been possible thanks to a collaboration started among several groups: the CERN research laboratory in Switzerland, the University of Udine, the INFN (Istituto Nazionale di Fisica Nucleare) of Udine and Genova, and the ATLAS 3D Sensors Collaboration. CERN provides the tools needed by researchers in the field of high-energy physics. These tools are the accelerators, which lead particles to speeds close to the light speed and then make them collide, to produce other particles via the transformation of energy in mass. Detectors, built around the collision points allow the scientists to reconstruct and identify the new particles produced (already known and classified or unknown). Currently, the most powerful accelerator is the Large Hadron Collider (LHC), which collides protons agains protons actually at a center of mass energy of 7 TeV, but it is planned to reach 14 TeV[3]. LHC is running since 2009, with the main goal to discover the Higgs boson (a particle needed to complete the Standard Model[4]) and in general new physics beyond the one already known. One of the detectors at the LHC is the ATLAS experiment. ATLAS is located in one of the four collision points, it is made of various sub-detectors in the form of concentric cylinders, each one with the task of identifying and measure a certain type of particles, and the innermost part of it is the Pixel Detector dedicate to the charged particles tracking. This detector is the closest to the interaction point of the beams, and it will be subject to a high radiation exposition. Due to the quantity of radiation levels, the performance of the B-layer (the innermost one of the three layers of sensors of Silicon pixels which form the Pixel Detector) will decrease. Therefore, it will be necessary to add a new additional layer of Pixel Silicon (Insertable B-Layer o IBL). The three technologies initially proposed for the Insertable B-Layer (IBL) project, which is the upgrade of the Pixel Detector planned for 2013, during the LHC stop, were: diamond, planar and 3D sensors. With the sensor review of July it was proposed to build a mixed detector with planar (75%) and 3D (25%) sensors.

The work of this thesis is centered on the 3D sensors proposed for the IBL. In particular, the candidate has given a significant contribution to the laboratory measurements for the characterization of the sensors performance with the read-out electronics. These measures, together with the beam tests perfumed by the candidates, was an important step to define the sensor performances. The thesis is divided into four main parts:

---

[3] 1 TeV = 10^{17} eV.

[4] The Standard Model is a theory that describes the main components of matter and their interactions.

Part I (Chapters 1, 2)

The first chapter gives a general overview of the semiconductors, the p-n junction, the designs used to built detectors and the base principles on how they work.
The second chapter introduces the CERN laboratory and the experiments inside the LHC proton-proton collider. A separate Section is dedicated to explain the ATLAS experiment providing a detailed description of its innermost detector, the Pixel Detector.

Part II (Chapters 3, 4)

The second part introduces the IBL project with the motivations behind the request to have an upgrade (a new additional layer) for the Pixel Detector. A section is dedicated to the description of the new electronics and sensors technologies proposed for the development of such a project. The section on the sensors gives a summary of the two technologies, diamonds and planar, while the 3D pixel silicon sensor technology is discussed in details in Chapter 4. Inside this Chapter, a brief summary of the history of the evolution of the 3D design originally proposed by Parker et al. in 1997, is given. In addition, the main features of the design and the advantages and disadvantages of this type of sensors are given. In particular, the two layouts proposed by the fabrication facilities FBK in Trento and CNM in Barcelona, are discussed. At the end, a list of sensors measured by the candidate is presented.

Part III (Chapters 5, 6, 7)

This is the heart of the thesis: Chapter 5 describes the laboratory studies, the hardware and software setup, the studies of the Front-End FE-I4 and the results of the 3D ATLAS09 batch (fabricated in Trento). This batch was used to provide the informations and results to be shown at the ATLAS Sensor Review for the final decision on which sensor technology will have to be used to built up the IBL. The results presented in this Chapter were all used by the ATLAS 3D community to prove that the 3D sensor technology is finally a good candidate for the IBL project. Chapter 6 describes the beam test's results obtained in 2011. The main parameters studied have been the efficiency, the cluster charge and cluster sizes. At the end, in Chapter 7, the conclusions are presented, together with a summary of the work done to present the results in time for the Sensor Review on July 2011 and for the ATLAS experiment decision board in June and September 2011.

Contents

List of Figures

List of Tables

Chapter 1

Introduction

1.1 Semiconductors

Compared with other materials, semiconductors have unique properties, very suitable for the detection of ionizing particles. In particular Silicons are widely employed to build electronic materials and devices devoted to this task. Even, the existing process technology can be exploited for these detectors production. The intrinsic properties of some semiconductors material are summarized in Table 1.1 [1]. As an example, the small band gap or (Energy gap, E_g) equivalent to 1.12 eV at room temperature for Silicon (Si), leads to a large number of charge carries per unit energy lost from the ionizing particle to be detected. The average energy needed to create an electron-hole pair, equal to 3.6 eV, is an order of magnitude smaller than the ionizing energy of the gases, around 30 eV. Thanks to the Silicon high density (ρ=2.33 g/cm^3), it is possible to produce thin detectors which still give rise to a large enough signal to be measured. The mobility of the electrons (μ_e), 1350 cm^2/Vs, and holes (μ_p), 450 cm^2/Vs, allows them to move quite freely. As a consequence, charges can be collected rapidly in a time of order of 10 ns, allowing their use in a very high rate environment. The good mechanical rigidity allows the construction of self-supporting structures useful to decrease the size of the devices.

By doping the crystal, it is possible to create a fixed space charge: this is not possible when using gas detectors. Thanks to this advantage it is possible to create sophisticated field configurations without limiting the movement of the signal charges.

Other most commonly used semiconductor materials are Germanium (Ge) but also compound materials like GaAs, while for specifics purpose, such as operations at room temperature and radiation hardness requirements materials with larger band gap are used. For example, diamond belong to this category and it is an excellent candidate for high-speed application thanks to its high electrons and holes mobility. A separate discussion on diamonds can be found later in Section 3.4.2.

Material	Si	Ge	GaAs	Diamond
E_g [eV]	1.12	0.67	1.42	5.5
E_{ion} [eV]	3.6	2.96	4.2	13
ρ [g/cm^3]	2.33	5.33	5.32	3.52
Z	14	32	31-33	6
τ [s]	>5000	>5000	≈0.001	≈300
μ_e [cm^2/(Vs)]	1350	3900	8000	1800
μ_h [cm^2/(Vs)]	450	1900	400	1200

Table 1.1: Intrinsic properties of few selected semiconductors at T=300 K [1]: E_g is the energy gap, E_{ion} the ionization energy, ρ the density, Z the atomic number, τ the lifetime, μ_e the electron mobility and μ_h the hole mobility.

1.2 The pn Junction

A p-n, or pn junction, is the elementary structure, or better the building block, of most semiconductor electronic devices such as diodes, transistors, solar cells, integrated circuits and detectors. It is the basic element to understand semiconductor detectors and the most important electronic structure. A pn junction is obtained by joining together two opposite regions homogeneously doped with p-type and n-type[1]. Initially, at thermal equilibrium, without an external voltage applied, a potential difference is present across the junction. After joining the two regions, electrons near the pn interface tend to diffuse into the p-type region likewise holes diffuse into the n-type region. As a consequence, there is a surplus of negative charge in the p-region and of positive charge in the n-region since electrons and holes recombine with the majority carriers producing a depleted region, free of charge carries, close to the junction. This creates an electric field which counteracts the diffusion and the so-called built-in voltage V_{bi}. Any movement of charge carries is presented in the region by the electric field so that a space charge region is obtained. In Figure 1.1 the charge, electric field and voltages curves are illustrated. Considering an abrupt pn junction case, with constant concentration on both sides, the V_{bi} is expressed by Formula 1.1[2] and can be simplified as:

$$V_{bi} = \frac{KT}{q} ln\left(\frac{n_{0,n}n_{0,p}}{n_i^2}\right) = V_{TH}\, ln\left(\frac{N_A N_D}{n_i^2}\right) \tag{1.1}$$

where $V_{TH} = KT/q$[3] is the thermal voltage (K is the Boltzmann constant, T is the absolute temperature of the pn junction in Kelvin, and q is the electron charge), $n_{0,n}$, $n_{0,p}$ are the electron concentrations in the n-type region and hole concentration in the p-type region respectively, and n_i is the intrinsic semicon-

---

[1] A p-type, p for Positive (n-type, n for Negative), semiconductor is obtained by carrying out a process of doping by adding a certain type of atoms called acceptors (donors) to the semiconductor in order to increase the number of free charge carriers positive holes, for p-type and negative electron for n-type case).

[2] Derived from the difference of the Fermi potentials between the n- and p- doped material.

[3] approximately 25.85 mV at 300 K.

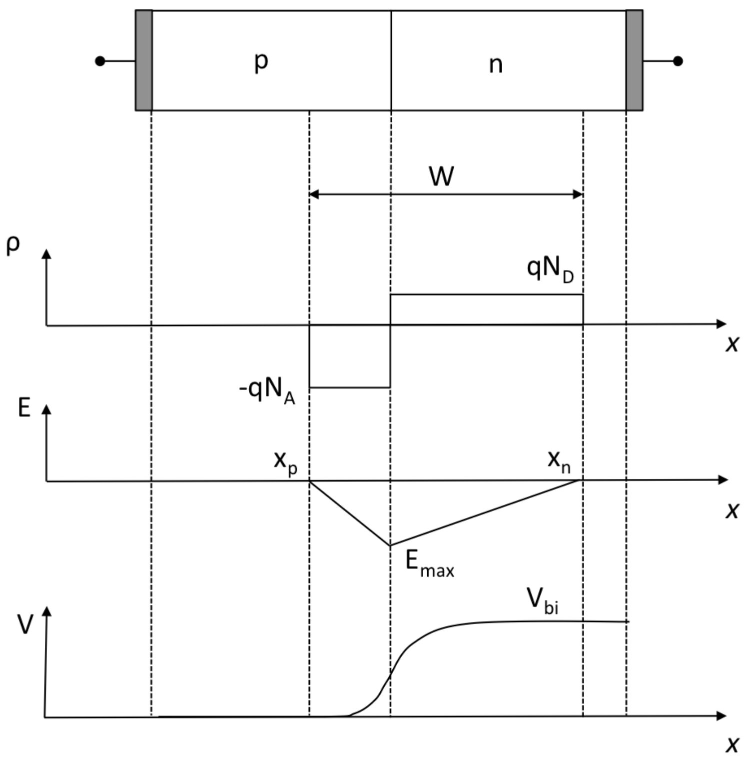

Figure 1.1: Sketch of a pn junction. From the top: structure, charge density ρ, electric field E and voltage V. The graphics are not in scale.

ductor concentration[4]. Assuming that these two concentrations are equal to the the concentrations of donors N_D and acceptors N_A[5]. The V_{bi} for Silicon is about 0.7 V.
The system, as it represented in Figure 1.1, is in thermodynamic equilibrium but an external voltage could be applied to the two terminals of the junction. Then, the carriers charge and the current flow depends on the polarity and on the external voltage value applied to it. There are then two cases: forward bias and reverse bias voltage, which will be discussed in the next sections.

1.2.1 Forward bias

If a positive voltage is applied to the p-type region, while the n-type region is negatively biased, the pn junction is under a forward bias (see Figure 1.2 left). In this case, the depletion width decreases: the minority carriers in each region

---

[4] The concentration of dopant introduced in an intrinsic semiconductor determines its concentration and indirectly affects many of its electrical properties. In an intrinsic semiconductor under thermal equilibrium, the concentration of electrons and holes is equivalent ($n = p = n_i$). In a non-intrinsic semiconductor in thermal equilibrium the relation becomes $n_0 \cdot p_0 = n_i^2$ (mass-action law) where n_0 is the concentration of conducting electrons, while p_0 is the electron hole concentration.

[5] Donors: atoms from the group V, of the periodic table of the elements, which gives one electron; acceptors: atoms from the III group of the periodic table of the elements, which accepts one electron.

increase, and the current flows from the p-region to the n-region. The electrons present in the p-region are attracted to the positive terminal of the power supply creating new holes; in addiction, electrons from the negative terminal go to the n-type region and diffuse through the junction.

1.2.2 Reverse bias

If a positive external voltage is applied to the n-type region, the diode is under a reverse bias. The free electrons are attracted from the n-type region to the positive terminal of the power supply, far away from the junction. At the same time, holes are moved away from the junction, causing a wider depletion region, and a larger space charge region with a larger built-in potential across the junction. The flowing current, called inverse current, is weak due to the fact that is transported only by minority carriers. In physics applications, this situation is the most interesting one, important to detect particles since a depleted zone as wide as possible is created in order to increase the sensitive part of the structure.

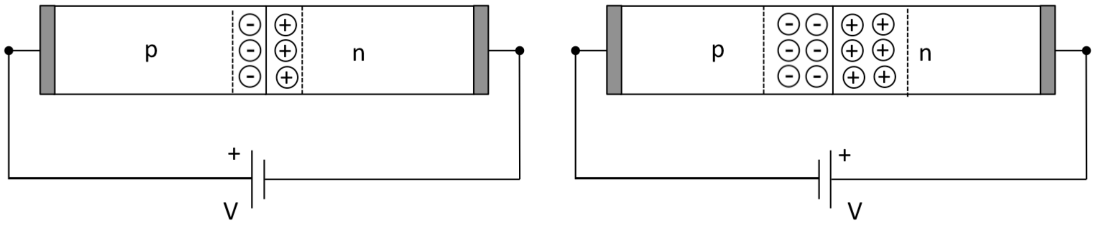

Figure 1.2: The pn junction biasing: forward bias (left), reverse bias (right).

The depletion width (W), the potential and the electric field for this case can be calculated by solving the Poisson Equation 1.2, where ρ^6 represents the charge density and ϕ the electric potential field, in one-dimension, applied to the diode structure as shown in Figure 1.2:

$$\nabla^2\phi = -\frac{\rho}{\epsilon} \tag{1.2}$$

and considering a constant doping and an abrupt junction the maximum value of the electric field is:

$$E_{max} = q\frac{N_D}{\epsilon_0\epsilon_{Si}}x_n = q\frac{N_A}{\epsilon_0\epsilon_{Si}}x_p$$

therefore, W is:

$$W = x_n + x_p = \sqrt{\frac{2\epsilon_0\epsilon_{Si}}{q}\left(\frac{1}{N_A} + \frac{1}{N_D}\right)(V + V_{bi})} \tag{1.3}$$

---

[6] $\rho = q(N_A - N_D + p - n)$

with V being the external applied voltage, ϵ_0 and ϵ_{Si} the absolute and relative dielectric constant[7], x_n (x_p) the depletion zone for the n-zone (p-zone) part, and W the total width of the depleted zone. In Silicon sensors the junction is usually realized by a shallow and high doped p^{+}[8] implant in a low-doped bulk material ($N_A > 10^{18}$ cm^{-3}, $N_D \approx 10^{12}$ cm^{-3}), see [2] for more details. Taking this into account, $1/N_A$ is negligible and the expression in Equation 1.3 becomes:

$$W \approx x_n \approx \sqrt{\frac{2\epsilon_0\epsilon_{Si}}{qN_D}V}, \;\; N_A \gg N_D \tag{1.4}$$

while in the other case:

$$W \approx x_p \approx \sqrt{\frac{2\epsilon_0\epsilon_{Si}}{qN_A}V}, \;\; N_D \gg N_A$$

The meaning behind this simplification is that the space charge region or the depletion zone increase much more where the doping is lower (as shown for example in Figure 1.1). Moreover, the total depletion zone depends on the external voltage V: W increases when the applied voltage V is raised (once again in reverse bias) and it reaches a maximum value after which the junction breaks down and becomes conductive (breakdown zone). Introducing the conductivity σ and, more important, the resistivity ρ[9], which is an important parameter to characterize doped silicons:

$$\sigma \equiv \frac{1}{\rho} = qn\mu_e \quad \text{for electrons}$$

$$\sigma \equiv \frac{1}{\rho} = qp\mu_p \quad \text{for holes}$$

where n (p) is the electrons (holes) concentrations. The resistivity for pn junction with reverse bias is then equal to:

$$\rho = \frac{1}{qN_D\mu} \quad \text{under the hypothesis} \quad N_A \gg N_D$$

where ρ depends on the dopant density N_D and on the majority carrier mobility μ and of course on the charge q. The total width of the depleted zone, W, can be expressed as:

$$W \approx x_n \approx \sqrt{2\epsilon_0\epsilon_{Si}\rho V}$$

Another important parameter for a pn junction in a reverse bias condition is

---

[7] $\epsilon_r = 12$ for Silicon

[8] With p^+ (n^+) it will refers to a material doped with acceptors (donors) to create an abundance of holes (electrons).

[9] please note the different meaning of the previous definition of charge density which has the same symbol ρ.

its capacitance, which can be defined, as for two parallel plates capacitor with electrode distance equal to W (once again assuming 1/N$_A$ negligible) as in the following:

$$C = \frac{\epsilon_0 \epsilon_r}{W} \approx \frac{2\epsilon_0 \epsilon_r}{\sqrt{\frac{2\epsilon_0 \epsilon_{Si}}{qN_D} V}} \tag{1.5}$$

One can see that the capacitance is inversely proportional to the square root of the bias voltage and it depends on the doping concentration N$_D$.

1.3 Semiconductor Silicon Detectors

Semiconductor Silicon detectors behave like a *ionization chamber*, with a simple configuration medium, the semiconductor in pn junction configuration, with two strong doped p$^+$ and n$^+$ electronics on the opposite sides, placed in a n-bulk substrate as shown in Figure 1.3. Applying to the structure an external power supply in a reverse configuration, the depletion zone starts to grow from the junction into the bulk thanks to the electrons. The positive voltage is connected to the n$^+$ electrode which creates an inverse polarization of the pn junction. An electric field and a depleted zone, free of charge, is consequently created between the two electrodes. The basic concept behind the Silicon detectors is the following: when a particle pass through the material, it generates charge carries which, under the effect of the electric field, drift to the respective electrodes. Holes go to the cathode (p$^+$ electrode) while electrons to the anode (n$^+$ electrode) and this effect produces the signal which is read out from a preamplifier connected to the n$^+$ electrode. Such sensors are not able to measure the position of the particle precisely. If spatial information is to be obtained, one of the electrodes, or both, have to be segmented (see Section 1.6 for more details).
For Silicon detectors it is enough if the crossing particle releases an energy equal to 3.6 eV (see Table 1.1), to create an electron-hole pair. This energy can be much lower than the one for ionizing a gas (i.e. ~30 eV). Another advantage in this kind of detectors is that the signal is larger and directly proportional to the released energy [3]. The average energy lost by the particle can be calculated by the Bethe-Bloch formula, see Section 1.5.

As soon as a charge starts to move through the junction, the induced charge on the electrodes changes continuously, creating a current (and not when the charges reach the respective electrodes as one might think). The induced current intensity depends on the coupling between the charge and the electrodes and it is given by the Ramo's theorem [4]. The instantaneous current is:

$$i(t) = -q\vec{v}(t) \cdot \vec{E}_w \tag{1.6}$$

where q is the charge moving under the electric field with velocity $\vec{v}(t)$ and $\vec{E}_w$ is the weighting field. Taking as an example the structure sketched in Figure 1.3, a Silicon geometry of a diode structure which is the simplest detector configuration, with two electrodes at a distance d, the carrier velocity is:

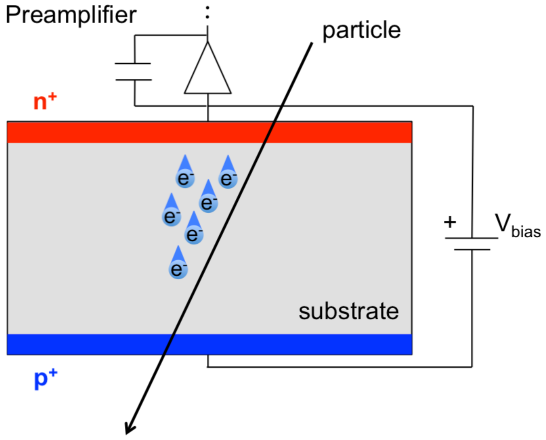

Figure 1.3: Sketch of a silicon detector geometry.

$$v_e = \mu_e E = \mu_e \frac{V_{bias}}{d}, \qquad v_h = \mu_h E = \mu_h \frac{V_{bias}}{d},$$

This is true under the hypothesis of having a constant electric field E between the electrodes, equal to $E = V_{bias}/d$ and with a bias voltage high enough to full deplete the substrate. The weighting field is constant and equal to $E_w = 1/d$ for both electrodes. Therefore, the current is constant until the charge arrives to the electrodes:

$$i = qvE_w = q\mu \frac{V_{bias}}{d^2} \tag{1.7}$$

Assuming that an electron-hole pair is generated at a certain position x, taking the starting point (origin of the coordinate system) at the positive p^+ electrode, due to the opposite movement and opposite charge sign, the total charge induced by electrons and holes is:

$$Q_e = it_e = q_e \frac{x}{d}, \qquad Q_h = it_h = q_e \left(\frac{d-x}{d}\right) = q_e \left(1 - \frac{x}{d}\right)$$

with an electrons and hole collection time equal to:

$$t_e = \frac{x}{v_e} = \frac{xd}{\mu_e V_{bias}}. \quad \text{Consequently,} \quad t_h = \frac{d-x}{v_h} = \frac{(d-x)d}{\mu_e V_{bias}}$$

As expected, the total induced charge depends on the electron charge q_e but also on where the charge has been generated. In fact, if the charge is generated close to a positive (negative) electrode, a hole (electron) will be collected instantaneously inducing a negligible signal, while all the signal will be produced by the electron motion (or hole, in the other case). For example, if a particle hits the substrate at $x = d/2$, after a time $t_e = d^2/(2\mu_e V_{bias})$ the electrons induce a charge $Q_e = q_e/2$ while the holes, due to the reduced mobility $\mu_h \approx \mu_e/3$, induce a charge equal to $Q_h = q_e/6$. All this corresponds to a total charge of (electrons and holes) $Q_{TOT} = 2/3q_e$, and after a time $(t_e - t_h)$ the remaining charge $q_e/3$ will also be collected. In conclusion, both electrons and holes contribute equally to the current on both electrodes, where at any time the current is the same (even if of opposite sign). Another derived parameter which is useful to describe the simplest diode configuration is the depletion voltage, which can be deduced using Equation 1.4 and expliciting in V:

$$V_{depl} = \frac{eN_D d^2}{2\epsilon_0 \epsilon_{Si}}. \tag{1.8}$$

This is for an very simple sensor which is completely different from the case of complex silicon detectors, but it gives a good estimate of the fundamental sensor properties. In fact, V_{depl} in first approximation depends on the sensor thickness and on the substrate doping N_D. However, a better estimate could be performed with a capacitance voltage measurement (CV-measurement): for a complete description of this, see [2] for more details. Using the definition of V_{depl}, the capacitance as a function of V_{depl} becomes:

$$C(V_{bias}) = \begin{cases} \sqrt{e\epsilon_0\epsilon_{Si}\dfrac{N_D}{V}}, & \text{for} V_{bias} < V_{depl} \\ \\ \dfrac{\epsilon_0\epsilon_{Si}}{d}, & \text{for } V_R > V_{depl} \end{cases} \tag{1.9}$$

Therefore, an increase of the reverse bias voltage has the effect to increase the thickness of the depletion zone and, on the contrary, to reduce the capacitance of the sensitive area. This will have as a consequence an increase of the signal-to-noise ratio (S/N) as it will be reported in Chapter 5 (Section 5.4.5).

1.4 Current and Voltage Characteristic of a Silicon Sensor - PN-Junction

A diode functionality is described via its current-voltage (IV) characteristic, or IV graph. Figure 1.4 illustrates the progress of the current (I), as a function of the voltage (V) applied between the n^+ electrode (cathode) and the p^+ electrode (anode, with the same polarity as the built-in potential). The IV curve is taken in the absence of external effects like light or particles crossing the diode (the sensor is put in the dark) that can affect the measurement, and only a power supply is applied in a reverse voltage condition. Three different areas can be distinguished: a volume of generation, a surface of generation and an avalanche breakdown zone. As Figure 1.4 shows, the current increases with the voltage raising.

For applied voltages lower than the full depletion voltage (V_{depl}) the IV measurement is in the forward bias region and follows an exponential behavior. If the applied voltage is instead above V_{depl}, the measured IV is in the reverse bias region. Increasing to higher voltages, after full depletion, there is a plateau region where the current slowly increases until the applied voltage reaches the V_{max} value, after which there is the breakdown at high voltages. This value depends on the particular junction used and can not be defined without performing the IV

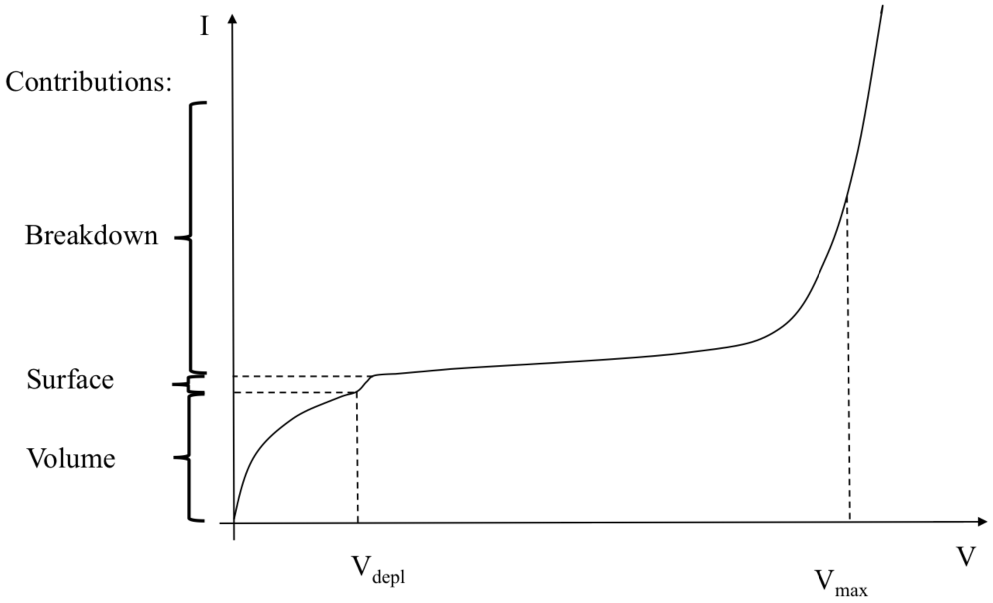

Figure 1.4: Typical current - voltage (IV) trend for a reverse bias voltage applied to the sensor. On the y-axis, the origin of the different current contributions are indicated.

measurement. The V$_{max}$ values is identified when a high electric field is present together with a current smoothly increasing.

Now, if the voltage values become higher, the current increases very fast and at some point could cause the destruction of the junction and the device (note that Figure 1.4 illustrates just an example and it is not in scale). To guarantee a good working point, in a reverse bias condition, the bias voltage has to be always below this critical value[10]. The IV measurement is an important test to study how the sensor behaves, and a lot can be understood from it as it will be discussed in Section 5.5.2.

1.5 Passage of Charged Particles Through Matter

When a charged particle enters a medium, it will interact with the medium electrons and nuclei and begin to loose energy as it crosses the material. It is useful to describe the energy loss per unit distance travelled by the charged particle, and the range of the particle in various material. Particles can be divided in two categories: 'heavy' and 'light'. A charged particles is called heavy if its rest mass is large compared to the rest mass of the electron: alpha-particles and of course fission fragments are all heavy charged particles. Instead, electrons and positrons are light particles.

The Bethe-Bloch formula gives the rate of ionization loss for a charged particle in a medium [1]:

---

[10] In this thesis, starting from this Section, the convention is to have a positive voltage applied for a reverse bias case, while for a forward bias the voltage is negative.

$$\frac{dE}{dx} = 2\pi N_0 r_e^2 m_e c^2 \rho \frac{Z}{A}\frac{z^2}{\beta^2}\left[ln\left(\frac{2m_e\gamma^2 v^2 W_{max}}{I^2}\right) - 2\beta^2 - \delta - 2\frac{C}{Z}\right] \tag{1.10}$$

where Z on A represents the matter dependence, $\delta(\beta\gamma)$ is a coefficient which

$\frac{dE}{dx}$	particle energy loss usually given in $\frac{eV}{g/cm^2}$
$2\pi N_0 r_e^2 m_e c^2$	$0.1535 MeV c^2/g$
x	path length in g/cm^2
r_e	$\frac{e^2}{4\pi m_e c^2} = 2.817 \times 10^{-13}$ cm and is the classical electron radius
m_e	electron mass: $\sim 9.11 \times 10^{-31}$ kg
N_0	Avogadro's number: $6.022 \times 10^{23} mol^{-1}$
I	effective ionization potential averaged over all electrons (137eV for Si)
Z	atomic number of the medium (14 for Si)
A	atomic weight of the medium (28 for Si)
ρ	density of the medium
z	particle charge
β	v/c, the velocity of a traversing particle in units of speed of light
γ	$\frac{1}{\sqrt{1-\beta^2}}$
δ	density correction
C	shell correction
W_{max}	maximum energy transfer in a single collision

Table 1.2: Parameters in the Bethe-Bloch formula.

reduces the dE/dx for high value of $\beta\gamma$, while β^2 is the dependence form the cross section from the natural energy decreasing with the decrease of the upcoming collisions. Therefore at for low energy the $1/\beta^2$ term in Equation 1.10 and the stopping power decrease with increasing energy. At a particle's velocity β of about 0.96 ($\beta\gamma \approx 3$) a minimum is reached [2]. The term C/Z is associated to the electrons shielding when, at low energy, electrons cannot be considered free. All the symbols are summarized in Table 1.2, and the dE/dx dependence is showed in Figure 1.6 which shows the energy loss for a muon traveling in Cu. For $\beta\gamma$ values < 0.007, the Bethe-Bloch formula is not valid anymore: the particle has a speed almost equal to that of the electrons and it will be absorbed. For $0.007 < \beta\gamma < 1$ the energy is dominated by the $1/\ \beta^2$ factor while for $1 < \beta\gamma < 4$ the decrease is compensated by the logarithmic term. For $4 < \beta\gamma < 200$ the energy loss increases as $\ln(\beta\gamma)$. Then, for $\beta\gamma > 200$ it reaches a constant value, the so-called Fermi plateau. For high-energy relativistic particles the logarithmic slope is ∼10% compared to the value of the minimum, so the minimum value of dE/dx is associated with a wide range of $\beta\gamma$. The energy loss rate as a function of the particle energy is shown in Figure 1.5. The energy E and velocity of a particle with mass M are related by relativistic kinematic according to the formula:

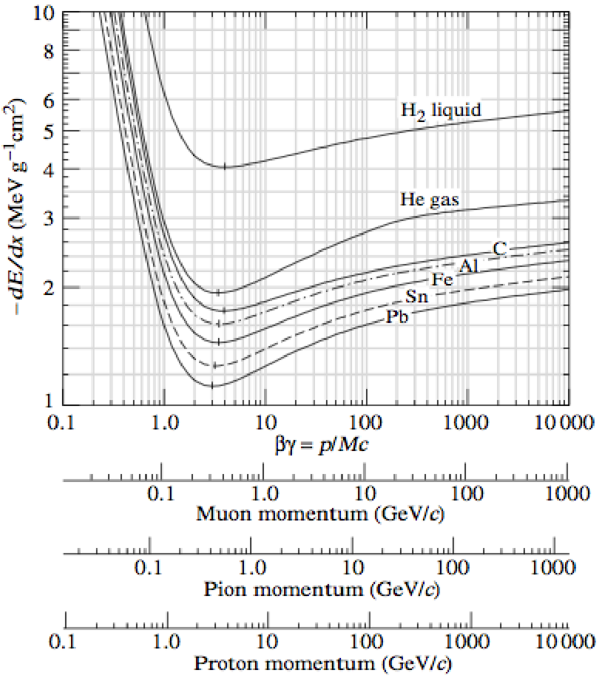

Figure 1.5: Energy loss by different heavy charged particles in different materials as a function of their momentum: Bethe-Bloch-graph.

$$E = \gamma M c^2 = \frac{Mc^2}{\sqrt{1-\beta^2}}, \quad \text{with} \quad \beta = \frac{v}{c}$$

which for small velocities reduces to $E_{kin} = E - Mc^2 = Mc^2/2$. The maximum energy transfer produced by a head-on collision is given by:

$$W_{max} = \frac{2m_e c^2 \beta^2 \gamma^2}{1 + 2\sqrt{1+\beta^2\gamma^2} + s^2}, \quad \text{with} \quad s = \frac{m_e}{M}$$

which for $M \gg m_e$, becomes $W_{max} \approx 2m_e c^2 \beta^2 \gamma^2$.
A particle with an energy loss in the minimum of the Bethe-Bloch formula is called *minimum ionizing particle* (m.i.p. or MIP). The value of the minimum depends on the square of the particle charge but very weakly on the particle mass. Due to the flatness of the curve, this expression is often used also for all particles with $\beta > 0.96$ (or $\beta\gamma > 3$). The number of electrons-hole pairs generated by a traversing particle can be calculate by dividing the deposited energy by the mean energy needed for ionization, w. The difference between w and the band gap generates photons, which in the end will dissipate as thermal energy [2].

The average energy loss in a sample of finite thickness can be calculated from the Bethe-Bloch formula by integration. However, statistical fluctuation about

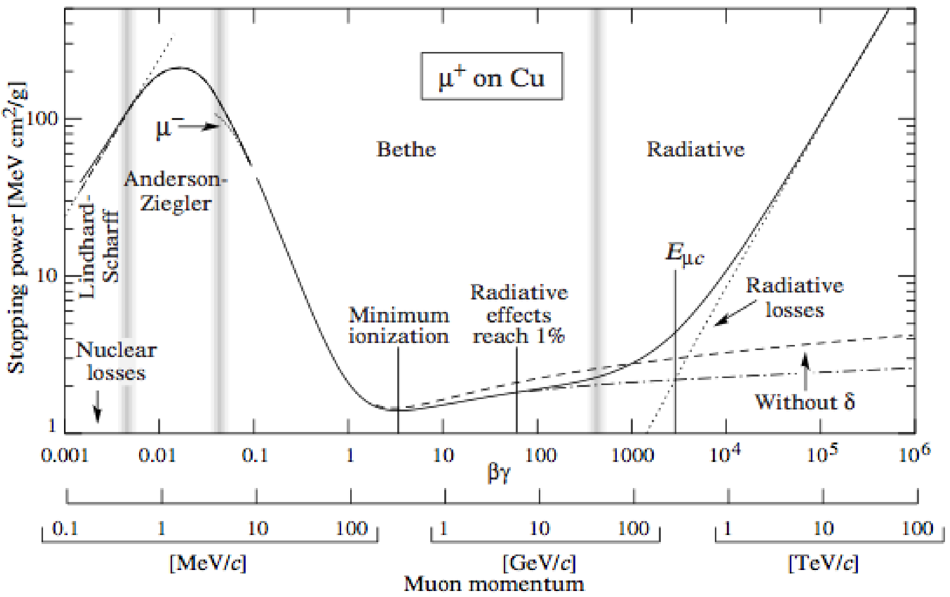

Figure 1.6: Energy loss of muon (μ) crossing a slab of Copper (Cu) as a function of its momentum.

this value have to be taken into account, see Figure 1.7. This problem has been treated in depth by Landau. A review of this subject, including the original discussion and a comparison with data, can be found in [5] and references quoted therein. In semiconductors, only part of the energy loss is used for the creation of electron-hole pairs. In Silicon, the average energy used for the creation of a pair is 3.6 eV, three times larger than the band gap of 1.12 eV. This is true for radiation energies that are large with respect to the band gap.

Landau Distribution
The fluctuations of the energy loss by ionization of a charge particle in a thin layer of matter give rise to an asymmetric probability density function characterized by a narrow peak with a long tail toward positives values (due to the small number of individual collisions) each with a small probability of transferring large amount of energy. The mathematical definition of the probability density function is the so called Landau Distribution as reported in Figure 1.7 which shows a comparison between measured data and the theoretical Landau expectation [6].

Shape of the Ionization Path
A high energy particle which cross the detector, has a constant velocity and produce a uniform ionization along the path. Assuming a detector thickness of 300 μm[11] of Silicon, a signal of about 24000 electrons (Most Probable Value or MPV)

---

[11] 300 μm is the compromise of having enough material (thickness for the standard planar technology) to maintain a good signal efficiency (higher is the inner-electrode distance, higher is the signal detected), and the low material budget required. Indeed, the multiple scattering may cause inefficiency during tracking reconstruction for the outside detectors layers.
For example, using 300 μm of Silicon material, it is aspect to have 24000 e$^-$ (8000 e$^-$ for 100 μm), which is enough charge considering the charge sharing along the neighbor pixel cells.

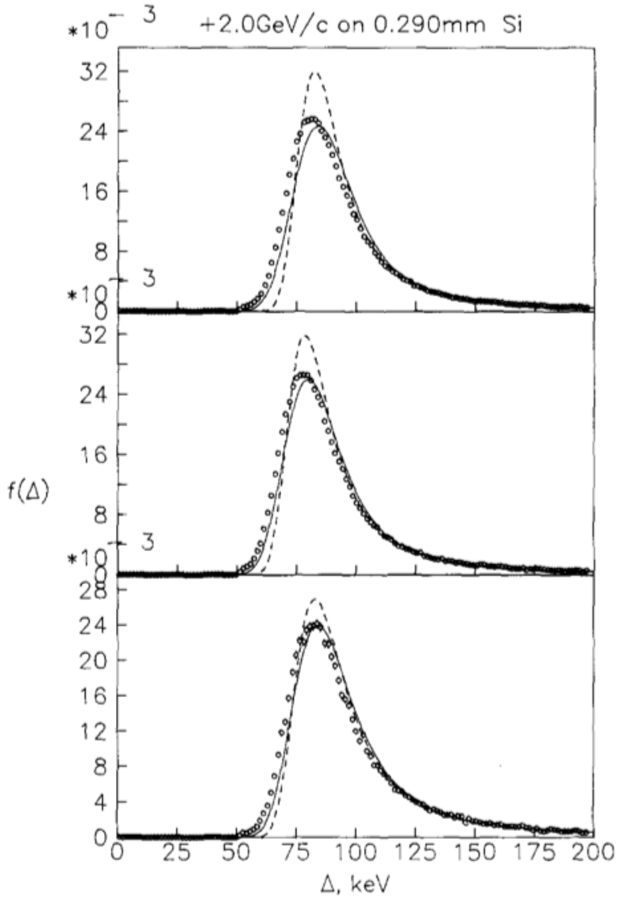

Figure 1.7: From top to the bottom: measured energy loss distribution (points) for 2 GeV/c positrons (top), pions (middle) and protons (bottom) traversing a 290 μm-thick silicon detector. The dashed curves show the theoretical Landau function expectation. For more details see [6].

is generated from a unit charge particle. In about 5 ns, all the charge can be collected, assuming the possibility to, producing a current of order of 1 μA, [2].

1.5.1 Source Measurements

To study the features of a Silicon detector, two types of particles are mainly used: β-particles and γ-particles.

β-particles:

These are high-energy electrons or positrons emitted by certain types of radioactive nuclei. The most common radioactive source to produce β-particles is the Strontium-90, Sr^{90}. Of the three common types of radiation given off by radioactive materials, α (helium nucleus), β and γ (photons[12]), β has an intermediate penetrating and ionising power. The β-particle interaction with matter

---

[12] Decaying types:
γ-decay: it occurs because the nucleus is at too high an energy. The nucleus falls down to a lower energy state and, in the process, emits a high energy photon known as a γ-particle.

generally presents a range which ten times, and an ionizing power which is one tenth, compared to the α-particles. Although β-particles can be produced by different radioactive materials with a different energy, most β-particles can be stopped by a few millimeters of Aluminum. Being composed of charged particles, β-radiation is more strongly ionising than γ-radiation. When passing through matter, a β-particle is decelerated by electromagnetic interactions and may give off bremsstrahlung x-rays[13]. In fact, β-particles are also often used in quality control to test the thickness of an item, such as a paper. Some of the β-radiation is absorbed while passing through the product. If the product is made too thick or thin, a correspondingly different amount of radiation will be absorbed.

In high energy physics applications, β-radiation is used in combination with an external trigger (scintillator) which gives the trigger signal to the acquisition system in order to study how much charge the device under test can collect. More precisely, Sr^{90} undergoes a β-decay with decay energy of 0.546 MeV distributed into an electron, an anti-neutrino and the Yttrium isotope Y^{90}. This isotope undergoes beta decays to an electron, an anti-neutron and zirconium Zr^{90}, which becomes stable by releasing 2.28MeV γ's. Sr^{90} can be considered a pure electron emitter as Y^{90}, but the γ-photon emission from the latter is so weak that it can normally be ignored. We will see that the Silicon detector performances are tested using as source of ionization the $Sr^{9}0$. This will be seen in Chapter 5, Section 5.5.3. The absorption of β-electrons is described via the Bethe-Bloch process.

γ-particles:

A typical γ-particle source is the Americium-241, Am^{241}, which emits γ-particles. Am^{241} decays by emitting an α-particle and gamma radiation to become Neptunium-237. It is used as a portable source of gamma rays and α particles for a number of medical and industrial uses (such as smoke detectors). Am^{241} source emits 60 keV photons, which can convert anywhere in the bulk in a 60 keV primary electron. If the photon emission is completely collected, a signal of 16.5 ke^{-} is expected. Therefore, in charge plot distribution, the higher peak is expected to be at 16.5 ke^{-}[14] Besides Am^{241}, it is possible to use Cd^{109} which emits 22 keV photons with a charge peak at 6.1 ke^{-}. The purpose to use γ-sources is to calibrate the detector as it will be discussed in Section 5.5.3.

β-decay: it occurs when the neutron to proton ratio is too great in the nucleus and causes instability. In basic β-decay, a neutron is turned into a proton and an electron. The electron is then emitted.
α-decay: it occurs because the nucleus has too many protons which produces a high repulsion force.

[13] Bremsstrahlung means 'braking radiation' and is retained from the original German to describe the radiation which is emitted when electrons are decelerated or braked when they are fired at a metal target.

[14] expected due to the noise fluctuation which always intervene in the measurement disturbing the signal.

1.6 Silicon Pixel Detectors: main layouts

The main Silicon detectors can be classified into two main basic geometry layouts: microstrip and Pixel detectors. The difference between the two layouts is the position of the electrodes, where charge is collected, and where the supply voltage is applied. Inside these groups the classification can be furthermore divided based on the different dipping configurations, such as the doping type of the bulk. As a consequence, the performance will be affected in terms of efficiency, resolution, radiation hardness etc. The idea is always the same, as described in Section 1.3, and shown in Figure 1.8: a junction configuration with high doped p^+ and n$^+$ electrodes [7] in a substrate (usually n-type).

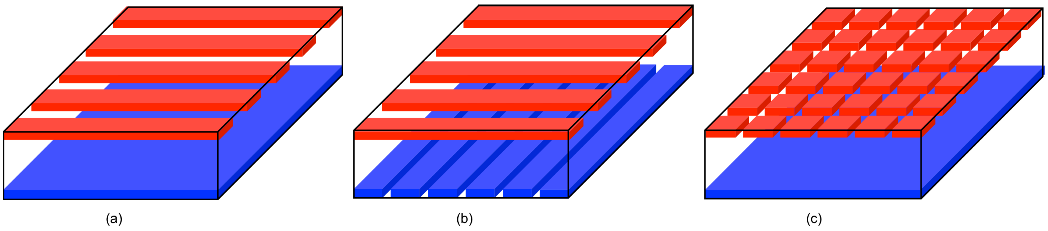

Figure 1.8: Different types of layout for the Silicon Pixel Detector, to improve the space resolution. From the left: (a) single sided strip - 1-Dimensional space coordinate, (b) double sided strip detector (or matrix) - 2D space coordinates (but still with ambiguity issue), and pixel detector (c) - 2D coordinates (reduced ambiguity issue).

The most common and oldest technic gives the so-called single-sided microstrip detector, see Figure (a) 1.8. A microstrip detector is obtained by creating one electrode segmented in thin parallel strips. The disadvantage of this detector is that it provides only a one dimensional position information. On the contrary, if both electrodes are segmented into non parallel strips (angle of 90°between the two stripes) on the two opposite sides of the wafer, a two dimensional position information becomes available. This is usually called matrix detector. The main disadvantage of this technique is represented by the ambiguity problem of multiple hit events in particle fluxes applications, as for example in the ATLAS experiment at the Large Hadron Collider (LHC) [7] at the CERN laboratory (see Chapter 2).

When more than one particle pass through the sensor at the same time, Figure 1.9 shows a two particles case, a hit is detected in the corresponding strips. The signal created by the charge detected will be readout from two different channels, and therefore two cases hit positions are possible, giving four possible two-dimensional hit positions. In general, for n simultaneous hits, n^2 reconstructed hits are obtained, out of which $n!$ are not real ("ghost" hits). Therefore, if the number of real particles which hit the sensor is $n = 2, 3..$, the x number of ghost hits will be 4,6 and so on. At the price of having a reduced resolution in one of the directions, the ambiguity can be solved by using different crossing angles, smaller than

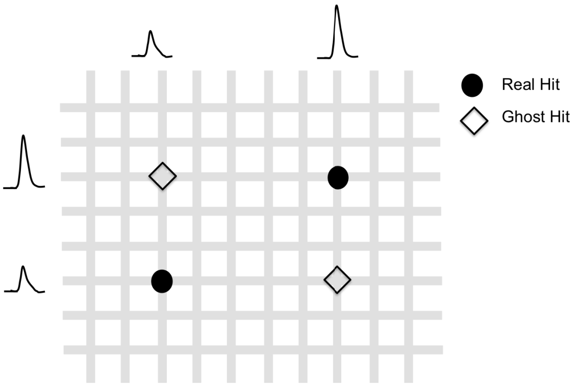

Figure 1.9: Schematic view of an ambiguity case for two particles that hit a strip sensor.

90°, but with the disadvantage of effectively reduce the area (in which ghost hits can be created). Alternatively, at the price of having higher computational cost, more layers can be added under varying crossing angles but with the additional disadvantage to increase the amount of material (increasing the probability of multiple scattering).

To avoid the ambiguity and still saving the 2D information, the solution is to segment one of the electrodes in both directions. This is the Pixel detector concept, as shown Figure (c) 1.8. This solution allows to have resolution similar to those of the detectors which use crossed stripes.

1.7 Hybrid Pixel Detector

The Pixel detector layout has a lot of benefits also for the readout. Not only it allows a smaller detector capacity, a smaller sensor leakage current, or a better signal over noise ratio (S/N), thanks to its capacity to maintain the signal and to reduce the noise due to a smaller area, but it is also able to reduce the hit rate. This is the most important aspect, in fact this parameter depends from the area of the strip or of the pixel. In the pixels case, the electronics is allowed to process the readout signal per channel more slowly compared to the strip, and this offers the advantage to operate at higher rate environment like the LHC. The disadvantage comes with the complexity of the readout and moreover with the connections of the electronic readout with the sensor itself. Two possible strategies are usually considered: use one single or few readout electronics per sensor or produce a hybrid Pixel detector. The first solution is mostly adopted for digital imaging, such as digital cameras[15]. It uses charge-coupled devices (CCD), but it has the disadvantage to require considerable time to process and elaborate the signal. In fact, the signal detected by each pixel cell is stepped column by column (or row by row) through the device into a final register which then is stepped cell by cell into a single channel read-out device (i.e.: a charge-sensitive amplifier or QSA) at its end. A second possibility is to have a matrix which connects all the

---

[15] Also in professional, medical, and scientific applications where high-quality image data is required.

pixels together, and the matrix switch activates one cell at a time. The signal is then passed to a single or a row of read-out devices. On the contrary, to be able to use the pixels at higher rates applications, the hybrid solution is preferable. Each pixel is individually connected to a read-out channel, composed by a charge-sensitive amplifier followed by a discriminator and/or ADC. Then the information is combined together into a bit stream (a dedicated section of Front-End will be explained in Section 3.3.1). As an example, Figure 1.10 shows a small volume sensor ($\approx 5 \times 10^{-3}$ mm^3) individually connected to the Front-End electronic to readout the charge. This is the so called hybrid Pixel detector. The term hybrid is used to underline that electronics and sensors are fabricated separately and then matched.

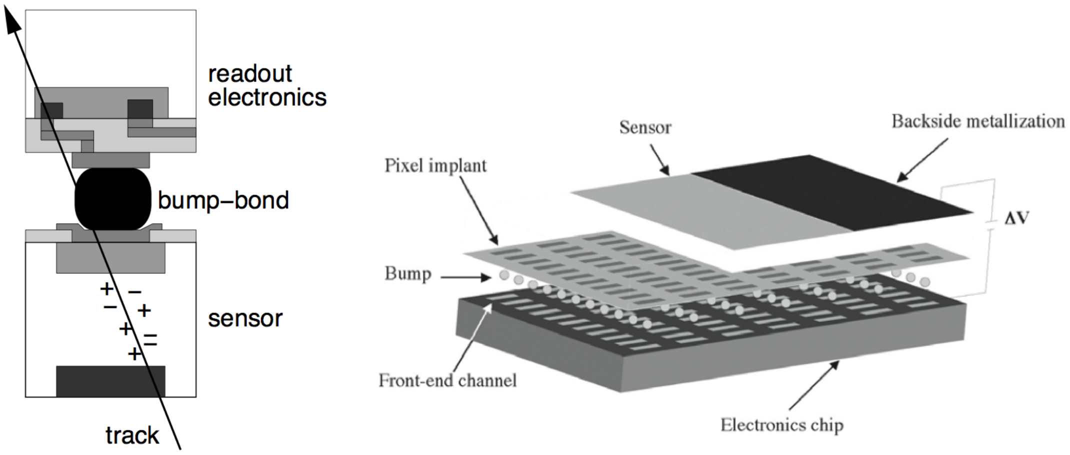

Figure 1.10: Left: scheme (not in scale) of one pixel cell: cross section of a hybrid pixel detector, showing the connection between the sensor and an electronics pixel cell. The black line indicates a crossing particle track which generate charge in the sensor volume that later will be collect by the electrodes [2], [8].
Right: scheme of an hybrid Pixel detector: Front-End plus sensors.

The key-characteristic of hybrid Pixel detector is the two-dimensional high density: it combines a vertical connection between the sensors and the Front-End electronics saving space. To reach this density the connection between the sensor and the Front-End chips is established through the bump bond, see Figure 1.10 (left), with a minimal pitch between the two of 50 μm. The direct consequence of this is that an exact matching between the size of the pixel and the electronic channels is required. Moreover, these must be very close to the sensor itself (10-20 μm). In fact, the dimensions are very small and critical: the area that each pixel covers is around 10^{-4}cm^2 over a thin 250-300 μm layers of silicon. The capacitance as well, is very low, around 0.2-0.4 pF, dominated by the neighboring pixels rather than by the backside plane. This allows to have a relatively low noise, around 200 e$^-$ for electronics operating at 40 MHz and therefore a S/N exceeding 100 for fully depleted 300 μm thickness sensors [2]. In fact, a detector threshold of 10 σ_{noise}[16] gives a full efficiency with a very low probability that noise fluctuation

---

[16] Where σ_{noise} is the standard deviation of the noise: how much variation exists from the average noise value.

exceeds the threshold. The excellent S/N ratio allows to use the pixel sensors also when the charge collection is reduced by the radiation damage (see Section 1.8). Another advantage to have such configuration is that the power supply can be applied to the backside plane of the structure, since all the pixels are grounded on the other side thanks to the virtual ground of the preamplifiers (once the Front-End is connected). This simplify the power supply structure as shown in Figure 1.10 (right). Thanks to all these advantages this detector is one of the best candidates to work in a very hostile environment in terms of radiation, like that of a high energy particle collider. In Table 1.3 the main advantages of the hybrid Pixel detectors are summarized.

Another possibility is the so called monolithic Pixel detector, where the Front-End electronics and the sensor are integrate together [9, 2]. In fact, since Silicon is widely used for Pixel detectors the natural strategy is to built in the same technological process.

Advantages	Short Description
Radiation Hard	Can survive after high radiation of particles as in the LHC.
3D measurement	No ghost hits: non ambiguous measurements with a good compromise resolution without using multi-layer strip detector or more complex designs.
Resolution	Good resolution to detect short-lived particles.
Patterns	It memorizes patterns that physics requires to analyze the origin of the hits (primary and secondary verteses).
Size	Very good (small) dimensions including Front-End electronics and sensor itself.
Power Supply	No complex structure required thanks to the backside metallization. Simplify structure which grows in vertical.
Low capacitance	Around 0.2-0.4 pF, thanks to the compactness and dimensions.
Excellent S/N ratio	Thanks to the low capacitance. It permits a considerable signal loss (poor charge collection, such as for diamond sensors and sensors damaged by high radiation).

Table 1.3: Main advantage of the hybrid Pixel detectors for high energy physics applications.

1.8 Radiation Damage

As it will explained in the next Chapters, sensors need to be qualified for a certain radiation or fluence. The radiation damage can be divided into two main effects: *bulk* and *surface damage*. The first is caused by the displacement of crystal atoms while the second includes all effects taking place in the dielectric layers[17] covering the sensors. The most important surface effect is the charge density increase in the oxide passivation layer, which saturates after some kGy to values of about $3{\times}10^{12}$ cm^{-2}. At high hadron fluences, bulk damage becomes the most important. Its main consequences for detectors are: *i)* the increase of the leakage current, proportional to the fluence. This leads to an increased power dissipation, which heats the sensor, and a higher temperature, which implies higher leakage current and therefore larger dissipated power. The result is a positive feedback system that may quickly diverge (thermal runaway), unless prevented by proper cooling; *ii)* the increase of the effective doping concentration and subsequent increase of the full-depletion voltage; *iii)* charge trapping. Usually traps[18] are mostly unoccupied due to the lack of free charge carriers, and can hold or trap part of the signal charge for a time longer than the charge collection time and consequently reduce the signal height. Preliminary results about the first step of the sensor irradiation program, corresponding to a fluence of 1×10^{15} n$_{eq}$/cm^2, were presented in [10].

---

[17] The dielectric layer is the oxide (SiO_2) which provides the isolation between two neighbor read-out electrodes, see Section 1.9, Figure 1.13.

[18] Impurities or dislocations which can trap an electron or hole and hold it until a pair is completed. Such carrier traps are sometimes purposely added to reduce the time needed to reach the steady state.

1.8.1 Inversion of the effective doping

In detectors with n-type Silicon wafer substrate, the initial effective doping changes with the irradiation fluence [11, 12]. Figure 1.11 shows dependence of the relationship between the depletion voltage, and the effective doping concentration of the bulk material with respect to the fluence, for a 300 μm of Silicon sensor. The depletion voltage is related with the doping concentration through to Equation 1.8.

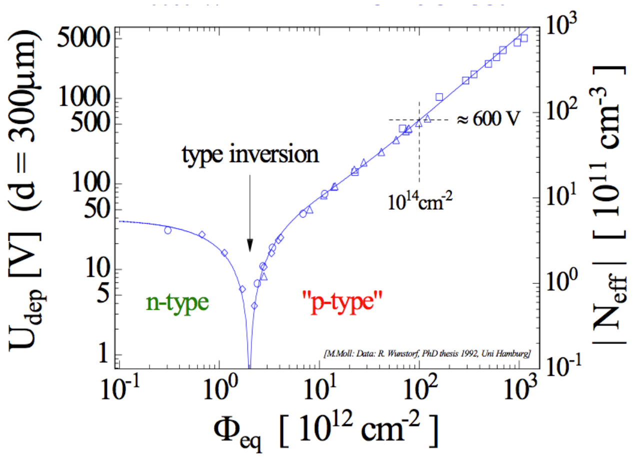

Figure 1.11: Dependence of the magnitude of the depletion voltage (left axis) and of the effective doping N_{eff} (right axis) [12, 13].

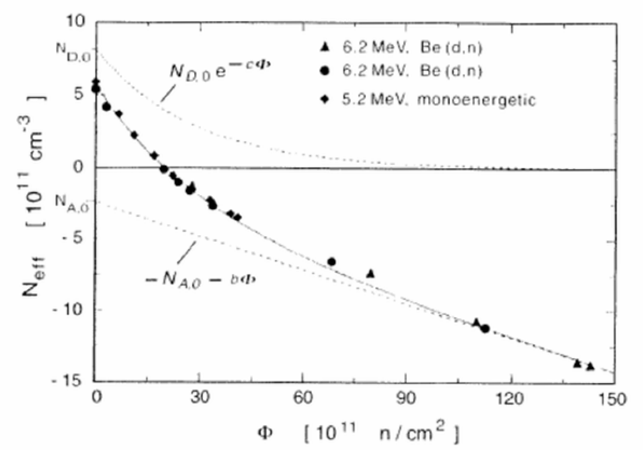

Figure 1.12: Parameterization of the effective doping dependence on the fluence, according to Equation 1.12 for an n-type Silicon wafer irradiated with neutrons [1].

Figure 1.11 shows the effective concentration measured immediately after irradiation. Due to the radiation the Silicon lattice suffers damages which consist in displacements of a Silicon atom from its original position. These damages act as acceptor centers. For a starting n-type material, the damage acts in a way to neutralize the effect of the donor atoms. It reduces N_{eff} to a point where N_{eff}

goes to zero at an irradiation fluence[19] of few times 10^{12} n/cm^2. At this point of minimum of concentration, the material is possible to be considered un-doped (the material becomes intrinsic). Above this minimum of concentration the doping becomes effectively of *p*-type (so-called type inversion) and eventually rises linearly with fluence [1]. The effective doping concentration could be expressed as:

$$N_{eff}(\phi) = N_{D,0}e^{-C_D\phi} - N_{A,0}e^{C_A\phi} + b_D\phi - b_A\phi \tag{1.11}$$

with $N_{D,0}$, $N_{A,0}$ being the donor and acceptor concentration before irradiation and C_D, C_A, b_D, b_A constants to be determined experimentally. Assuming an absence of acceptor removal and donor creation, the parameterization for effective doping simplifies to:

$$N_{eff}(\phi) = N_{D,0}e^{-C\phi} - N_{A,0}e^{b\phi} \tag{1.12}$$

with $c = 3.54 \times 10^{-13}$ cm^2 ± 4.5% and $b = 7.94 \times 10^{-2}$ cm^{-1} ± 8.0%. The original doping and doping concentration can be determinate by looking at the intercept of the fitting terms with vertical axis of Figure 1.12.

1.9 Isolation Technique Among Pixels

Recent studies have shown that Silicon detectors made on p-type substrate have a higher radiation hardness compared to more conventional single n-type devices [14, 15]. On the contrary, the isolation technique to be employed for the interruption of the inversion electron layer between the readout electrodes (n$^+$ electrodes) depends on the type of application and characteristic that the device wants to achieve. In the particle detectors produced with a technology n$^+$ -in- p, due to the irradiation, which causes a strong increase of the positive charge trapped in oxide, the electrons layer induced in proximity to the surface of the wafer, may create the unwanted effect of a short circuit between plants of different pixels. Therefore, in the design stage, it is necessary to take adequate precautions to prevent this from happening. As Figure 1.13 illustrates, the most common techniques are: p-spray, p-stop and a combination of the previous two, called moderate p-spray.

p-stop: the p-stop technique is the most commonly used to achieve the isolation among pixels. It consists in introducing a p-type region strongly doped, see Figure 1.13 (a). The advantages of such an approach are that with a dose of 10^{14} cm^{-3} of Boron[20], it is possible to reach a good isolation in presence of saturation oxide charge in the oxide (2×10^{12} cm^{-3}). The main disadvantage is related to the creation of a p-n junction with the lateral inverse substrate which could modify the breakdown voltage. Therefore with this technique it is important to keep under control the intensity of the electric

---

[19] The fluence value at which type inversion occurs depends on the original doping, as the parameterization in Figure 1.12 shown.

[20] B, atomic number equal to 5, introduces a free hole charge when it is used to dope silicon materials.

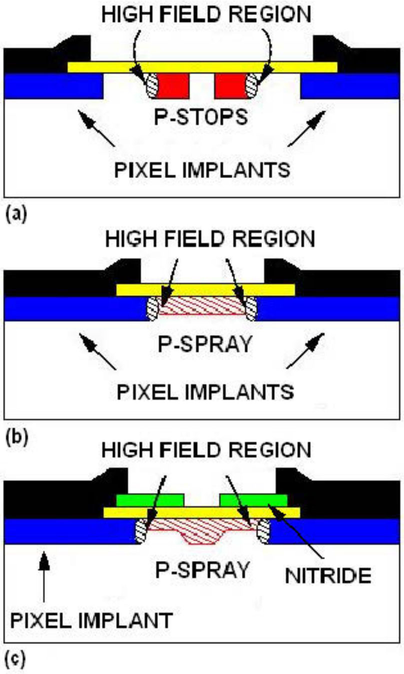

Figure 1.13: Sketches of the three possibles type of isolations between the electrodes: (a) p-stop, (b) p-spray and (c) moderated p-spray. The regions with a high value of the electric field are indicated [15]

field close to this critical junctions both before and after irradiation. Before irradiation the p-stop technique has an higher breakdown voltage: the crucial part is the surface point between the p-stop implant and the read out electrode (the n^+ electrode). On the contrary, after irradiation, the breakdown voltage due to the increasing concentration of electrons at the Silicon oxide interface is reduced. The second disadvantage is that the isolation through p-stop requires the introduction of an additional lithographic step to align the p-type plants with the pixels.

p-spray: with the p-spray, contrary to the p-stop technique, no additional lithographic step is required. The isolation is made by an uniform p implant doping between the electrodes along all the wafer structure, see Figure 1.13 (b). The doping is created at the first steps of the fabrication process before any lithography, and is later completed at the hard n^+ doping process which reduces the initial high doping values. Therefore, the high field region is created between the n^+ electrodes and this uniform implant, and in such regions the breakdown process starts at higher voltages. Typically, detectors with p-spray isolation show a low breakdown voltage before irradiation due to surface breakdown where p-spray and n^+ electrode are in contact or, in other way, where the electric field is higher. P-spray devices increase their radiation resistance, due to the development of oxide charge compensation, leading to a progressively lower electric fields at p-n boundaries as irradiation proceeds. After irradiation the increased oxide charge lowers the effective doping concentration of the p-spray at the surface, due to compensation and the breakdown voltage is shifted to higher values [16]. Therefore the p-spray isolation, gets better and better as the irradiation dose increases. The concentration of the p-stop layer has to be high enough not to leave the electrons layers.

moderated p-spray: the mixed solution consist of a mixture of the p-stop and moderated p-spray techniques, see Figure 1.13. The advantage of this isolation consists in reach a high breakdown voltages both before and after irradiation, with a sufficient level of isolation between the readout electrons. The idea is to improve the p-spray isolation behavior keeping the good performance after irradiation. In this strategy, the p-spray implant is made after the n^+ electrode, creating in the central region a higher than p-doped concentration at the two extremities close to the electrode pixels. The doping concentration, in the central part of the sample, has to be chosen in such a way to resist in a large radiation range conditions, while at the extremities has to be optimized to work in a high voltage conditions.

Chapter 2

LHC and the ATLAS experiment

This Chapter is dedicated to the description of the proton-proton Large Hadron Collider (LHC) at the CERN laboratory, Geneva (Switzerland) and one of the four experiment at LHC, the ATLAS detector. A particular attention will be given to the tracking device of the ATLAS detector, to then focus on the innermost part: the Pixel Detector. The Pixel Detector plays a key role in the reconstruction of the primary vertices from the proton collisions and secondary vertices produced by short-lived particles coming from these collisions. To cope with the high level of radiation present during the collider operation, it has been planned to add an additional inner 'layer' to the Pixel Detector, the so called Insertable B-Layer or IBL. In this section it will be explained why an IBL will be needed, and its planned structure which will make also use of a new type of Silicon sensors.

2.1 CERN

CERN (*Conseil Européen pour la Recherche Nucléaire*[1]), is the world's largest particle physics laboratory, located in the northwest suburbs of Geneva on the border between France and Switzerland.
It is an international organization created on the 29th September 1954 in order to rebuild the high energy physics in Europe after the dark period of World War II. Originally, 12 states signed the CERN convention and the membership has grown up to the present 20 member states. Nowadays it counts about 2400 full-time employees, as well as some 7931 scientists and engineers representing 608 universities and research facilities and 113 nationalities using its facilities. The research at CERN is of fundamental nature: it does not focus on the development for new products or to industries alternative sources of energy or medicine, but to better understand the origin of our universe and its fundamental components. Certainly there can be or will be major industrial and economic spin-off from these studies, but is not the first goal. One very famous spin-off of the researches conduced at CERN, is the development of the World Wide Web (www).

The main CERN function is to provide the accelerators which accelerate particles at the speed of light and make then collide against each others and the other

---

[1] or European Organization for Nuclear Research

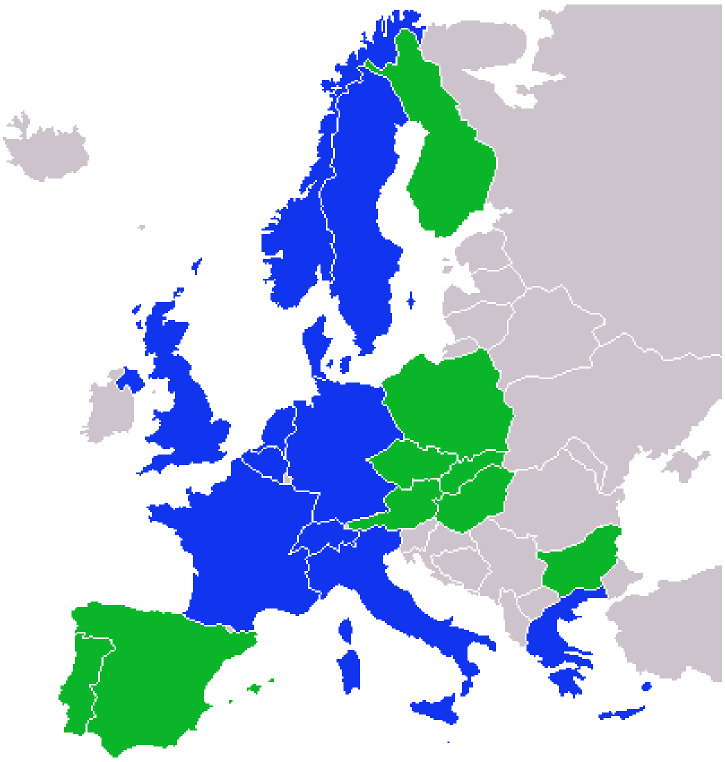

Figure 2.1: CERN member states: in blue the funding members, in green members who joined CERN later on.

infrastructures needed for high-energy physics research. The field of physics called "high energy" explores the secrets of matter and of the forces which link together the universe. CERN is helping in the realization of experiments that represent the status of the art from both the technological and scientific point of view of this kind of research. The CERN laboratory includes a large computer centre with very powerful data processing facilities primarily for experimental data analysis. Because of the need to make these data available also to researchers residing in other institutes (outside CERN), it has been (and continues to be) a major wide area networking hub. Indeed, numerous experiments have been carried on at CERN by many international collaborations since its birth. Scientists from several universities or research centers can come to CERN or use the tools remotely for this research, like laboratories and facilities. The original CERN members were: Belgium, Denmark, Germany, France, Greece, Italy, Norway, Sweden, Switzerland, Netherlands, United Kingdom, Yugoslavia. Later on other countries joined Austria (joined 1959), Yugoslavia (left in 1961), Spain (joined in 1961, left in 1969 and rejoined in 1983), Portugal (1985), Finland and Poland (1991), Hungary (1992), Czech Republic and Slovakia (1993), Bulgaria (1999).

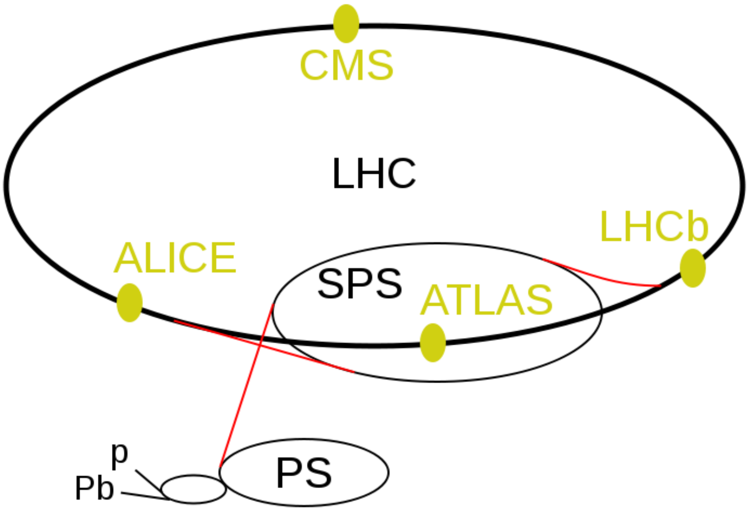

Figure 2.2: The accelerator complex at CERN, including LHC.

2.2 The LHC hadron collider

The LHC is a circular proton-proton collider machine built at CERN. It has been developed in the circulator tunnel previously used by the LEP[2] experiment, which was shut down in 2000. The LHC characterized by having a large number of superconducting magnets to bend and focus the protons, is located in a tunnel digged at a depth ranging from 50 to 175 metres (100 meters in average) below the sea level, crossing the Swiss-France boarder, between the Geneva airport in Switzerland, and the Jura mountain in France. The proposal is dated 1990, but the digging started in 1996 and only after almost ten years the first run of the LHC started, during the end of Summer 2008 (September 10th). Unfortunately, few days after the start there was an accident: a cryogenic magnet support broke during a pressure test involving one of the LHC magnet assemblies. This accident caused an explosion who damaged several dipole magnets and a leak of six tons of liquid helium. It has then been necessary to stop the running and repair the damage. Only after one year of hard working and checking all the magnets[3], the LHC started to be functional again. Now it is the world's largest and highest-energy particle accelerator: it is designed to accelerate protons in two opposite circulating beams up to an energy of 7 TeV[4]. This results in center of mass energy at the collision point of 14 TeV: an energy region never yet reached by previous machines. Presently it is running at a lower energy: 7 TeV and has collected already 5 fb^{-1} of data. In 2013 the LHC will stop for one year and half about, and will then restart at the project energy.

The highest center of mass energy so far was of 1.96 TeV, reached by Tevatron

---

[2] Large Electron-Positron Collider

[3] it has been necessary to bring back on the surface all the magnets, test them, repair them, if needed, and put then back into the tunnel.

[4] $1\ TeV = 1\ Tera - electronvolt = 10^{12}\ eV$

accelerator at the Fermi National Accelerator Laboratory (Chicago, USA)[5]. To acquire a decent rate of rare events, a high luminosity of 10^{34} cm$^{-2}s^{-1}$ is required. The luminosity is defined as (in a ring collider):

$$L = f \frac{n_1 n_2}{4\pi\sigma_x\sigma_y} \tag{2.1}$$

where:

- f is the frequency[6]
- n_i is the number of particles in each bunch
- $4 \cdot \pi \cdot \sigma_x \cdot \sigma_y$ is the cross section of the beam, where σ_x and σ_y measure the beam transverse dimensions

The integrated luminosity $l = \int L\,dt$ is the integral of the instantaneous luminosity with respect to time, so that the number of events is given by $n = \sigma \int l\,dt = \sigma L$ The luminosity is an important value to characterize the performance of an accelerator. The event rate dN/dt is given by the product of the luminosity times the cross-section: $dN/dt = L \cdot \sigma$.
The LHC lies in a 27 km circular tunnel and its mains components are dipole magnets that keep the beams on a circular path. It consists of eight straight sections of approximately 528 m length (this gives the approximately number of 27 km) with bent intersecting parts equipped with superconducting dipole magnets to keep the protons on track. There are 1232 dipoles while other 392 quadrupole magnets are used to keep the beam focused in order to maximize the interaction probability between the two beams. In total 1600 superconducting magnets are installed, for a total weight of 27 tons. The magnets, made of copper-clad niobium-titanium, are cooled down at 1.9 K (-271.25° C) to keep them at their operational temperature[7], see Figure 2.3.

Before entering the LHC, protons are accelerated by an already existing chain of smaller accelerators, a Linac[8], a Booster, the PS[9] and the SPS[10]. After this preliminary acceleration the two beams of protons are injected into the LHC at an energy of 450 GeV. As the proton bunches are accelerated in two beams which are rotating clockwise and counter-clockwise, there are two separated beam pipes installed. It is then possible to apply a magnetic fields designed in such a way to bend the opposite traversing particle trajectories in order to keep them on a circular trajectory. Once the protons have reached the needed energy, the two

---

[5] The Tevatron accelerator was stopped on the 30th September 2011

[6] $f = f' \cdot n$, where n is the number of bunches in one beam and f' is the cycle frequency. At LHC, f = 40 MHz is the frequency between one bunch and the next one (inside LHC the two groups of bunches have the same f).

[7] This make the LHC also the largest cryogenic facility in the world at liquid helium temperature

[8] Linear Accelerator

[9] Proton Synchrotron

[10] Super Proton Synchrotron

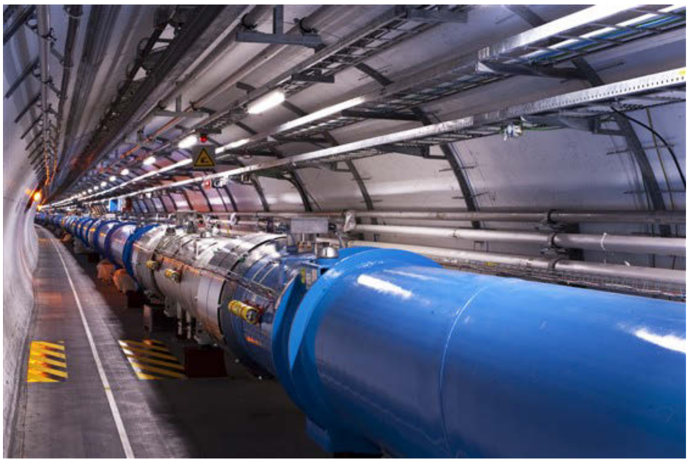

Figure 2.3: Photo of the dipole magnets inside the LHC tunnel.

beams are sent, again thanks to a magnetic field, one against the other, and from their energies new matter can be created as predicted by Einstein's formula: $E = m \cdot c^2$. From these particle collisions new particles previously unknown might be generated. As displayed in Figure 2.2, there are four different detectors mounted around the four collision points.

ATLAS and CMS are two general purpose detectors optimized to study the productions of new physics at proton-proton collisions and possibly discovers the Higgs boson, a missing piece not yet discovered, of our present best theory to describe the matter constitutes and their interactions, the so-called Standard Model (SM). LHCb is dedicated to the study of the b-quark physics. Finally, ALICE will study heavy ion collisions (for a fraction of time, LHC will make collide also heavy ions) to look for a new state of matter, the so-called "quark-gluon plasma"which was present at the start of our universe, after the "big-Bang". The planning of the tunnel has required an incredible precision: the interaction points had to be defined with a precision along the beam path of the order of less than a mm. To maintain steady the beam orbits, superconductors have been used, and even the tidal force of the Moon and Earth have been taken into account.

2.3 ATLAS

The ATLAS, acronym of A Thoroidal Large ApparatuS, detector is one of the four detectors at the LHC proton collision points. It is composed by different sub-detectors of cylindrical shape one inside the other, with their axes along the beam pipe direction. The very harsh environment of LHC in terms of extremely high energy and rate of collisions, requires ATLAS to be larger and more complex than any detector ever built. Each cylindrical layer is devoted to the identification and measurement of a certain type of particles. ATLAS is designed as a general-purpose detector. When the proton beams collide at the center of the detector a variety of different particles with a wide range of energies may be produced. ATLAS allows to have a full coverage to detect all these new possible particles.

Its purpose is to identify the outgoing particles from these collisions and measure their kinematic properties without focusing on a particular physic process, but rather measuring the broadest possible range of signals. The main goal is to ensure that whatever particle is going to be produced, ATLAS will be able to detect and measure it. A good reconstruction of the event generated after a collision is possible only if the properties (type, energy, momentum, charge) of all the particles in the event are precisely measured. A schematic view of the ATLAS detector is given in Figure 2.4.

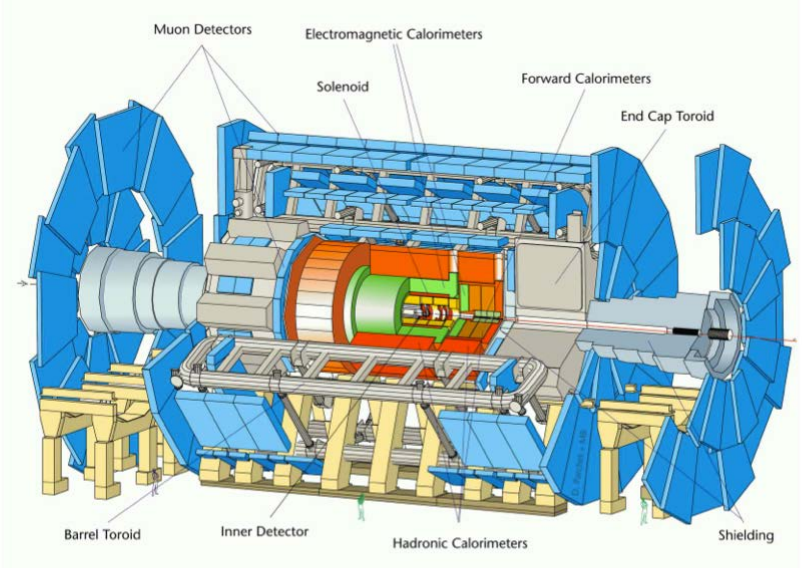

Figure 2.4: Schematic view of the ATLAS detector. The innermost part is the tracker, and an eletromagnetic and a hadron calorimeters follow. The outermost part is made by muon chambers embedded in a large Toroidal magnet.

The ATLAS detector, shown in Figure 2.4, measures 46 m in length and 22 m in width as well as in height, and its total weight is of 7000 tons.

A cartesian coordinate system to locate tracks, vertex and particles in the detector is used, which is shortly explained here.

- the origin (0, 0, 0) is located at the nominal interaction point,
- the x-axis points to the middle of the accelerator ring,
- the y-axis points upwards,
- the z-axis completes the right handed coordinate system (and points into the beam direction).

While analyzing the direction of flight of the objects produced after the collisions in the center of the detector, a two-dimensional system is used. Given the momentum vector p, the azimuthal angle ϕ and the polar angle θ[11] are defined

---

[11] Positive angle with respect to the z coordinate.

as:

$$\phi = \arctan \frac{p_y}{p_x} \tag{2.2}$$

$$\theta = \arctan \frac{p_T}{p_z} \tag{2.3}$$

where the subscripts x, y and z denote the projections of the momentum vector on the respective axis andp_T stands for transverse momentum which is calculated using the formula:

$$p_T = \sqrt{p_x^2 + p_y^2} \tag{2.4}$$

In practice, θ is replaced by the pseudo-rapidity η. This quantity is defined as:

$$\eta = -\log \tan \frac{\theta}{2} \tag{2.5}$$

If one wants to calculate a distance between two objects in the $\eta - \phi$-plane, the formula

$$\triangle R = \sqrt{(\triangle\eta)^2 + (\triangle\phi)^2} \tag{2.6}$$

can be applied.
One can then move along the positive y-axis direction to list all sub detectors which are encountered from the collision point: the Inner Detector surrounded by a super-conducting solenoid, the Calorimeters and the Muon Spectrometer with its gigantic superconducting air-core toroids. These main three parts are divided into 12 different specialized sub-detectors that perform different tasks such as track reconstruction, particle identification and energy measurements.

2.4 Working principles of the ATLAS sub-detectors

The main purpose of the ATLAS detector is the search for the Higgs boson and of course of any new physics as predicted by various theoretical model which go beyond the Standard Model. Data from previous experiments and theoretical limits restrict the Higgs boson mass in the range between $114,4\, GeV < m_{Higgs} < 1\, TeV$. The requirements to cover the large mass range where the Higgs boson can be found have been met by ATLAS, thanks to different sub-detectors which have been assembled to form a multipurpose status. For the reconstruction of a Higgs boson, which decays almost instantaneously close to the collision point, particle identification is a vital part since the Higgs can decay in any of the particles included in the Standard Model, depending on its mass. The basic principles of the interplay of different parts of the detector which allow to get the information about the particle type is shown in Figure 2.5.

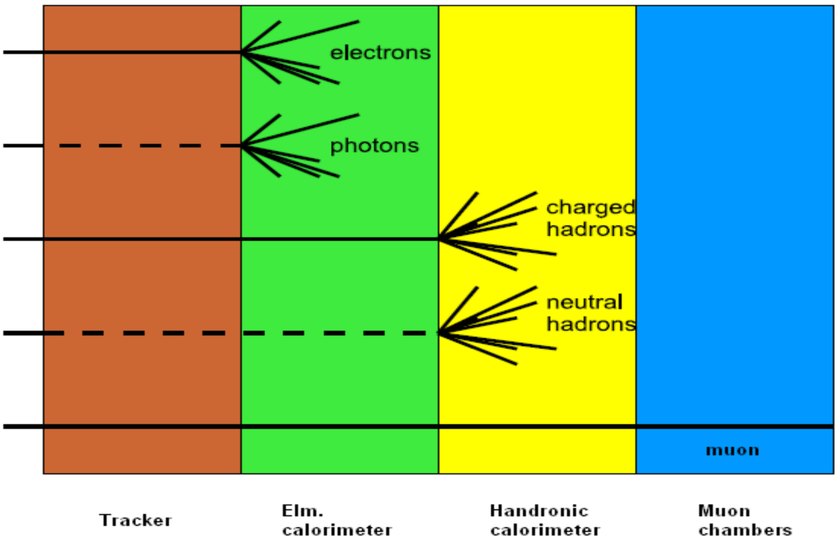

Figure 2.5: Particle identification [17]. Schematic view of the interaction of different particles with the various sub-detectors components of the ATLAS detector.

Depending on their energy loss in matter, different particles are stopped at different places in the detector. Electrons go through the tracker which is dedicated to the identification and measurement of charged particles, and produce a shower of secondary particles in the electromagnetic calorimeter. Photons are not seen in the tracker but produce a shower in the electromagnetic calorimeter. Hadrons need more massive material to be stopped, therefore they reach the hadronic calorimeter and produce a shower there. Neutral hadrons, especially neutrons, are not seen in the tracker, nor in the electromagnetic calorimeter. Muons can pass through all the layers of absorbing material and reach the Muon chambers. Only muons can travel such a long distance up to the muon chambers and therefore they are easily identified. By applying magnetic fields and a tracking device it is possible to measure the particle curvature radius, whereas the calorimeter system can measure their energy. Knowing their mass and the curvature radius, it is possible to calculate the particle momentum. With this kinematic information it becomes possible to reconstruct the primary particles from which the measured ones originate and therefore get information about their properties. The individual sub-detectors are discussed in more detail in the following sections. A common feature of the sub-detectors is the division into barrel and end-cap parts, where the barrel part is covering particles with low pseudorapidity, η, as previously defined in Equation 2.3, and the end-cap part is covering high pseudorapidity.

2.5 The Inner Detector

The Inner Detector is the innermost part of the ATLAS experiment. It is designed to reconstruct the charged particles trajectory with high resolution. A low material budget is used to avoid distorting the energy measurements in the calorimeters. The design concept includes three individual sub-detectors. From outermost to innermost those are: the TRT[12], the SCT[13] and the Pixel detector. The Inner Detector is embedded in a magnet that bends the particle tracks and allows momentum measurement. A schematic view of the Inner Detector is given in Figure 2.6. The output of this detector are the hits concatenated with geometrical information. This results in a sample of space points which are related to a bent curve to get the particle track. Another goal of the Inner Detector is the identification of jets of particles[14] originated from the fragmentation of a b-quark the so-called b-tagging. B-quarks, which are produced close to the interaction point, are long lived compared to particles like the Higgs boson and travel a measurable distance (depending on their initial momentum) before they fragment. A jet from a b-quark therefore will look like being originated from a secondary vertex, displayed with respect to the primary one. Reconstructing a secondary vertex with the tracking detector allows b-tagging of a hadronic jet. For the physics goal of finding the Higgs boson this is critical considering the importance of the $H \to b\bar{b}$ channel for the discovery of a low mass Higgs.

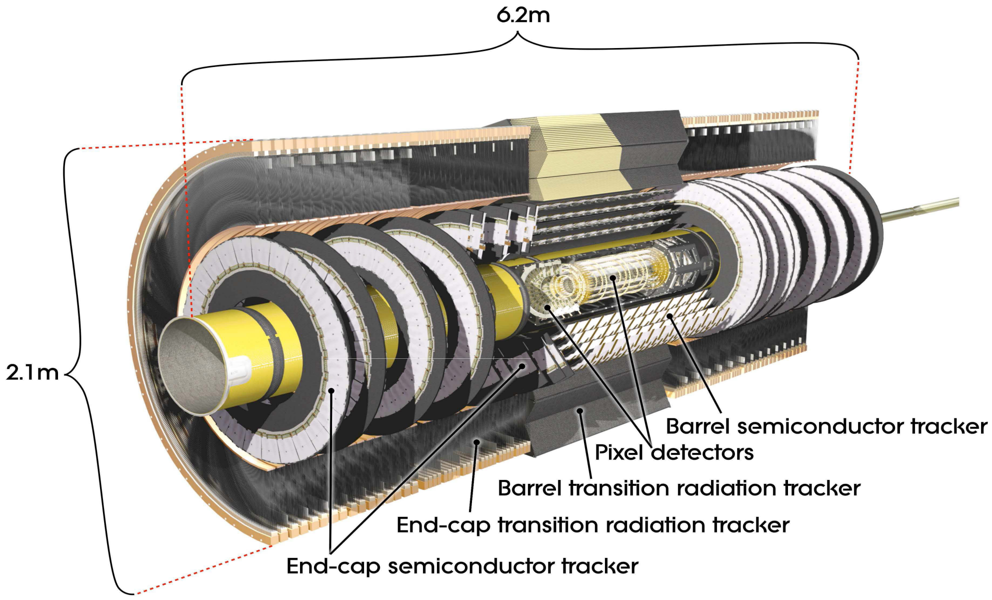

Figure 2.6: Schematic view of the ATLAS Inner Detector [17].

---

[12] Transition Radiation Tracker

[13] Semiconductor Tracker

[14] Quarks produced in proton-proton collisions, are not identified as single quarks for the so-called confinement effect: they immediately fragment producing a jet of particles, with its axis directed approximately along the originating quark direction.

2.5.1 Pixel Detector

The ATLAS Pixel detector is the innermost layer of the ATLAS tracking system and it provides a set of granular and precise measurements very close to the interaction point. The position of the Pixel Detector requires excellent radiation hardness, mechanical and thermal robustness, good long-term stability and all this must be combined with a low material budget. This detector, based on semiconductor technology, is built to provide three precision measurements of space points for the 40 MHz bunch crossings. Thanks to such a performance, the physicists will be able to reconstruct the vertex of the collision and together with the other detectors do a measurement of the momentum of each charged particle. The sensitive part of the detector is about 1.3 m long, has a diameter of 35 cm and a weight of 4.4 kg. The Pixel system consists of three barrel layers and six disks (three disks each end-cap) with the same geometry.

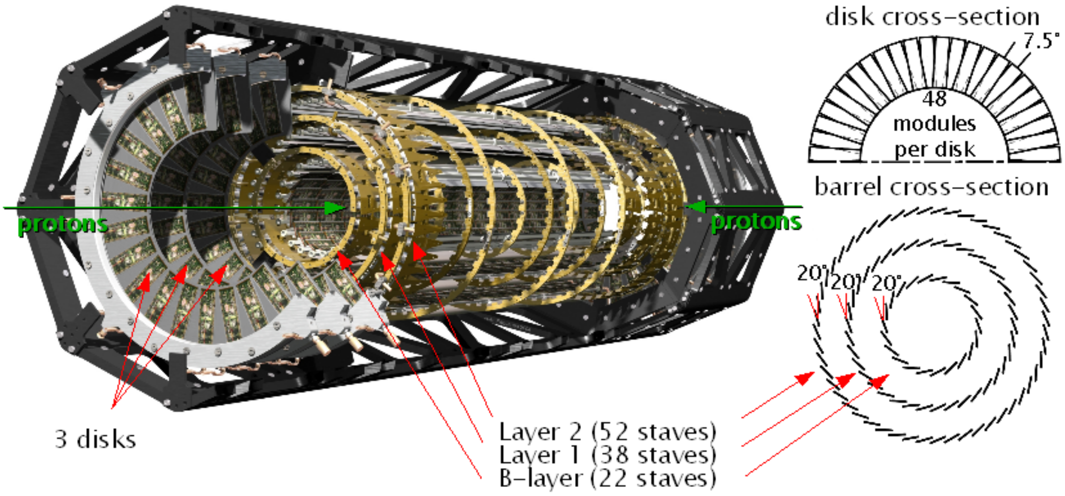

Figure 2.7: Layout of the ATLAS Pixel Detector with 3 barrel layers and six disks, three for each region.

The barrel layers are three coaxial cylinders called, B-layer, Layer-1 and Layer-2, with nominal radii of 50.5, 88.5 and 122.5 *mm* respectively [18]. All support structures are made of carbon composite materials. The global carbon-carbon support structure locates the layers, holding respectively 22, 38 and 52 structural elements called staves. The staves of a layer have a tilt angle of 20°. To close the area there are three disks each for two disk sections as shown in Figure 2.7. The complexity of the detector has lead to numerous test procedures and the setting-up of different sites where Pixel sub-detector parts were assembled and tested before being sent to CERN. The mechanical and electrical tests of one third of all the pixel wafers have been performed in Udine. The assembly and testing of the whole Pixel detector has been done at CERN. Each barrel layer consists of a turbine-like sequence of tilted staves. The staves design is identical throughout the three layers. One stave supports and cools 13 electronic modules. There is one cooling tube per stave and one cooling loop circuit, which cools two staves in series. The most relevant parameters of the barrel layout are given as summery in Table 2.1.

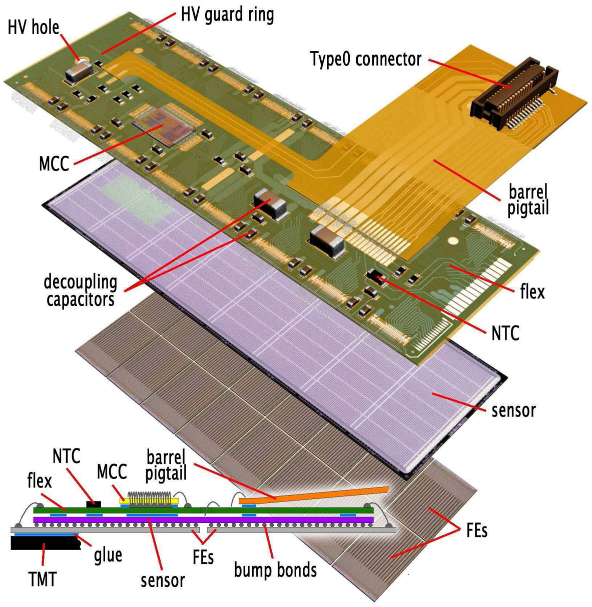

Figure 2.8: Schematic view of a Barrel Pixel module illustrating the major pixel hybrid and sensor elements, including the MCC (module-control chip), the Front-End (FE) chips, the NTC thermistors, the high-voltage (HV) elements and the Type0 signal connector. Also shown (middle) is a plan view showing the bump-bonding of the Silicon pixel sensors to the polyimide electronics substrate [19].

	No. of staves	No. of modules	No. of Pixels
B-layer	22	286	13.2×10^6
Layer 1	38	494	22.8×10^6
Layer 2	52	676	31.2×10^6

Table 2.1: Main parameters of the barrel Pixel detector: numbers of staves, modules and cooling circuits.

The basic functional unit of the Pixel Detector is the Pixel Module. There are 1744 modules in the Pixel Detector (see [19]). The module is essentially a hybrid assembly consisting of 16 readout chips arranged in two rows, connected to a silicon sensor. The sensor is rectangle-shaped and has an active area of 60.8×16.4 mm^2[15] and thickness of 250 μm. Each Front-End chip has 2880 readout channels

---

[15] Divided into 47232 pixies with an area of 400×50 μm except for a fraction with a size of 600×50 μm.

reading out 2952 sensitive channels [8, 20, 21, 22]. Pixels between neighboring chips in z direction are elongated to 600 μm instead of the usual 400 μm (referred as long pixels, located in the inter-chip regions), while pixels between neighboring chips in the ϕ direction are connected by trances on the passivation on the sensor to pixels that can be read out (called ganged pixels). The 16 chips read out in total 46080 channels, but all 47232 pixels are readout, as pixels in the inter-chip regions are ganged together to be read out. The steering of the readout chain is done by the Module Control Chip (MCC) [23]. It collects the data from the 16 readout chips convert the signal into optical signals and send then via optical fibres to the off-detector electronics. It provide as well the clock and control signals to the individual front-end chips. Each sensor pixel is connected to one read-out pixel via bump bonds (with the exception of the aforementioned ganged pixels). The Front-End is connected to a flexible printed circuit board via wire bonds and, at the end, the module is connected with the outside world through a custom-made aluminium cable. This is connected to the flex directly for the disks modules or plugged into a connector on another little flex kapton PCB (the pigtail) in the case of the barrel modules. These cables are plugged into connectors on the PP0, which is why they are called Type0 cable. Every detector module is connected to an optoboard channel which converts the electrical data signals transmitted from the modules to an optical signal for transmission to the off-detector electronics via optical fibres. In parallel it receives optical signals from the off-detector electronics and converts these to electrical signals for distribution to the modules.

2.5.2 SCT

The SCT is a silicon microstrip detector located in the middle layer of the Inner Detector. It consists of four concentric barrel layers increasing radii and two end-caps of nine disks each. The barrel layer carries 2112 detector modules, while 1976 end-caps modules are mounted on the disks for a total of 4088 modules. The whole SCT occupies a cylinder of 5.6 m in length and 56 cm in radius with the innermost layer at a radius of 27 cm. Contrary to the Pixel Detector (see following Chapter) the SCT uses silicon strips with instead of silicon pixels, so that particle track information could only be extracted in one dimension. By installing layers of silicon strips with a relative angle to each other, the information on the second dimension can be extracted with some combinatorics. The total silicon detector area is 61 m^2 with a total of 6.2 million readout channels. This results in an angular resolution of 16 μm.

2.5.3 TRT

The Transition Radiation Tracker (TRT) is the outermost part of the Inner Detector. Its main function is to register the tracks of charged particles. It is also used to help distinguish pions from electrons. Basically the TRT is a straw detector with transition radiation generating material. A straw detector consists of gas-filled tubes with a wire in the middle. Each straw works like a drift tube. A high-voltage is applied between the wire in the centre and the straw (the outer boundary of the gas volume). When a charged particle passes through, it ionizes the gas molecules. The electrons that are liberated are then accelerated in the electric field, creating a cloud large enough to be detected by the electronics attached to the wire. The signals from all the straws crossed by the particle are used to reconstruct its path. As already mentioned, the TRT is also used to distinguish electrons from pions. Electrons are more likely than pions to emit transition radiation photons when they pass through the layers of radiator foils before reaching the straws. Transition radiation is produced by high-energy particles passing a boundary between two materials with different dielectric constants. The transition radiation alters the charge collection in the straw and is used to identify electrons together with the electromagnetic calorimeter (see Chapter 2.6.1).

The TRT consists of tubes filled with Xenon gas with a diameter of 4 mm and a length of 39 cm - 150 cm throughout the detector. Xenon as a gas fill makes the detector intrinsically radiation hard. The wires are made of gold-plated tungsten with a diameter of 30 μm. The TRT barrel has three layers (three cylinders with increasing diameter). Each layer consist of 32 identical modules with, from the inner to the outer layer, 329, 520 and 793 axial straws each. In between the straws polypropylene/polyethylene fibres are mounted to generate the transition radiation. The end-caps consists of three wheels on each side of the detector, also consisting of straw tube layers with radiator foil in between. With this design of the detector a particle with transversal momentum > 0.5 GeV and $\eta < 2.5$ is expected to cross 40 straws. This design gives the TRT a spatial resolution of about 50 μm.

2.6 Calorimeter system

A calorimeter system is needed to measure the energy of particles like electrons, photons or quark-jets including a measurement of their position and propagating direction. As needed for particle identification (see Figure 2.5), the system is divided into an electromagnetic and a hadronic calorimeter. The electromagnetic part has to have a high resolution, in energy as well as in angular position, to identify a Higgs decay peak against the background. Radiation hardness is also an issue at the LHC luminosity, which accounts for the choice of different materials for the high coverage in the hadronic calorimeter.
The ATLAS detector also employs a forward calorimeter for the very high ($4.9 > |\eta| > 3.2$) pseudorapidity range.
A schematic view of the calorimeter system can be seen in Figure 2.9.

2.6.1 Electromagnetic calorimeter

The Inner Detector is surrounded by the Electromagnetic Calorimeter covering a range of pseudorapidity $|\eta| < 3.2$. It is an accordion-shaped Lead-liquid Argon detector which is divided into a barrel and an end-cap part, with an outer radius of 2.25 m. It meets the requirement for radiation hardness, since liquid Argon

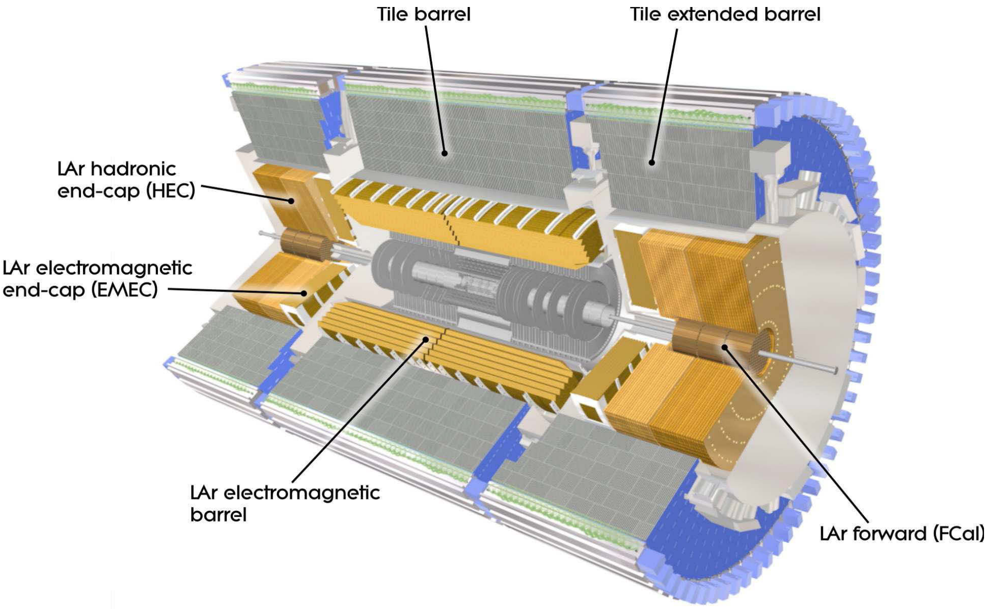

Figure 2.9: ATLAS calorimeter system [19].

is intrinsically radiation hard. To make the construction easier, the barrel was divided into two half-barrels each including 1024 absorber modules alternating with 1024 readout units. The end-cap parts were made of eight wedge-shaped modules with 96 absorbers each. The best granularity achieved is $0.025 \cdot 0.025$ in $\Delta\eta \cdot \Delta\Phi$ meeting the required angular resolution described before.

2.6.2 Hadronic calorimeter

The hadronic calorimeter consists of a barrel part, the Tile calorimeter, and two end-caps. The materials for those parts differ due to radiation hardness considerations. The Tile calorimeter barrel is divided into barrel and extended barrel parts with an outer radius of 4.32 m. The assembly unit for this sub-detector is a wedge-formed structure consisting of sandwiched steel plates of various dimensions alternated with read-out units [17]. Each barrel part is formed of 64 of those wedges. The gaps created by this design are needed to let the cabling for the Inner Detector pass. The granularity achieved by the Tile calorimeter is $0.1 \cdot 0.1$ in $\Delta\eta \cdot \Delta\varphi$. The mechanical structure of the Tile calorimeter is also designed to guarantee the stability of the Inner Detector since it is decoupled from the outer muon chambers support structures. The hadronic end-cap is a Copper-liquid Argon detector. This choice of material is necessary since the end-cap is installed at a high pseudorapidity area, requiring better radiation hardness than the barrel. Both end-caps consist of two doughnut-shaped wheels built out of 32 identical modules each. In addition, the hadronic and electromagnetic calorimeters share a forward calorimeter, the FCAL[16]. The FCAL is made of Copper for the electromagnetic and of Tungsten for the hadronic part covering a high pseudorapidity

---

[16] Forward calorimeter end-cap region.

range.

2.7 Muon chambers

Muon detection plays a vital role for particle detectors, as muons are (together with the neutrinos) the only particles which can cross the full calorimeters without being stopped. This makes them good candidates for triggering on interesting events by measuring their energy after the calorimeter, since in this case the background due to other particles is low. For this reason the calorimeter system is followed by a muon spectrometer consisting of muon detectors and bending magnets [19]. The bending system has a barrel part and an end-cap part on each side. The barrel toroid is made of eight superconducting coils 25 m long. They are arranged around the beam axis to form a cylinder with an outer diameter of $\approx$ 20 m. The two end-cap toroids are also built from eight single coils each mounted in a cryostat and inserted into the barrel at each side. The bending power of this system ranges from 3 Tm in the barrel region to 6 Tm in end-cap one. The Muon detection system employs four different detector types. MDT[17]s cover most of the pseudorapidity region. They are aluminium tubes of 30 mm diameter with a wall thickness of $400\mu m$ and a $50\mu m$ thick W-Re wire. The tubes are filled with $Ar - CH_4 - N_2$ gas at a pressure of 3 bar and form a drift chamber with a drift time of $\approx$ 500 ns. Closer to the interaction point and at high pseudorapiditiy CSC[18] are used since they provide a better granularity and a faster response. These are multiwire proportional chambers, the drift time is lower ($\approx$ 30 ns) than the MDT's drift time. The trigger system consists of RPC[19]s in the barrel. They are made of two parallel Bakelite plates with a narrow gas gap. This design provides a time resolution of 1.5 ns allowing fast trigger decisions. In the end-caps TGC[20]s are employed which are also multiwire proportional chambers with a 25 ns time resolution. Those parts are integrated in three barrel layers of 5 m, 7.5 m and 10 m radius and four wheels on each side forming end-caps to build tower structures for muon detection. A schematic view of the muon system can be seen in Figure 2.10.

---

[17] Monitored Drift Tubes

[18] Cathode Strip Chambers

[19] Resistive Plate Chamber

[20] Thin Gap Chambers

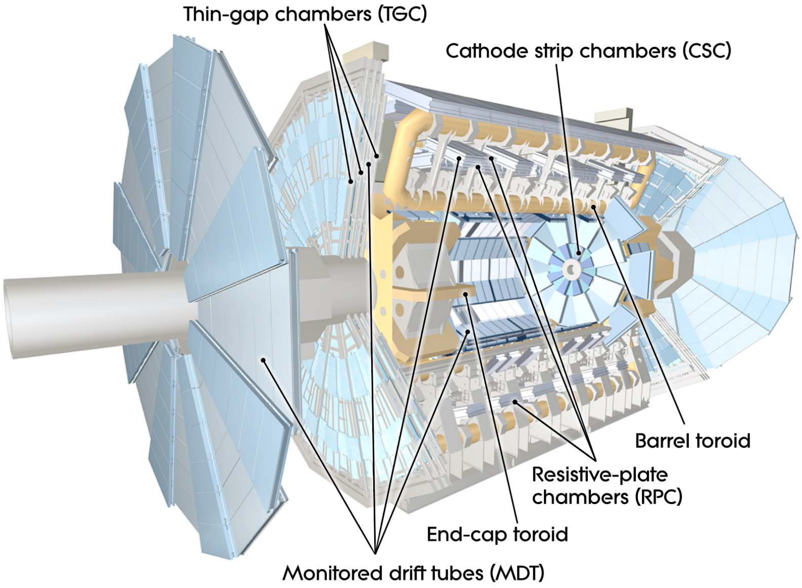

Figure 2.10: ATLAS muon system [19].

Chapter 3

Pixel Detector Upgrade: the IBL project

The LHC will see in the next coming years three major consolidation and upgrade phases which will allow to increase the proton collision energy in the center of mass, to the design value of 14 TeV, as well as the luminosity. These three phases correspond to three long shutdowns: 2013 and 2018 and 2020 [24]. The first one will bring a consolidation of the dipoles to run at the design energy, while the other two are needed to reach a higher luminosity. The period from 2018 to 2022, is called sLHC phase I, whereas the following one is called sLHC phase II. The scheduled machine shutdowns, agreed between LHC and the experiments, and the planned luminosity are shown in Figure 3.1. Having started from a value of around $3 \times 10^{28}\,\mathrm{cm}^{-2}\mathrm{s}^{-1}$, the luminosity has now[1] reached the value of 3.65 10^{33} $\mathrm{cm}^{-2}\mathrm{s}^{-1}$ (at 3.5 TeV). The goal is to reach $1{\times}10^{34}$ $\mathrm{cm}^{-2}\mathrm{s}^{-1}$, and it will double to $2{\times}10^{34}$ $\mathrm{cm}^{-2}\mathrm{s}^{-1}$ (nominal target), that will be reached after two years of operations, see Figure 3.1. In parallel the machine, also the detectors will undergo some upgrades.

The Insertable B-Layer, in shorter IBL, is the first upgrade of the present ATLAS Pixel Detector: it consists in the insertion of a layer of sensors in addition to the existing three layers, to cope with the high level of radiation absorbed by the Pixel Detector (see Section 3.1). It will be placed at a radius of approximately 3 cm, between the new beam pipe and the current inner Pixel layer (B-Layer)[2]. As previously described, the B-Layer is located at a radius of 5 cm and plays a crucial role for the tracking, vertexing, and b-tagging capabilities of ATLAS. Especially at high luminosity, it will decrease its performance and it will suffer the long period of radiation absoption. The shutdown during which the IBL will be installed inside ATLAS will be the first one, in 2013: after that the IBL will be active for physics until the complete ATLAS inner tracker will be replaced, during the long shutdown of 2022.

---

[1] December 2011.

[2] During the compilation of this thesis, the ATLAS Collaboration proposed to replace the whole Pixel Detector, but this proposal has still to be defined and clarified (CERN, IBL meeting - October 19th-21st -2011).

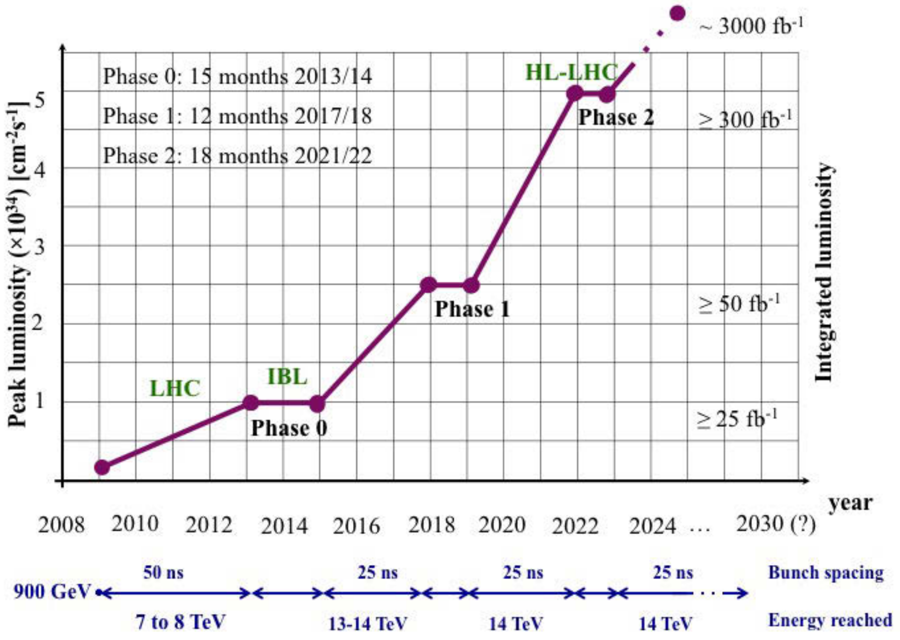

Figure 3.1: Peak Luminosity vs year [25].

3.1 IBL Motivations

The actual Pixel Detector has been designed to face a total dose of 50 MRad, a fluence of 1×10^{15} $\mathrm{n}_{eq}/\mathrm{cm}^2$ and a peak luminosity of 1×10^{34} $\mathrm{cm}^{-2}\mathrm{s}^{-1}$. This means that the expected lifetime for the B-Layer, the ATLAS detector component most exposed to radiation damage, corresponds to an integrated luminosity of about 300 fb^{-1} [26]. With the LHC schedule, the LHC peak luminosity will reach the value of $2{\times}10^{34}\mathrm{cm}^{-2}\mathrm{s}^{-1}$, at the end of Phase I (estimated to be in 2022), as shown in Figure 3.1, and this will generate inefficiency in the Front-End due to the higher occupancy reached.The B-Layer will suffer more than the other layers since it is closer to the beam, therefore the Front-End will have a higher occupancy with the consequence of loosing hits. The expected inefficiency of the present FE-I3 in the B-Layer with respect to the hit occupancy is shown in Figure 3.2. Additional reasons to add a new pixel layer come also from the following: luminosity effects, tracking robustness, tracking precision.

Tracking robustness and radiation doses are correlated to the accelerator luminosity: due to the fact that this last one will increase, a lot of modules might risk to fail. These consequences will be seen first in the B-Layer, due to its closer position to the beam pipe and later on in the other layers as well. As a consequence, the loss of efficiency in the B-Layer will degrade the reconstruction of the collision vertex as well as of the impact parameter resolution, directly affecting the b-tagging. In the other layers, the inefficiency can be (partially) recovered at the level of the offline data reconstruction; learning how to deal with the increased occupancy. The large radiation dose to be absorbed was taken into account when designing the Pixel Detector, in 2002, and already at that time a replacement of the innermost layer was foreseen. Nowadays, after the data taking, it seems

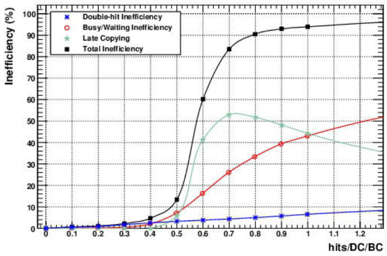

Figure 3.2: FE-I3 inefficiencies [24].

that the dose which will be absorbed until the end of 2012 by the Pixel Detector is not such an issue like it was thought in the past. The dose will affect to a lesser extent the efficiency of the detector. Howver, the dose deposited locally might cause different local problems and has to be taken into account. A certain level of redundancy in the measurement of tracks is required to control the fake rate due to random combinations of clusters in events with high background from pileup. The additional layer with comparably low occupancy helps preserving the tracking performance.

Right behind the project motivations there are strong boundary constraints and projects specifications. To afford the insertion of a new layer to the pre-existing Pixel Detector, a smaller radius is requested. This implies the need to develop a better radiation hard technology for the IBL components, both for electronics and sensors. Said that, a difficulty is given by the very small clearance between the new beam pipe and the existing B-Layer, which does not allow to tilt the modules along the beam in the longitudinal direction z. To reduce the geometrical inefficiency, due to the small available space, the sensors must have either an active edge or a slim guard ring (see Section 4.2.2 in Chapter 4, for details). It was also thought to have a larger new Front-End chip with a chip area five times larger than the present FEI-3, see Section 3.3, that covers an active area which is about 90% of the footprint[3]. An increase of the active area is needed to have a full coverage in the ϕ angle, considering modules with the same active width, but with only one row of Front-End chips. Concerning the pure mechanical part, the small space, available imposes to reduce all the present elements as much as possible. It is then necessary a good engineering plan to allow the removal of the present beam-pipe and the inversion of the new detector with such tight tolerance and clearances. For all these reasons, the services and the IBL itself will have to be made minimizing the material. To reach the goal, very aggressive technology solutions have been taken into account. Starting from the new sensor requirements, the core of the detector, throughout the chip module (with an

---

[3] In the present FE-I3 the active fraction of the pixel modules is 75%.

increased area and radiation harness), to arrive to the stave made of low density carbon foams, more efficient in term of mass flow and pipe size, CO_2 evaporate cooling and electrical power services using aluminum conductors. Thanks to this approach, it is possible to optimize the tracking and vertex performance adding the IBL which ends up to account for 1:5% X0 corresponding to 60% of the B-Layer material budget. In addition to all the previous considerations, one should not forget that the IBL is going to be an intermediate step to the final new ATLAS Pixel Detector replacement, planned for the 2022 shutdown. Developing now the IBL allows to develop and test, in an intermediate step, the technologies, and to better measure and understand the limits of the present detector. The IBL potential to anticipate and recover possible serious failures of the existing B-Layer (or of the Pixel Detector in general) pushes towards having the detector ready as soon as possible. The technologies involved will however require substantial developments and qualification tests. The IBL is scheduled to be ready in the first half of 2015, in time for the end of the long LHC shutdown, scheduled for the end of the same year.

3.2 Layout

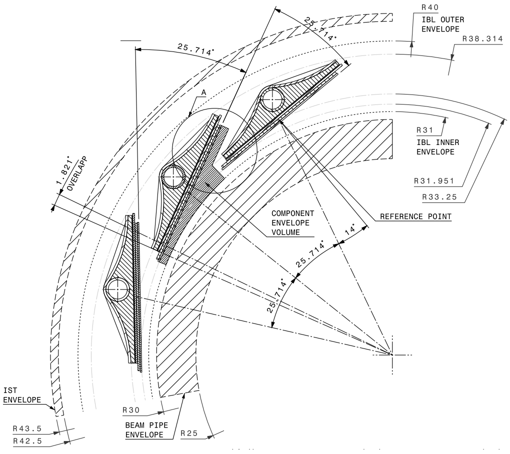

Figure 3.3: IBL Layout: X-Y section viewer [24].

As shown in Figure 3.3 the IBL layout is simple [24]: as the other Pixel layers, the IBL consists of staves, 14, which can cover the circumference in the ϕ-direction[4]. Due to the space constraint (small radius), and to allow the coverange of all the area, the staves are tilted in the ϕ-direction, with an angle between 0° and 27°[5]. Since there is no space along the z-direction it is not possible a partial overlap between module in this direction as shown in Figure 3.4 and Figure 3.5. As a consequence, there is no complete geometrical coverage in the z-direction. This is important to mention, since it will affect the sensor requirements (active

---

[4] A fully hermetic coverage for high energetic tracks is possible.

[5] The orientation is consistent with the other layers, and chosen to reduce the Lorenz angle.

edge), see Chapter 4, Section 4.2.2.
Table 3.1 summarizes the main layout parameters.

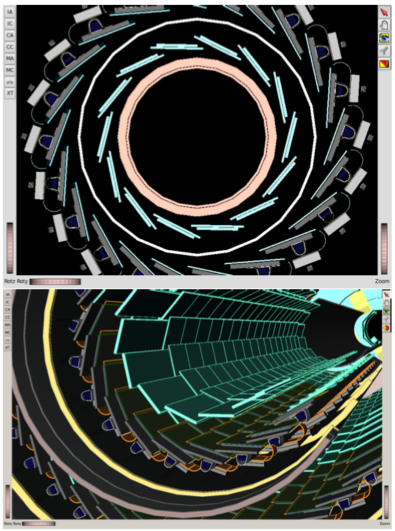

Figure 3.4: Schematic view of the IBL with its modules: (top) XY-view showing the new (smaller) beam pipe, the IBL modules, staves and support tube and the Pixel B-Layer, all implemented in the ATLAS geometry model; (bottom) 3D view of the IBL inside the Pixel Detector illustrating the geometrical arrangement [24].

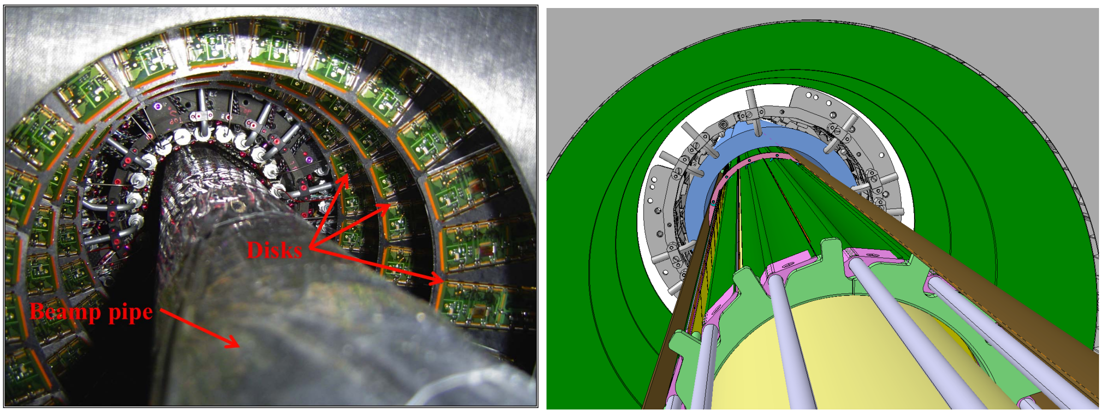

Figure 3.5: (a) Left: Pictures of the Pixel Detector with the inserted beam pipe. (b) Right: rendering of the insertion of the IBL with the smaller beam pipe.

The increasing luminosity is not affecting the sensor design, but it affects the readout electronics: from the Front-End chip to the off-detector electronics. The new FE-I4 Front-End chip will have a completely new internal architecture that fulfills the important request in terms of occupancies and bandwidths

	Value	Units
Number of staves	14	
Number of modules per stave (single/double FE-I4)	32 / 16	µm
Pixel size (ϕ,z)	50×250	μm
Module active size W×L (single/double FE-I4)	16.8×40.8 /20.4	μm
Coverage in η, no vertex spread	$\lvert\eta\rvert < 3.0$	
Coverage in η, 2σ (=112 mm) vertex spread	$\lvert\eta\rvert < 2.58$	
Active z extent	330.15	
Geometrical acceptance in z (min, max)	97.4, 98.8	%
Stave tilt angle in ϕ (center of sensor, min, max)	14.00, -0.23, 27.77	degree
Overlap in ϕ	1.82	
Center of the sensor radius	33.25	mm
Sensor thickness:		
Planar silicon	$150 \div 250$	mm
3D silicon	230 ± 15	mm
Diamond	$400 \div 600$	
Radiation length at z = 0	1.54	

Table 3.1: Main IBL layout parameters.

3.3 IBL Electronics

3.3.1 FE-I4 Chip Architecture

To satisfy the requirements of the ATLAS experiment upgrades, a new Front-End chip has been developed. this project was performed in the Lawrence Berkeley National Laboratory (LBL), Bonn and Genova. This new version is called Front-End Integrated circuit (version) four, or FE-I4, see [24] and [27]. The main motivations to redesign the Front-End can be listed in the following:

(i) due to the small radius (*ii*) and (*v*) increasing luminosity a higher hit rate will be achieve, as shown in Figure 3.2. As a result, the FE-I3 column drain architecture saturates, see [22] and presentation [28] for more details. Therefore a new digital architecture and regional memory is needed in the newest Front-End generation. As shown in Figure 3.9 the new digital logic area shares four neighbours analog parts (or better four pixels neighbours arranged in the so called 'four pixel regions' which store the information until a trigger arrives instead of storing the whole double column information in the EOCL[6]).

(ii) due to the smaller radius, it is necessary to have a larger fraction of active area since, as said, the modules cannot be longitudinally tilted. By increasing the chip are a one should go from 75% (for the actual FE-I3 version) to 90% of active area.

---

[6] End of Column Logic, present in the FE-I3

(iii) having a larger chip brings the benefit to reduce the size of periphery (from 2.8 to 2.0 mm) and the costs (for the past FE-I3 the main cost driver was the flip-chip). Moreover, the Front-End cups will be thinner and with less material.

(iv) the assemblies will be arranged in 2×1 modules instead of 2×8 as before. There will be then an increased flexibility: no need anymore for a Module Controller chip (MCC) since the new generation includes more digital functions.

(v) the increasing luminosity and radiation level require a better radiation hardness that is obtained by shortening the pixel to increase the granularity on one hand (leading to get a better resolution), and to reduce the cross section, on the other hand (to better cope with pile up events).

(vi) thanks to the presence of new technology, a higher integration density for digital circuits is possible. This helps to increase the radiation hardness and consequently to get a smaller power consumption: new analog design for reduced currents, decrease of digital activity (digital logic sharing for neighbor pixels) etc..

(vii) the scaling of the transistors size (130 nm in FE-I4 compared to 250 nm in FE-I3) and the main core transistor layout, increase the total dose radiation tolerance of the chip in order to exceed the 300 MRad specification. Custom layout, triple-redundant memory cells for storing configuration, triplicated digital logic blocks, and hamming coding data buses and storage should protect the chip against damages caused by single event upsets.

The FE-I4 used and tested in this thesis is a first prototype called FE-I4A. A second version, FE-I4B, is ready to be bump-bonded. In this thesis we are going to refer to the prototype FE-I4A as FE-I4. The FE-I4 contains readout circuitry for a total of 26880 hybrid pixels arranged in 80 columns on 250 μm pitch by 336 rows on 50 μm pitch. It is based on 130 nm CMOS technology. The FE-I4 has a larger size than the FE-I3: $19 \times 20\,\mathrm{mm}^2$, as shown in Table 3.2.

Sensors will be DC coupled to FE-I4 with negative charge collection. Each FE-I4 pixel contains an independent, free running amplification stage with adjustable shaping followed by a discriminator with independently adjustable threshold. The chip keeps track of the firing time of each discriminator as well as the Time Over Threshold (TOT) with 4-bit resolution, in counts of an externally supplied clock, [27]. Information from all discriminator firings is kept in the chip for a latency interval, programmable up to 255 cycles of the external clock. Within this latency interval, the information can be retrieved by supplying a trigger. The data output is serial over a current-balanced pair (similar to LVDS). The primary output mode is 8b/10b encoded with 160 Mb/s rate. The FE-I4 is controlled by a serial LVDS input synchronized by the external clock. No further I/O connections are required for regular operation, but several others are supported for testing [27].

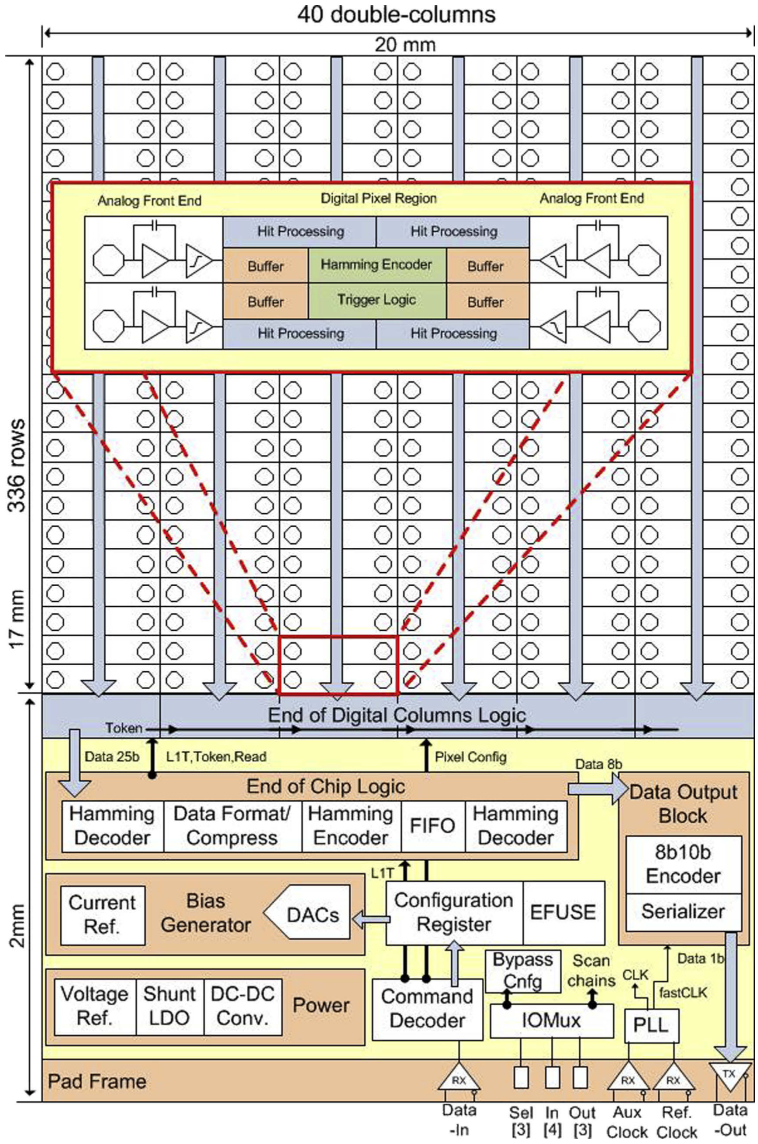

Figure 3.6: FE-I4 layout with a zoom on a single channel [27].

Architecture

The FE-I4 pixel array is organized in column pairs, like the present detector's FE-I3 chip [8], but the read-out architecture is different: instead of moving all the hits in each column pair to a global shared memory structure for later trigger processing, the double columns are further divided into 2×2 pixel regions and each of them contains four identical analog pixels, ending in a discriminator, and one shared memory and logic block called Pixel Digital Region (PDR). The digital region can store up to five events. For each event, the time elapsed since the event was took with 25 nm resolution is memorized thanks to the 40 MHz counter clock (40 MHz is the collision rate). The clock is distributed with a maximum delay of 2 nm due to a possible skew of the clock shape, inside all the network chips. Therefore, in the worst case, when an external trigger arrives a delay of 2 nm is produced. The trigger selects any events for which the time counter matches the

	FE-I3 (ATLAS exp.)	FE-I4 (ATLAS IBL)
Width [cm]	0.7	2.0
Length [cm]	1.1	1.9
Chip Size [mm^2]	82.08	383.8
Active Area [cm^2]	0.58	3.36
Num. pixels	2880	26880
Technology [nm]	250	30
Active Fraction	74%	89%
Rad.-hardness [MRad]	>200	>50
Analog Current [μA/pix]	26	10
Digital Current [μA/pix]	17	10
Analog Voltage [V]	1.6	1.5
Digital Voltage [V]	2	1.2

Table 3.2: Main parameters of the FE-I4 compared to the previous version FE-I3.

programmed trigger latency value. When the counter exceeds the latency without a trigger, the event is erased to make room for more. The events selected by a trigger remain in the region until it is their turn to be sent off the chip via the serial LVDS output. The events are read out sequentially, ordered by time. A “stop” readout mode is also provided where the time counter is stopped and all events stored in every region are read out. This is useful for testing and debugging.

Analog Region

As shown in Figure 3.7 the analog Front-End part is composed by a two-stage amplifier configuration: a preamplifier followed by a second stage of amplification. The first stage is a straight ’cascode’ integrator with a NMOS input device operated in weak inversion. In serie to the output there is a capacitor, C_c, for the AC-coupling which is the input of the second stage: another cascode with PMOS input amplifier. The motivation to have two stages is to optimize the choice of the preamp feedback capacitor (C_{f1}), first stage, and provide enough gain, with the second stage, to the discriminator.

The nominal Front-End current for FE-I4, assuming a 400 fF sensor load, is 10 μA per pixel, while for the present Pixel Detector, scaled to the FE-I4 pixel size, would be 17μA. At the nominal FE-I4 current, the analog time-walk performance is worse than in FE-I3, and in fact a current close to 17 μA per pixel would be required to match the present detector analog time-walk. However, as explained in the next section, the FE-I4 region architecture compensates for the degraded analog timing performance with digital processing. For the ATLAS detector application we define a time-walk figure of merit (“overdrive”) as the charge above threshold at which the delay at the discriminator output is 20 ns greater than for a maximum charge pulse. The FE-I4 overdrive at nominal current is 2000 e^-, while the present ATLAS detector operates with 1500 e^- overdrive.

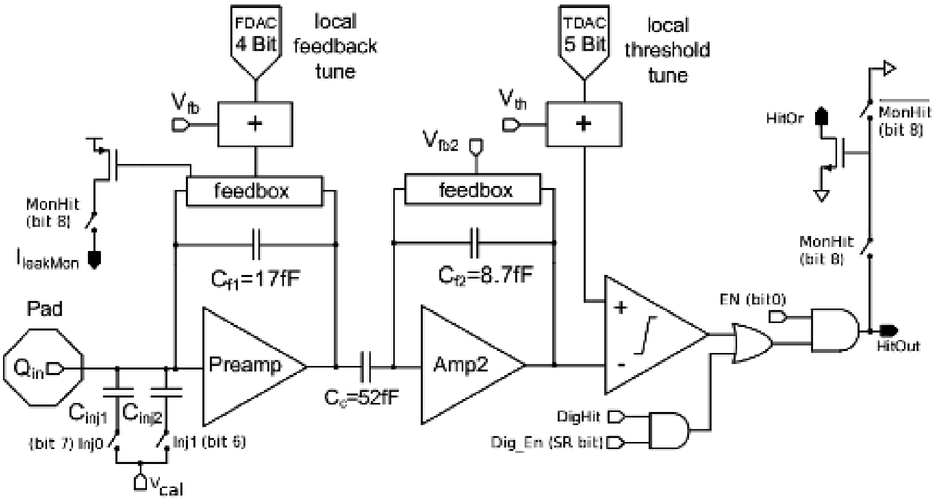

Figure 3.7: Analog Pixel schematic diagram of FE-I4 [27].

Digital Region

The output of the analog region is the input of the digital part. The individual discriminator output is synchronized with the clock as they feed into the digital region. Here all the operations are syncronous: each synchronized output is processed by applying a digital cut on the TOT, see Figure 3.8. The duration of the TOT is measured by counting the cycles of the 40 MHz master chip clock and it is set in units of LHC bunch crossings (25 ns): it is the result of the constant discharge of the feedback current. The TOT is proportional to the deposited charge and a conversion between the two is possible, see Section 3.3.2[7]. TOT can be programmable between one and three clock periods. The Front-End chip digitalizes signal charge from the sensor as shown in Figure 3.7.

3.3.2 FE-I4 Calibration

The calibration procedure allow to set the working point in terms of threshold and charge response, and to make uniform the response throughout the pixels. Consequently the FE-I4s have to be properly calibrated to allow the different sensors to operate correctly. Not all the particles that pass through the sensors produce a hit: the charge collected in the sensor substrate and then read out through the Front-End has to be above certain threshold. Via software is possible to set the calibration, as it will explained better in Section 5.4.1. The digital signal on the Front-End is controlled by the PlsrDAC, a DAC controlling the charge, which generates a voltage pulse V$_{cal}$. For each pixel cell, V$_{cal}$ injects the charge into the injection capacitor C$_{lo}$ or C$_{hi}$[8], see Figure 3.7. Therefore, the pixel preamplifiers

---

[7] It must be stressed that for the present FE-I3 Front-End chips the TOT to charge conversion factor is available and the procedure how to calculate it is known [29], but for the FE-I4 version is still under studying and therefore not available yet.

[8] For the present ATLAS Pixel Detector, C$_{lo}$ or C$_{hi}$ are used, while for the FE-I4 are these renamed as C$_{inj1}$ and C$_{inj2}$ as in Figure 3.7.

see a signal equivalent to a signal generated by a charge $V_{cal} \times C_{lo/hi}$. The signal shapes of the Front-End preamplifier output and the discriminator output signal is shown in Figure 3.8 (a).

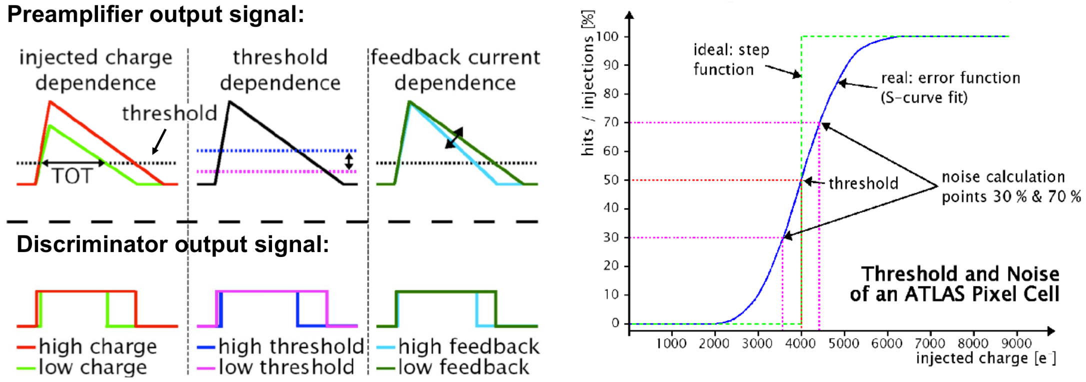

Figure 3.8: Preamplifier and discriminator output signals (left) and Pixel Cell Threshold (right) [30].

The number of collected hits versus the injected charge is recorded after the STControl scan. Ideally, a step function with an immediate transition of the detection efficiency from 0 to 100% at the threshold target should be desirable. In practice, as shown in Figure 3.8, in real detectors this never happen. Due to the presence of noise (e.g. preamplifier noise), some injected charges are below the threshold while some others are not. The best way to describe this behavior after the discriminator output is via the *error function*: a convolution of the ideal step function with the Gaussian pixel noise distribution.

$$f_{error}(x) = \frac{1}{\sqrt{2\pi}} \int_0^x e^{-t^2}\, dt \tag{3.1}$$

with $t = \frac{x-\mu}{\sigma}$.
Therefore, the threshold value of a pixel is defined at the 50% hit efficiency value of the error function, as shown in Figure 3.8 (b). On the contrary, the noise (σ) of a pixel is inversely proportional to the steepness of the transition from no detected hits to full efficiency, and is calculated between the 30% and 70% points of the error function as:

$$\sigma = \frac{Q_{70\%} - Q_{30\%}}{f_{error}^{-1}(70\%) - f_{error}^{-1}(30\%)} \tag{3.2}$$

with: f_{error} error function normalized to one, and Q injected charge.

The probability of detecting a charge is consequently giving by the following formula:

$$P_{hit}(Q) = \frac{1}{2} Erfc\left(\frac{Q_{thr} - Q}{\sqrt{2}\sigma_{noise}}\right) \tag{3.3}$$

with

$$Erfc = \frac{2}{\sqrt{\pi}} \int_0^{\infty} e^{-t^2}\, dt = \frac{1}{\sqrt{\pi}} \int_0^{\infty} e^{\left(\frac{Q_{thr}-Q}{\sqrt{2}\sigma_{noise}}\right)^2}\, dt \tag{3.4}$$

$$Erfc = \frac{2}{\sqrt{\pi}} \int_x^{\infty} e^{-t^2}\, dt \tag{3.5}$$

Threshold and noise can be derived from this fit, and together with the TOT distribution they are used to characterize the Frond-End chip and also the assemble. In fact, due to differences during the production, the Front-End do not have all the same threshold and noise with the same configuration settings, and in this state the chip is so called untuned. Moreover, to satisfy the tracking requirements and the way to operate with the detector, it is possible and necessary to set different parameters to operate under the desired conditions. This can be done as explained in the following:

Threshold:
a local voltage offset can be added via the threshold tuning DAC (TDAC), a 5-bit register which locally set the voltage. In addition, other three global parameters are involved to set the threshold [31]: Vthin, a 8-bit register which controls the Vthin_C output current (usually set to value 255 to use the temperature compensated Vthin_C voltage[9]), Vthin_Alt (Coarse and Fine), a 16-bit register which controls the Vthin_C output voltage (divided in eightLSB[10] bit for the Vthin_AltFine field, a non linear adjustment, and eight MSB[11] for the Vthin_AltCoarse field), and finally the TdacVbp a 8-bit register which influences indirectly the threshold by changing the TDAC LSB size.

TOT:
There is a global 8-bit register, PrmpVbpf, which controls the master feedback current of the preamp. It sets the fall time of the preamp output which in turn determines the ToT LSB scale; locally, the FDAC 4-bit register for each pixel, and indirectly the last one, like TdacVbp, for the threshold, the register FdacVbn, a 8-bit register to be able to change the step size (LSB) for the in-pixel amplifier feedback current DAC.

---

[9] The pixel threshold itself has a known temperature dependence, and a different configuration must be used to have a temperature stable threshold, see [31] for more details. The full scale value is around 25 μA.

[10] Least Significant Bit.

[11] Most Significant Bit.

3.4 IBL Sensors Technologies

The IBL modularity will be different: the physical size will depend on the chosen sensor technology and three different technologies have been proposed: planar, 3D, and diamond [24]. The 3D technology, being the core of the work presented in this thesis, will be explained in more details in the next Chapter 4. Due to its large dimensions, one planar sensor requires two Front-End chips (2-chip module), while for a 3D sensor only one chip (1-chip module) is needed.

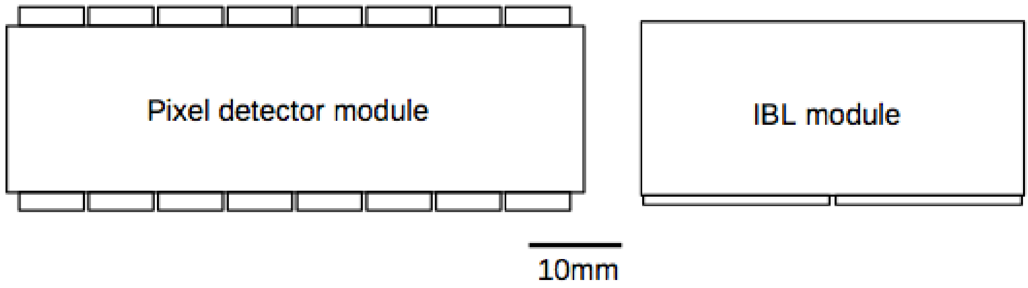

Figure 3.9: Comparison between the footprints for the present Pixel Detector bare module and for the IBL 2-chip module on the same scale, as viewed from the sensor side [24].

The IBL design assumes an integrated luminosity of 550 fb^{-1} and a peak luminosity of 3×10^{34} cm^{-2}/s to determine the sensor requirements. Including a conservative safety factor of two, this translates into an ionization dose of 250 Mrad and into a NIEL dose of 5×10^{15} $\text{n}_{eq}/\text{cm}^{2}$[12] [32]. As summarized in Table 3.3, up to this fluency the IBL is required to provide a hit efficiency in the active area >97% and a r - ϕ resolution better than 10 μm for minimum ionizing particles. Other IBL constraints are the operational temperature, set to -15° C, and the maximum sensor bias voltage, set at 1000 V. The power dissipation should not be above 200 mW/cm^2 at the nominal temperature, and concerning the sensors design one has to minimize the dead regions, in order to achieve the target inactive edges of 200 μm.

3.4.1 Planar Sensors

The planar pixel sensors are based on the well know technology of the current planar ATLAS Pixel Detector, [33] which has been used as a starting point to develop the n^{+}-in-n planar sensors. Many more planar sensors have then been produced and characterized with a reduced number of guard rings, with a smaller safety margin between the outmost guard ring and the dicing street, and also with pixels that were shifted stepwise underneath the guard rings [34]. But, at the end,

---

[12] Non-Ionizing Energy Loss (NIEL): is a quantity that describes the rate of energy loss due to atomic displacements as a particle traverses a material. NIEL damage for sensors is conventionally quoted as the equivalent damage of a fluence of 1 MeV neutrons ($\text{n}_{eq}/\text{cm}^2$).

	Specifications
Power dissipation	< 200 mW/cm^2
Leakage current	< 100 nA/pixel
Operational temperature	-15° C on sensor
Inactive edges	< 450 μm
Thickness	between 150 and 250 μm
Hit efficiency*:	$> 97\%$

Table 3.3: Main IBL specifications to qualify the IBL sensors. Hit efficiency: after a benchmark fluence of 5 $\times 10^{15}$ n$_{eq}$/cm^2 at a maximum bias voltage of 1 kV.

with the new IBL installation schedule in 2013, only two layouts were supported from the planar community to be used with the new Front-End: one conservative design with 13 instead of 16 guard rings[13], similar to the old design but following the IBL specifications, and one design where the outermost pixel implants on the front side are extended to a length of 500 μm[14]. The planar sensors are based on diffusion oxygenated FZ[15] silicon bulk. The sensor thickness chosen for the IBL is 200 μm (less than the present Pixel Detector thickness of 250 μm). Isolation

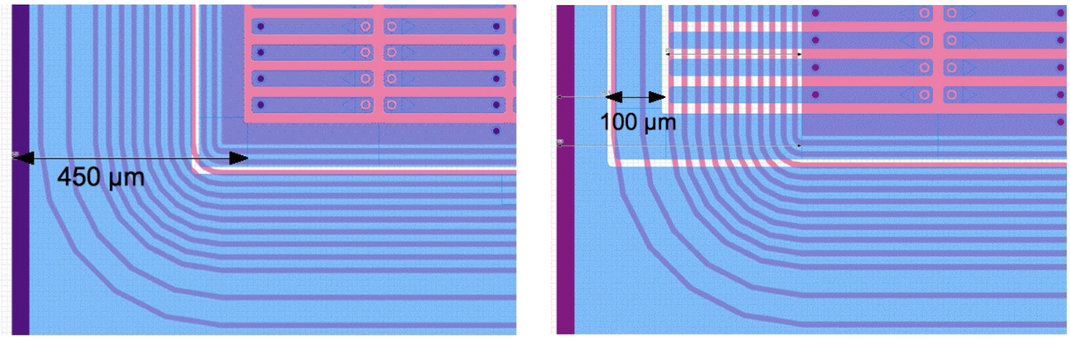

Figure 3.10: Conservative layout design and slim edge for planar n$^+$-in-n silicon technology [24]. On the left it can be seen that there are 13 guard rings (reduced from 16 of the actual ATLAS Pixel Detector) with an inactive edge of 450 μm. On the right the detail shows that the outermost pixel implants are extend to a length of 500 μm, respect to the normal size of 250 μm, over the ohmic side guard rings. Therefore the total inactive edge is about 200 μm.

---

[13] The number of guard rings is chosen to obey to the IBL condition of the limit of 450 μm of inactive edge.

[14] In order to reduce the inactive edges, the planar IBL design shifts the guard rings on the ohmic side beneath the outer pixels. This solution introduces a distortion of the electric field on the sensor edge, but the charge collection after irradiation occurs primarily in the region directly beneath the n$^+$ implant [35].

[15] Float Zone or Floating Zone (FZ): used primarily for applications in which very high resistivity or the absence of oxygen are necessary for a good device performance. Some examples of FZ silicon main applications are: discrete power devices, high efficiency solar cells, RF-wireless communication chips and optical products.

between the n^+ implants is obtained through the moderated p-spray technique. A bias grid [33] is integrated into the design to determine the sensor electrical quality before bump-bonding. The inactive edge of planar devices achieved with this design is around 200 μm. The planar IBL sensors are produced at CiS [36] (Germany), which also supplied ATLAS with the sensors for the current Pixel DetectorPixel Detector.

3.4.2 Diamond Sensors

It has been proposed to build a detector with diamond sensors instead of Silicon ones. As already mentioned in Chapter 1, Section 1.1, due to the diamond high energy gap (5.5 eV) compared to the one (1.12 eV) of Silicon, the intrinsic carrier generation is very small, see Table 3.4. Therefore, the advantages of using this material is the very low leakage current. This permits to work with the sensors at room temperature without thermal runaway problems (an increasing leakage means an increasing temperature which again causes an increasing current). On the contrary, the main disadvantages of the diamond technology with respect to Silicon is the low signal size. A MIP particle that crosses the diamond sensor will generate almost four times less charge than in a Silicon detector. The processing does not need any implantation but just a metal deposition to define the electrodes to bias the sensors itself. Moreover, the collected charge of a diamond sensor it is half of that from an equal thickness Silicon detector: this makes necessary to operate with a read-out electronics that works at very low threshold. Therefore, the advantages of having a lower pixel noise, thanks to a smaller dielectric constant compared to Silicon (5.7 against to 11.9), helps to keep a lower threshold operation. In fact, the capacitance is smaller compared to 3D and planars (again, because of the lower dielectric constant). In particular, after irradiation it was not noted an increase of noise (S/N $\sim$ 50) [24]. Due to the higher atom displacement energy (43 eV/atom compared to the value for Silicon sensors of 13-20 eV/atom), diamond is intrinsically more radiation hard than Silicon.

However, despite the good advantages, diamond sensors have not been considered as the final chiose for the IBL project [37]. The higher cost and the difficulty to ensure a uniform production for the IBL requirements have caused its exclusion. The IBL will require a sensor area almost two orders of magnitude bigger than of the diamond sensor detectors produced up to now. On the contrary, diamond sensors have been choosen for the Diamond Beam Monitor (DBM) [38].

At the moment there are 22 institutes involved in the development of diamond sensors, grouped in the so called R42 Collaboration.

Property	Diamond	Silicon
Energy Band Gap - E_g[eV]	5.5	1.12
Breackdown field [V/cm]	10^7	3×10^5
Intrinsic resistivity [Ω cm]	$>10^{11}$	2.3×10^5
Intrinsic carrier density	$<10^3$	1.5×10^{10}
Electron mobility μ_e [cm^2/Vs]	1900	1350
Hole mobility	2300	480
Saturation velocity	1.3 (e)-1.7 (h)$\times 10^7$	1.1 (e)-0.8(h)$\times 10^7$
Density	3.52	2.33
Atomic number - Z	6	14
Dielectric constant - ϵ	5.7	11.9
Displacement energy [eV/atom]	43	13-20
Thermal conductivity [W/mK]	~2000	150
Energy to create e-h pair [eV]	13	3.61
Radiation length [cm]	12.2	9.36
Spec. Ionization Loss [MeV/cm]	6.07	3.21
Aver. Signal Created / 100 μm	3602	8892
Aver. Signal Created / 0.1 X_0 [e_0]	4401	8323

Table 3.4: Comparison between diamond and Silicon sensors. The values given refers to a temperature of 25° C.

Chapter 4

3D Pixel Detectors

3D silicon technology is one of the technologies chosen for the ATLAS IBL. In contrast with the planar technology, which have the electrodes implanted 'on' the substrate surface and restricted to be within a few microns from the wafer's top and bottom surfaces, the 3D architecture has the electrodes perpendicular to the wafer's surface. A schematic view of a full 3D sensor is shown in Figure 4.1. The dotted line box emphasizes one typical 3D cell layout (considering the case for the ATLAS FE-I4 pixel layout): the n^+ columns, drawn in red in the picture, are the readout electrodes or junction electrodes, while the p^+ columns drawn in blue are the ohmic electrodes or bias electrodes. As the planar, the 3D sensors are reverse biased but while in the planar sensors the electric field is growing largely perpendicular to the surfaces (the power supply is provided between the two surfaces) in 3D sensors this happens in the parallel direction, see Figure 4.2. In the 3D architecture the bias voltage is applied from the p-electrode (+) to the n-electrode (−) to create the necessary depletion voltage. The substrate could be a silicon n-type or p-type doped.

In this chapter, a summary of the main advantages and a short history of the evolution of the 3D technology are given, together with a description of the 3D sensors chosen for the IBL project. A detailed description of the 3D devices tested and characterized at CERN by myself will be presented as well.

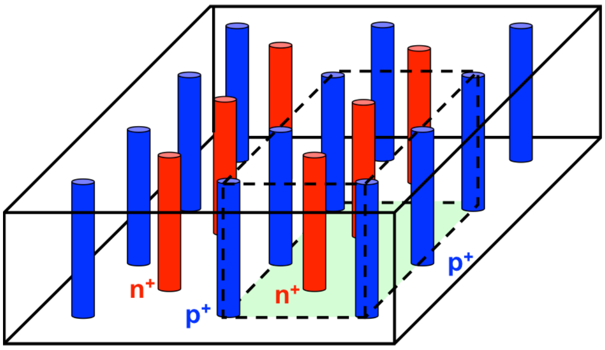

Figure 4.1: 3D layout: three dimensional view of a typical pixel structure. The internal box drawed with a dotted line represents a typical cell, for the ATALS FE-I4 pixel layout application, named "two electrodes" (or 2E): this consist of two n-columns readout around six ohmic p-columns.

4.1 3D Pixel Detector Features

The 3D architecture is a combination of standard planar technology and micromachining. Compared to traditional planar sensors, for which electrodes are processed on the wafer surface, 3D design has several important distinguishing features that are listed in the following, with he help of Figure 4.2:

(i) higher average electric field between the electrodes: in 3D case, the depletion region proceeds laterally between the columns, Figure 4.2 (b)), while in a planar sensor the depletion region proceeds vertically[1]. As consequence, in the planar case the full depletion voltage depends on the substrate thickness, while in the 3D detectors the decoupling from the substrate thickness allows to have a higher electric field. In fact, the distance between the columns ranges is between 56 and 103 μm, see Figure 4.3, compared with the 200 μm for planar sensors. Therefore, the full depletion voltage, which is a function of the electric field, depends as well on the electrode distance. For the 3D sensors the latter can be one order of magnitude smaller than the detector thickness: it decreases with the square of the electrode distance. As an example, an inner-electrode distance of 30 μm has a full depletion voltage 100 times smaller than a 300 μm thick planar silicon detector [39].

(ii) shorter collection path: in 3D detectors, the electrodes have the same distances, see Figure 4.3, which is smaller than for a planar sensor. Therefore, a charge generated by one ionizing particle is collected in a much shorter time, as shown in Figure 4.2 [40].

(iii) higher signal to noise ratio: the short collection path have the effect to increase to signal strength due to the decrease of the recombination of carriers. This leads to have an higher signal to noise ratio, despite the increasing noise (due to the higher capacitance for the short distance). In the presence of significant charge trapping and poor charge collection efficiency, such as for diamonds and GaAs devices [41], the performance can be improved.

(iv) advantages in extreme radiation environments: the charge carrier drift-length is decoupled from the sensor thickness. In fact, irradiating silicon structures with high fluences produces damage centers and this increases the voltage required to fully deplete a silicon detector. Thanks to the small collection distance, the trapping probability at high fluences is reduced with respect to standard planar sensors. 3D-sensors can be still fully depleted after having been irradiated with high fluences, since the distance between the electrodes (of opposite type) is smaller [42], [11].

(v) the sensor edge can be an electrode (see Figure 4.2) or one can use etching trenches technique (see following Section 4.2.2): this is an important feature to decrease the dead volume area at the edges. For comparison, the planar sensors use guard rings.

---

[1] the electrode surface geometry is larger for the 3D sensors with respect to the planar sensors and the average electric field is higher than the peak value for the planar.

(vi) lower charge sharing: thanks to the electrodes configuration that provides high shielding effect.

The main features for planar and 3D-sensors are shown in Table 4.1.

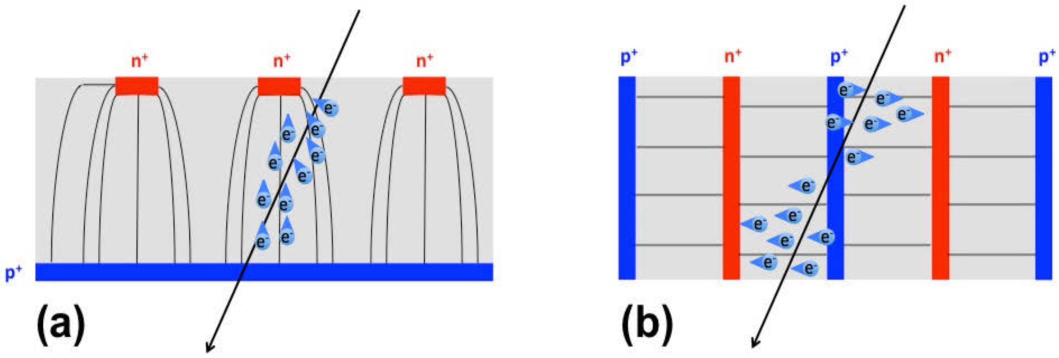

Figure 4.2: Scheme of the geometry and of the charge collection mechanism for the standard planar (a) and 3D-sensor (b), not in scale.

Thanks to the features listed above, the main advantages of the 3D-detectors can be summarized as:

1. *high efficiency and radiation hardness*: as already reported in Chapter 1 Section 1.8, the most important radiation damage is the bulk damage: acting to reduce the collection path will reduce this unwanted effect (especially the charge trapping). The high electric field and the short collection path increase the efficiency due to the reduced space between the electrodes (see [43] for more details). More precisely, after irradiation, the higher is the electric field, faster the charge can be collected to the electrodes, reducing the probability of charge trapping in the bulk. The inter-electrode distance in a planar technology corresponds to the sensor thickness itself, while for 3D sensors is the distance between the columns. If we consider a 3D sensor 25×62.5 μm as a basic rectangle p-n cell, the distance between the n^+ and p^+ electrodes is 67.32 μm which is extremely low compared to the 250-300 μm of the planar case. Indeed, if a particle is created in the middle between the two electrodes, the charge under the electric field will move $\sim$33.6 μm (for the 3D), compare to the 115 μm (for the planar).

2. *lower depletion voltage*: the short collection path implies a lower full depletion voltage. Moreover a lower power dissipation is required. This is extremely important for the IBL project since the cooling system had a lot of problems in the present Pixel Detector. Indeed, keeping the same sensor thickness, the depletion voltage will be lower (e.g. 200 V respect to 1500 V planar case after irradiation).

3. *faster charge collection*: when an ionizing particle generate charges, they move to ward the electrodes under the electric field, following a parallel direction, and reach them almost at the same time. Considering the short

distance involved, the corresponding charge pulse produced is large pulse with a fast rise-time. For the planar sensors the same ionizing particle originates different collection times for the carries, see Figure 4.2.

4. *active edge*: thanks to explained in *(v)* the dead area at the sensor periphery is reduce to a few μm [44, 45], whereas in modified-3D sensors, see Section 4.2.2, a slim edge of a few hundreds of μm can be achieved [44].

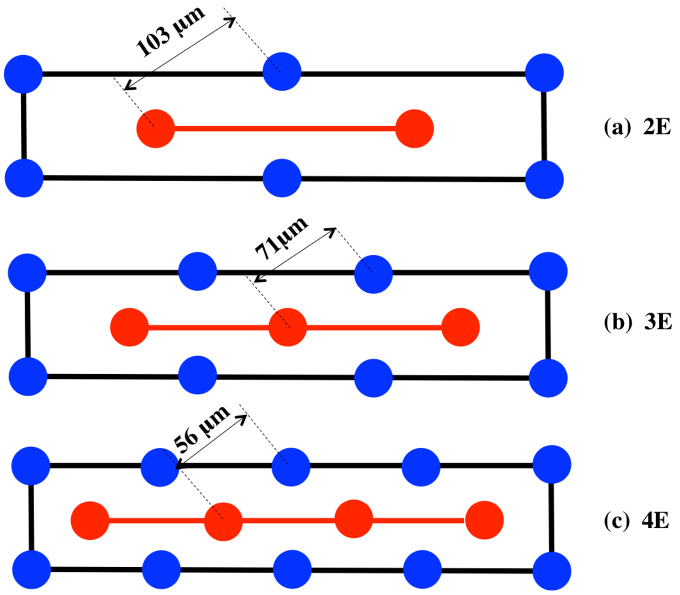

Figure 4.3: Schematic view of the different 3D layout configurations with 2, 3, and 4 read-out electrodes per pixel.

	Planar	**3D**
Electric Field	perpendicular to the surface	parallel to the surface
Depletion region	vertical: depends of the substrate thickness.	horizontal: depends on the electrodes distance (distance between the readout and ohmic columns).
Collecting Charge Distance	strongly dependent from the substrate thickness.	depends on the electrode distance. Small if compared to the planar case since the distance is lower.
Radiation Hardness	high	very high
Active Edge	guard rings	yes
Charge Sharing	higher	lower than planar
Dead Region	-	along the electrodes
Depletion voltage	Order of tens of V.	Less than 10V.
Edge sensitivity	< 5 μm	$\sim$400 μm
Charge 1 MIP (300 mm)	24 ke$^-$	24 ke$^-$
Capacitance	30-50 fF	20 fF
Collection distance	200-300 μm	$\sim$50 μm
Speed	1-2 ns	10-20 ns

Table 4.1: Summary of the main features for planar and 3D pixel sensors [46],[47], [48]

4.2 Evolution of the 3D layouts

The 3D architecture was originally proposed by Parker *et al.* in 1997, that is more than ten years ago [49]. The electrodes in 3D detectors were fabricated by etching holes in a silicon substrate, typically with the Deep Reactive Ion Etching (DRIE) technic, then filling them with polysilicon [50]. This makes 3D sensors considerably more complicated to produce than traditional planar sensors. A 3D detector has three dimensional electrodes that penetrate entirely or partially in the detector bulk, perpendicularly to the surface. Electrodes can be arranged to form pads, strips or pixels, depending on the application. The 3D silicon technology is a complete different and innovative technology compared to the standard planar one. It is a combination of two well established industrial technologies: Microelectro-Mechanical Systems (MEMS[2]) and Very-large-scale integration (VLSI[3]), where electrodes are fabricated inside the silicon bulk instead of being implanted on the wafer surfaces. 3D sensors, are currently fabricated at different processing facilities in Europe and USA. The first 3D silicon pixel detector has been the Stanford detector (USA), see Figure 4.4 (*a*), which is considerate the reference technology with full passing through columns. This approach requires a support wafer which will need to be removed, see next Section 4.2.1. Following, SINTEF [51] has fabricated the 3D thanks to a technology transfer. Afterwards, others facilities have proposed alternative approaches which are briefly summarized in the following:

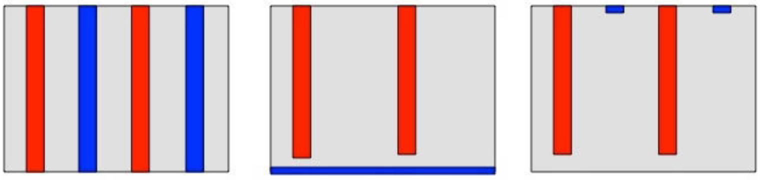

(a) Stanford, SINTEF (b) FBK, VTT (c) BNL

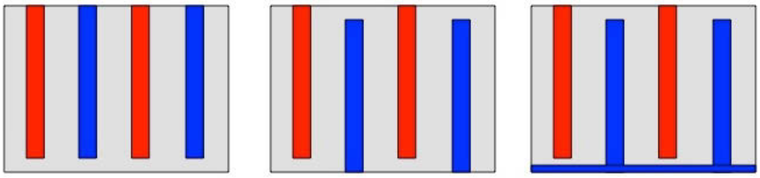

(d) BNL (e) CNM (f) FBK

Figure 4.4: Different type of 3D architectures proposed by different research groups.

---

[2] Technology of very small mechanical devices driven by electricity

[3] A process of creating integrated circuits by combining thousands of transistors into a single chip. VLSI began in the 1970s when complex semiconductor and communication technologies were being developed. At present (2011) cutting edge technology is able to integrate up to three billion transistors on a single chip (dimension of the transistor 45 *nm* in the better case, in laboratory 32 *nm*). All the microprocessors are VLSI devices.

(b) semi-3D detector, initially proposed by Fondazione Bruno Kessler (FBK [52], Trento) and VTT [53] (Finland) in 2004 and independently developed. This approach consists of having only one doping type columns not all the way through the wafer, with blank implantation on the back for the ohmic contact. The sensors fabricated at VTT have been electrically tested, before and after a proton irradiated fluency of $6 \times 10^{15}\, cm^{-2}$ [54]. The semi-3D pixel detectors were also characterized with the MEDIPIX2 readout chip, showing a higher energy resolution with respect to planar sensors [55]. The development of semi-3D detectors ended in 2005. At the moment VTT has kept on developing 3D technologies with the aim of fabricating and testing edgeless microstrip detectors on six inch silicon wafer [56]. The FBK architecture will be discussed in the next Section 4.3.2 since it is related to the main part of the work done for this thesis.

(b) alternative semi-3D detectors in a second alternative: column electrodes of only one type, etched from the top, proposed by the Brookhaven National Laboratory (BNL) at the end of 2005 [57]. In another variant, p^+ and n^+-columns electrodes are etched on the same side and not penetrating all the way through the substrate as proposed again by BNL (d). Simulations have been performed with 3D-TCAD to study the full depletion voltage and the charge collection after irradiation. Results are reported in [58] only for the static IV characteristics (see Chapter 5, Section 5.5.1) of single type column prototypes.

(e-f) Double sided 3D detectors: proposed by CNM [59] and FBK [60] independently, with of course few differences in the fabrication process. The basic idea is to have the columns etched from the opposite sides of the wafer for each electrode type and not passing through the entire thickness so that no support wafer is needed. More details of the advantages of such detectors are described in the next chapters since their laboratory characterization is the core of this thesis.

4.2.1 3D fabrication technology with support wafer

A summary of the steps needed to produce 3D sensors is shown in Figure 4.5. Not all the process steps are included but just the most important phases which distinguish a 3D detector fabrication from a standard planar one [44, 50].

With the aid of Figure 4.5 the whole process can be summarized as follows:

(a) A support wafer is bonded through an oxide layer to the substrate wafer where the detector will be made. This allows the detector wafer to be back-thinned to any desired thickness [50], and processed without additional yield losses due to accidental cracking. Bonding the bonding support wafer, the top wafer can be protected with photoresist, primarily to protect the region near the edges, then placed face down in an etcher while the support wafer, now on top, is etched off.

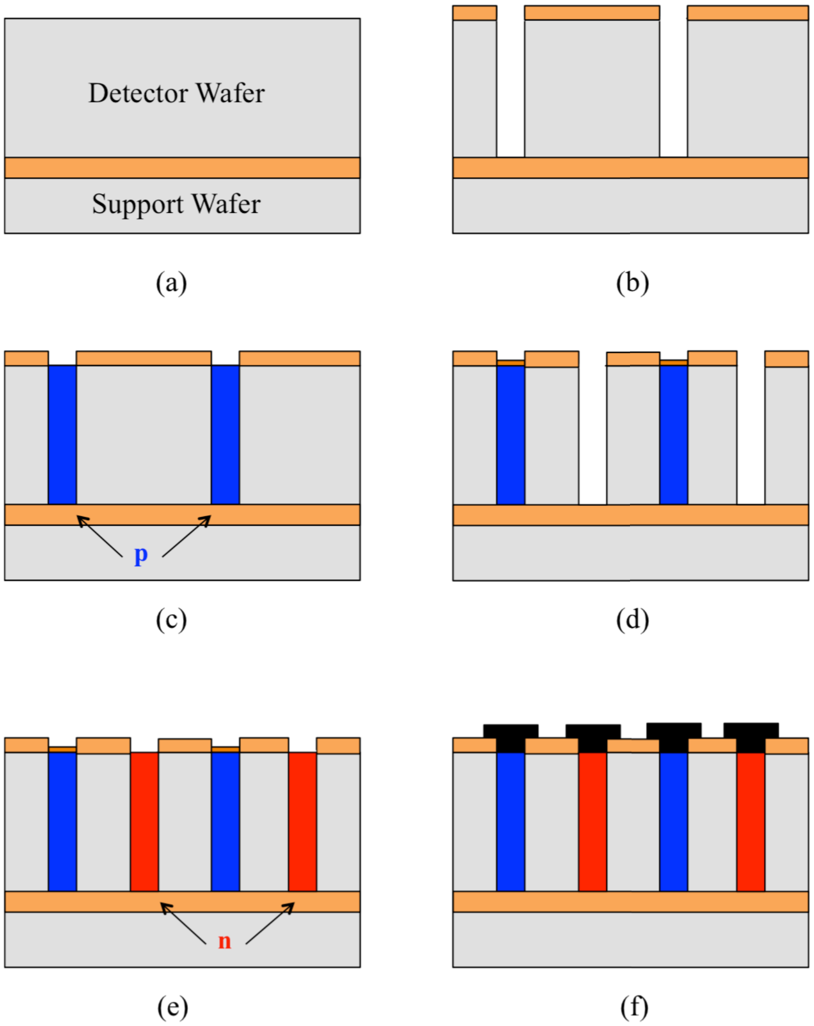

Figure 4.5: 3D fabrication steps.

(b) The windows where the electrodes columns will be patterned and then the p^+ electrodes for the whole detector thickness are etched.

(c) The p^+ electrodes holes are filled with polysilicon deposition by low-pressure chemical vapor deposition. The low pressure increases the main free path of the Silane molecule, so that the exposition to polysilicon is uniform along the holes. Silicon is doped so that junction electrodes are created.

(d) A thin layer of oxide protection is deposed on the p^+ electrode and then the n^+ electrode is etched.

(e) Holes are filled with polysilicon and columns are doped with phosphorus which also acts as a getter site. The readout electrodes are now created.

(f) Aluminum is pattered and deposited for the electrode connection to the desired geometry configuration.

4.2.2 Active Edge

One of the main features of 3D technology is the active edge, as already explained in this chapter in Section 4.1. In order to have a strong reduction of the dead area compared to the planar sensors, a wall electrode around the sensor, right at the border of it, can be realized, see Figure 4.6 and Figure 4.7, [44]. The existing ATLAS Pixel Detector, for example, has an active region of only 80-85% of the total area [50]. In fact, planar pixel detectors need multiple guard ring structures at the cutting edge of the silicon in order to prevent high leakage currents coming from the edge of the chip flowing into the active area, to smooth electric field from the active region to edge and for the confinement of the depleted region (sensitive area), as already discussed in Section 3.4.1. Guard ring structures should be at least as wide as the detector thickness to be effective so, the dead layers is on average few hundreds of microns (see Figure 3.10) [16]. Thanks of using the DRIE process 3D sensors can be diced by etching trenches. Basically, making these trenches at the border of the sensor, they can be doped and filled with polysilicon to act as p^+ or n^- electrodes. The result of such a technique is optimal: a detector with an extremely reduced and thin dead zone[4]. This gives great advantages for applications where several detectors have to be stacked together to cover large area. The new design scenario allows to save material since there is no need of an overlap between one detector and the other. Moreover, an active edge can be realized also on planar segmented detector where 3D architecture is not necessary, but saving material is the main concern. As a matter of fact, this design is appealing for the IBL project where the restricted available space could be critical, but it will not be used. The masks for the first fabrication run were made before the support wafer technique was adopted, therefore no active edge sensors design was included. However, one with wall electrodes, alternating to the normal cylinder electrodes, were included. For the wall electrodes fabrication steps similar to those for the active edge sensors are used. The additional steps needed for active sensors, mainly the etching of the dicing trends and the removal of the backing wafer, are done at relatively low temperatures and would not be expected to change the dopant distribution, the resultant electric fields or the sensors performance significantly. The near-edge performance of the active edge sensors should be similar to the near-cell-edge performance of the active edge properties.

Unfortunately an active edge has several complications: it requires a support wafer and consequently the backside of the sensor wafer is not accessible, and even worst is not compatible with the double-sided process, described in detail in Section 4.3.1.

---

[4] Basically there is no dead layer compared to the planar case.

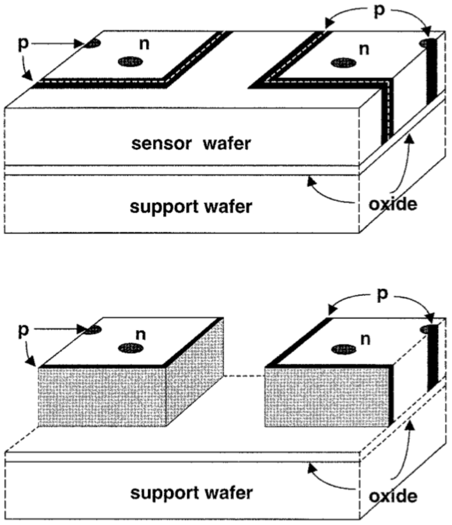

Figure 4.6: Schematic view of the corners of two active edge sensors fabrication processes with support wafer (not in scale) [44].

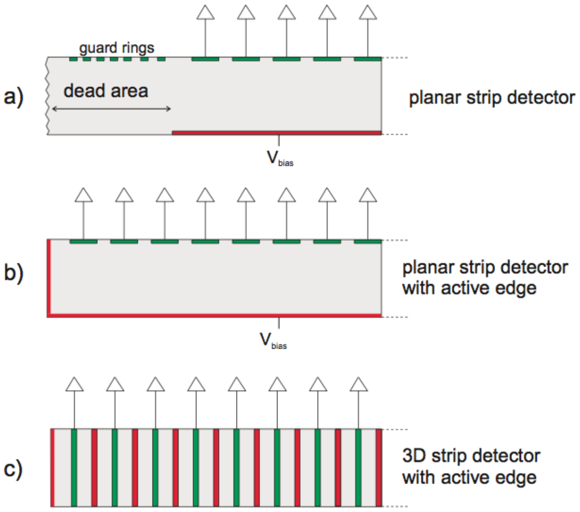

Figure 4.7: Different active edge layouts to decrease the dead area at the sensor border. (a) planar strip detector, (b) planar strip detector with active edge and (c) 3D strip detector with active edge.

4.3 3D-FBK History

As previously described and shown in Section 4.2, the process technology behind the 3D sensors is relatively new, it requires several steps that are not commonly used in standard detector technology and it is continuously developing: this is one of the main reasons why they are not yet so widespread used in high energy physics and imaging. Consequently the yield is not so high as for the planar processing (which is well known). However the technique to produce 3D sensors is improving and getting better and better with years and experience. For future mass production of 3D devices very critical will be the fabrication yield[5] and the costs involved. To give some numbers, at the time of the writing of this thesis the planar yield is around 80%, while the 3D yield is around 60-70%, which is an exceptionally good result for a new technology with a complexity process as is the case of 3D sensors. Since the beginning, different designs have been studied and different facilities worked on them. While the full-3D sensors fabricated at Stanford [61] and in parallel at SINTEF [51] presented fully penetrating electrodes, the modified-3D sensors fabricated at Centro National de Microelectronica (CNM) of Barcelona, Spain [62] where characterized by electrodes which do not penetrate the entire substrate thickness. In parallel, the FBK in Trento, Italy [63], started to produce modified-3D sensors, not full penetrate, to end up producing the full penetrating electrodes. As it will be explained in Section 4.5, for the IBL project only the production from FBK and CNM has been considered. Here the history of the 3D-FBK devices is shortly described. Due to the difficult production process and required technology to fabricate the 3D sensor, FBK has decided to start with the production of Single-side Single Type Columns (SSTC), in 2004-2006 [52, 64]. The readout electrodes were edged from the top surface, while the bias electrode is basically spread along the whole back side, as shown in Figure 4.8 (a). The proposed architecture is a combined planar electrode of p^+-type inside a p-type bulk with n^+ columns used to readout the signal. In this way, the fabrication was much simplified and a first step was made to allow new manufacturers to work on the devices using micromachinine technology. In fact, the advantages of this first solution consisted in a considerable simplification of the fabrication process: the column etching and doping was performed only for the readout electrodes, therefore only once. The disadvantage was that it prevented the control of the electric field value with the applied voltage when the full depletion was reached. As a result, the low-field regions might have a larger extension compared to the original full 3D detector architecture. The only free parameter to control the electric field was the appropriate substrate doping concentration.

After few years, in 2007-2009, the Double-side Double Type Columns technique (DDTC) have been developed: columns of both doping types are etched from the two sides of the devices: the readout columns, n^+, are etched from the front-side and the other type, p^+-type, ohmic from the back side. The micromachining used in MEMS is applied to etch deep and very narrow apertures within the silicon wafer using the Bosch process [65], followed by a thermal diffusion process to drive dopants to form the n^+ and p^+ electrodes. Neither set of columns penetrate through the whole sensor thickness yet. The columns are connected together by etching windows in the oxide layer and then coating the entire back surface with metal. Thanks to this technique it has been possible to accumulate enough experience to reach the full 3D passing throughout columns and to better understand the behavior of the charge collection. In parallel, this configuration has been looked up with simulations studies [66]. The electric field is different from the previous prototypes and it really depends on the deepness of the columns and even more on the overlap between them. The final full 3D

---

[5] See Section 4.5.1.

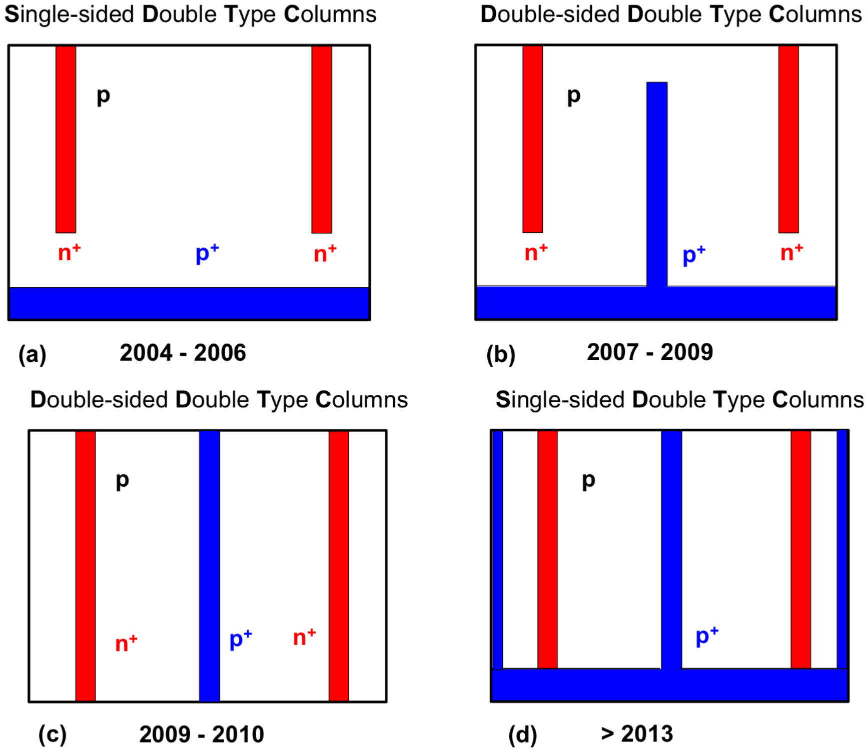

Figure 4.8: Sketch of the main steps of the 3D-FBK different architectures during the years. From the top left: (a) Single-side Single Type Columns, (b) Double-side Double Type Columns, (c) Full 3D Double-side Double Type Columns technique, (d) same as (b) with column edges. As in Figure 4.1, the blue lines represent the readouts while the red ones the ohmic electrodes.

passing, showed in Figure 4.8 (c), has been ultimate in December 2010 with the so called ATLAS07 production batch version[6]. The later improved version (ATLAS08) was bounded not to the FE-I4, newest version of Front-End, but to the existing old FE-I3. Finally, the ATLAS09 prototype, showed increased and yield in March 2011. Here the main differences between the various batches starting from ATLAS07, the first one to have the passing through columns:

ATLAS07 : layout compatible with FE-I4. Due to some processing problems (due to some mechanical stress the wafers sides were inclined), the currents were high with respect to the expected values. Moreover the p-spray dose was too high, causing a low breakdown voltage (around 30-35 V) with slim-edge (p^+ columns at the border).

ATLAS08 : layout compatible with FE-I3. Processing problems solved, but the p-spray dose were still too high. No active edge or slim-edge were present.

ATLAS09 : pre-production batch (or qualification batch). Layout compatible with FE-I4, basically similar to the ATLAS07, with the correct dose of p-

---

[6] Code used by the FBK farm to name the production batches. ATLAS07 or 3D-DTC-4 batch as reported in [66].

spray (breakdown above 45-50 V). Sensor thickness equal to 230 μm with slim-edge. IBL specification respected.

ATLAS10, ATLAS11 : identical layout of ATLAS09. Production batches on the way to be complete at the time of writing of these thesis.

In Chapter 5 the laboratory characterization of the ATLAS09 batch will be described in details. As Figure 4.8 (d) shows, the planned layout was thought to be a full-3D (for both type of columns) with active edge. To achieve this original plan, it was necessary to change the type of processing: from a double side to a one side processing, since it became necessary the support-wafer to have access to the back side. This is now changed to a simpler preliminary layout without active-edge still under development[7].

4.3.1 3D-Double Side Double Type Column

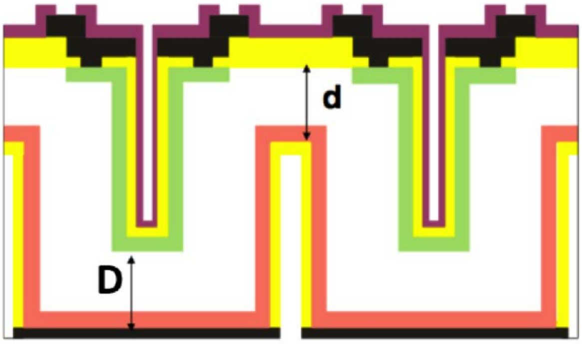

Figure 4.9: Schematic cross-section of a 3D-DDTC detector used with the FE-I3 (not in scale).

Based on the experience gained with 3D-STC detectors [16] as shown in Figure 4.4 (b), FBK has developed the 3D-DDTC detectors, which are aimed to have an enhancement performance while maintaining a reasonably simple fabrication process. The first 3D-DTC batch was completed at FBK at the end of 2007 [67] and it was based on a n-type substrate. A second wafer layout was designed and fabricated on high resistivity p-type substrate. The two were called 3D-DTC-1 and 3D-DTC-2 respectively. The main aim was to experimentally validate the 3D-DDTC approach and better understand the features of these technologies as intermediate steps to achieve the full 3D architecture, see Section 4.3.2. The main steps of the processing are summarized here and are summarized to Figure 4.10:

(a) *first DRIE*: a thick oxide is grown on both side of the wafer surface, to be used as masking layer for the DRIE step on the back side. The oxide is patterned on the back side and the first DRIE step is performed.

---

[7] Note that the distance between the last n^+ column to the active-edge it should be around 25 μm, see Figure 4.8 (d).

(b) *n^+ doping*: the thick oxide layer is removed from the back side and Phosphorus is diffused from a solid source into columns and at the back surface to obtain a good ohmic contact. A thin oxide layer is later grown to avoid out-diffusion of the dopant.

(c) *second DRIE*: the oxide layer on the front side is patterned and the second DRIE step is performed for the column etching.

(d) *p^+ doping*: the thick oxide layer on the front side is removed from a ring shaped region surrounding holes; Boron is diffused from a solid sure into the columns and at the open surface region to ease contact formation.

(e) *aluminum deposition*: an oxide layer is grown at the surface and in the columns to prevent the dopant out-diffusion; an additional oxide layer (TEOS[8]) is deposited; then contact holes are defined and etched through the oxide at the surface aluminum is suited and patterned.

(f) *second contact deposition and passivation*: the final passivation layer is deposited on the Front-End side, whereas on the back side, after removal of the oxide layer, aluminum sputtering provides a uniform metal electrode. Finally the passivation layer on the front side is patterned to define the access regions to the metal layer.

The p-type substrates are more appealing for the ATLAS Pixel upgrade: in p-type substrates the main junction remains always on the same side (after irradiation the so-called type-inversion does not occur, see Chapter 1, Section 1.8.1) and read-out electrodes collect electrons which are faster than holes and have a lower trapping probability [68]. However, the first 3D-DDTC detectors were fabricated on n-type substrates due to a delay in the wafer procurement [16]. It should be stressed that at the time of starting the detector fabrication, the DRIE equipment was not available at FBK, so that column etching had to be performed at an external service like IBS (France). Consequently, the sensor thickness of these first batch of devices was the standard 300 μm on n-type wafers (see Chapter 1 Section 1.5), which also allows a simpler technology since on the surface no isolation p-stop or p-spray implantation was necessary.

Differently from 3D-STC there are two type of columns that stop at certain distance d and D, as Figure 4.10 shows. Since the electrodes are etched from different sides, this approach has the advantage to *(i)* not use a wafer support and make possible to avoid two processing steps: the wafer bonding at the beginning of the entire process, and the mechanical lapping at the end of the process. *(ii)* after the first DRIE step is not required to grow an oxide layer thanks to the fact of not having two DRIE steps on the front wafer side. *(iii)* the electrode columns are empty and no filling and deposition steps are required.

Different layout versions of 3D-DDTC FBK sensors bump-bonded to the FE-I3 version have been studied, featuring two (2E), three (3E) 105 and four (4E) equally spaced electrodes per pixel (see Figure 4.3).

---

[8] TetraEthOxySilane - Gas used as a source of silicon for the deposition of silicon dioxide (SiO_2).

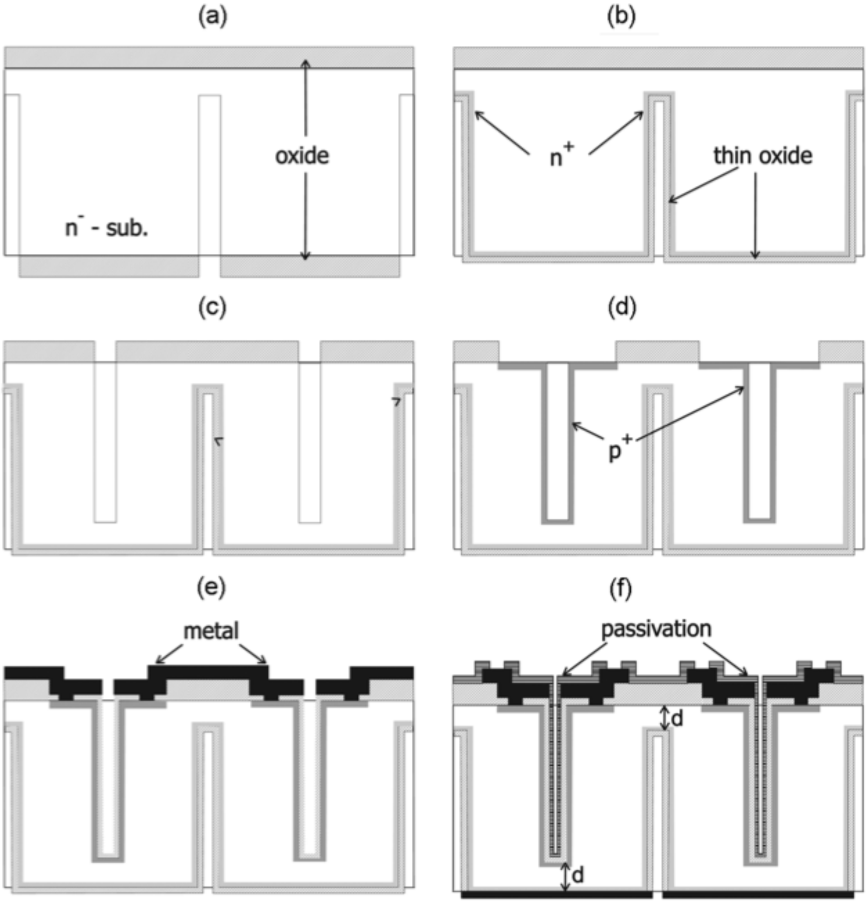

Figure 4.10: Main steps of the 3D-DDTC fabrication process on the n-type substrate [67]. (a) first DRIE, (b) n^+ dipping, (c) second DRIE, (d) p^+ doping, (e) aluminum deposit and final (f) second aluminum deposition contact and final passivation.

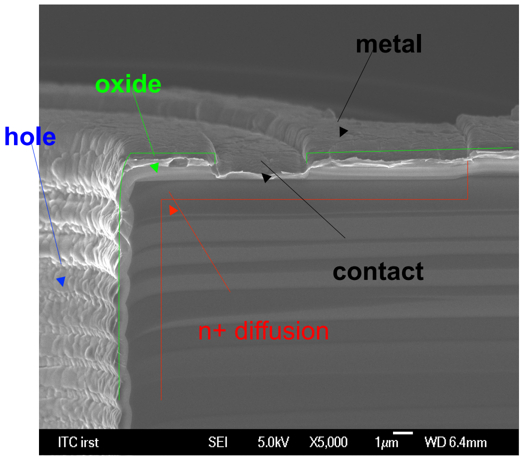

Figure 4.11: 3D-FBK electrode layout [10].

4.3.2 3D-DDTC: The Full-3D

As reported in several studies and published results such [67] or [66], the efficiency of the DDTC technology is strongly related and critically depending on the columnar electrode overlap as well as on the radiation hardness. Indeed, the overlap region between columns is the depletion region where the sensor collects the charge, see Section 1.3. The electric field is higher between the columns respect to the regions below the electrodes. Therefore, to a deepest depletion region corresponds to a better efficiency.

The goal to reach a passing through columns is not easy to reach. In fact, ideally the distance between the column tips and the opposite surface should be at the worst case just few tens (20-30) of μm. This hypothetic restriction affects both depth columns, ohmic and junction, in a way that depends on the substrate thickness. This is not so easy to obtain even with a well controlled and reproducible processing since the column depth attainable with a DRIE process is strongly dependent on the column diameter, and even small variations of it, as achieved with standard lithography equipment (mask aligner), can results in differences between column depths of several μm. The parameter used to define the ratio between the diameter and the depth of the column electrode is called aspect ratio[9]. Moreover, an additional problem appears during etching holes on both sides of the wafer. Since every wafer is different from the other, the non uniformity on the wafer thickness might be an issue. The thickness has to be well measured in order to minimize the risk to break the wafer and to optimize the DRIE etching time for each wafer. As confirmed, in some FBK 3D-DDTC were observed non uniformities in the same wafer batch ATLAS07 (as previously anticipated, more informations in [66]), and consequently a different column depth values of the order of few μm were measured[10].

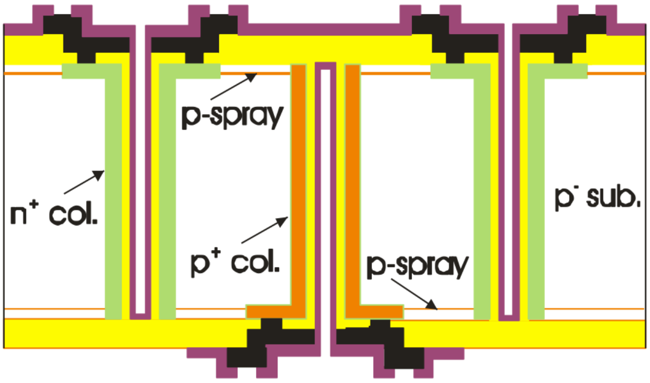

Figure 4.12: Schematic cross-section of a modified 3D-DDTC detector with passing through columns (not in scale) [66].

Like in the previous versions of the 3D-DDTC detectors, no polysilicon material is used to fill the columns. The read-out columns are n^+-type doped on a p-type substrate, with p^+-type columns as ohmic columns. The columns are

---

[9] Which was 11:1 in 1997, 24:1 in 2009 and nowadays reaches the value of 110:1 [69]

[10] To avoid this unintended effect FBK developed an enhanced 3D-DDTC$^+$.

doped by thermal diffusion and then passivated by silicon oxide. The p-spray technique is used to ensure the required surface isolation between junction columns on both wafer sides. Once again, no support wafer is required as for the previous 3D-DDTC version, therefore the advantage to avoid the related wafer bonding and final etching steps is possible which make easier the fabrication process. An additional advantage is that the wafer back side is fully accessible, so that it is possible to increase the design flexibility. Therefore, like in the Pixel detector assemblies such as the ATLAS Pixel Detector, the read-out is connected to the front surface of the 3D detector, through bomb-bonding (see Section 1.7), while the required power supply is provided by the back-side of the sensors because is shorted. This is an important option for space-constrained applications, like the ATLAS Insertable B-Layer.

As already explained in Section 4.2.2, the active edge is one of the main features of the 3D sensors. For the 3D-FBK sensors, due to the absence of the wafer support, the 'real' active edge technology[11] is not implementable. On the contrary, the DDTC technology is suitable to allow "slim edges". Slim edge technology consist of a multiple ohmic columns (p^+ electrodes) termination having an overall size of the order of 200 μm. Figure 4.13 shows a detail of the ATLAS09 pixel sensor prototype (front-side) for a FE-I4. This technology has the feature to have a dead area of only 200 μm at the edge (between the cut-line to the pixel cels) and on the other side of order of 400 μm. The p^+ columns fence outside the 'active' pixel region are aimed to "limit" the electric field to prevent the depletion region spreading from the outermost junction columns to reach the cut-lie. Thanks to this technique the detector can be safely operated even at high voltages, since no leakage current contribution from the highly damaged cut-line influence the detector itself. Moreover, it seems that such technique is more sensible with respect to the planar case and the CNM case (it will be explained in Section 4.4). Recently more detailed studies have shown that this dead area could be reduced to 100-150 μm without detecting the detector[12] performance [70], [45].

To test the quality of each batch, on the wafer it is provided a temporary metal line which connects 336 pixels into a strip. This method have been developed at FBK[13] and allows a good IV tests to estimate the quality of the sensors detecting the presence of defects. 80 strips line, which are on the respective 80 columns of the FE-I4 chip (after bump-bonding) short together a full column of the pixel. The strip line terminates to a probing pad located outside the active region of the sensor, to avoid any possible surface damaging. Therefore, all the columns are measured separately and summer up together, and after the measurement these temporary metal layers are removed. Such a measurement will be reported in the Section 4.5.1 (see Figure 4.18).

---

[11] Active edges on the four sides of the wafer.

[12] Especially the breakdown voltage of the detector.

[13] Together with STINTEF and Stanford.

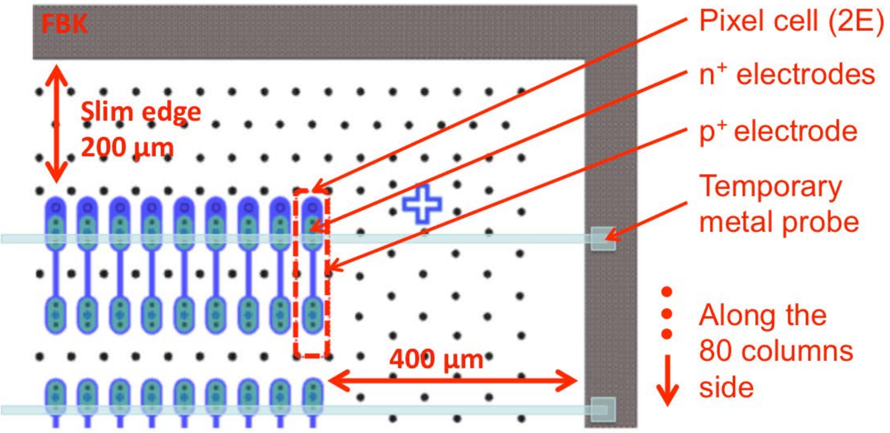

Figure 4.13: Detail of the 3D FBK production mask design [35]. Temporary metal strip are used to evaluate the electrical characteristic of the device before bump-bonding.

4.4 3D CNM sensors

The first layout included MEDIPIX2[14] pixel detectors and microstrip sensors suitable to be read out with the LHCb chip [16]; capacitance measurements have shown a lateral depletion on only 2V and a total depletion of 9V [72]. Functional characterization with the MEDIPIX2 chip has shown a reduced charge sharing with respect to planar sensors, thanks to the 3D electrode configuration [73]. A microstrip detector has been irradiated up to 5×10^{15} $\mathrm{n}_{eq}/\mathrm{cm}^2$, and at a bias of 200 V the chip has recorded a most probable charge of 12800 electrons from a MIP particle, comparable with the results obtained by the Stanford group [74]. The first detector fabricated in the clean room facilities of CNM-IMB [62] in Barcelona was presented in [59] in 2007. The proposed [75] alternative double-sided 3D detectors were fabricated in a double sided configuration, with columns of one doping type etched from the front side of the device and the other type etched from the backside, like for the FBK-DDTC. As shown in Figure 4.14 neither set of columns passed through the full thickness of the silicon substrate and they were 250 μm deep on a 300 μm thick substrate.

For the layout shown in Figure 4.14, the main limitation to reach a full 3D detector was the aspect ratio of the plasma etching process. To allow an electrode overlap depth of 200 μm, a diameter of 10 μm was necessary. On the contrary, the diameter should be kept s small as possible since otherwise it presents lower efficiency, as described in [40] and later on in [76]. By simply enlarging the hole diameter or using thinner detectors it is possible to get a standard 3D detector. The double side structure is similar to the the one of a full 3D, but it has a simpler fabrication process since the difficulty of doping the two different kind of holes on the same side is avoided. The 3D fabricated at CNM consist of a very thick

---

[14] a Medipix2 collaboration was started at the end of the 1990' with the aim of taking advantage of the potential of deep sub-micron CMOS to shrink the pixel size and to increase the number of pixels per chip. The outcome of that effort is the Medipix2 chip [71].

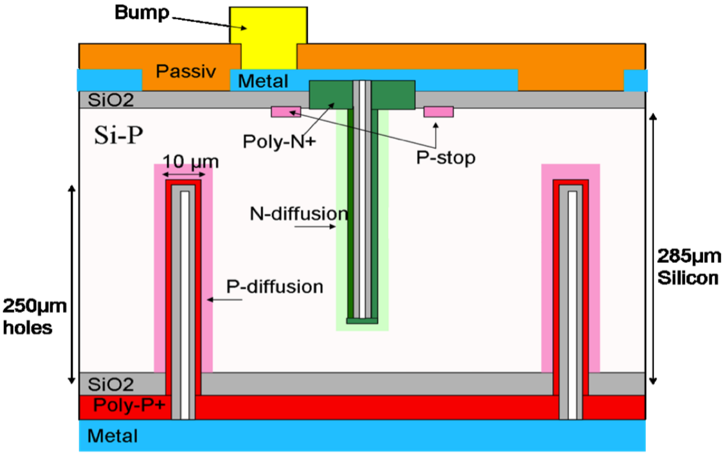

Figure 4.14: Layout proposed for the double sided 3D-CNM detectors [74].

layer of polysilicon deposited on the two sides of the substrate. The polysilicon is highly doped in order to create the p-n junctions. The p and n diffusion is therefore naturally created since the substrate is less doped, and of p type. The electrodes are not filled but a layer of SiO_2 is needed to create the isolation: the read out columns are partially filled with poly-p^+ while the ohmic columns poly-n^+, see Figure 4.14. As for the 3D-FBK DDTC, the ohmic columns are on the backside of the wafer and are shorted together to apply the high voltages bias to the back surface of the detector creating the advantage to power supply the sensor with a simple wire bonding. This avoid complicated rerouting in detectors for the read out electronics. Consequently, the photolithographic steps define the electrode contacts in the polysilicon layer only on the top surface: no special patterning is required to connect the electrodes to the metal plate. Two sections p-doped are implanted on the Si-substrate to have p-stop implants and a higher break down voltage.

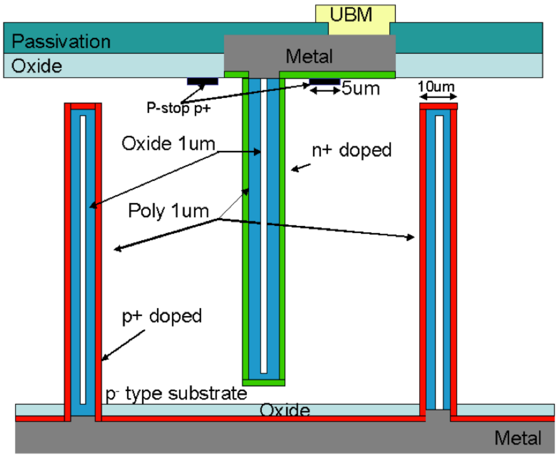

Figure 4.15: Layout proposed for the double sided 3D detector with the columns that do not penetrate the full thickness of the sensor [35].

As for the FBK case also, for the 3D-DDTC$^+$ technology no active edge is

Parameter	**Value**	
	3D CNM double sided*	3D CNM (full 3D)
Substrate (p-type) thickness	300 μm thick bulk	230 μm electrodes
Junction column (n^+) thickness	250 μm	210 - μm
Ohmic column (p^+) thickness	250 - μm	210 - μm
Column overlap	90 - 100 μm	110 - 150 μm
	3D FBK double sided*	3D FBK (full 3D)
Junction column (n^+) thickness	100 - 110 μm	140 - 170 μm
Ohmic column (p^+) thickness	180 - 190 μm	180 - 190 μm
Column overlap	90 - 100 μm	110 - 150 μm

Table 4.2: 3D-CNM detectors. [*] Indicates the presents of the FE-I3

implemented but a slim edge of 200 μm. As shown in Figure 4.16, a CNM sensor has a 200 μm inactive area in the edge region. For the CNM sensors, with difference to the 3D-FBKs DDTC, the edge isolation is guaranteed with a combination of a n^+ 3D guard ring, which is grounded, and fences, which are at the bias voltage potential from the ohmic side. The sensor quality of the wafer, before dicing, is evaluated on the 3D guard ring, see Section 4.5.1. Some results have been reported in [48] and [35].

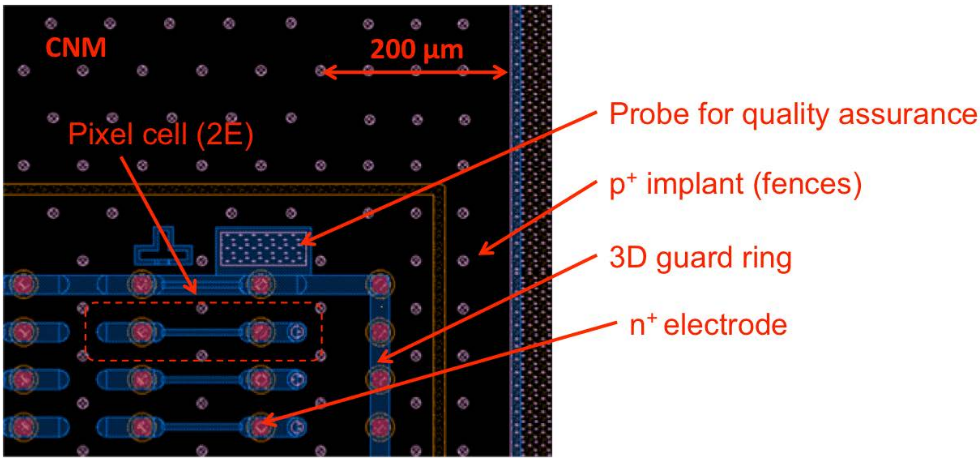

Figure 4.16: Detail of the 3D CNM production masks design [35]. Temporary metal strip are used to evaluate the electrical characteristic of the device before bump-bonding.

4.5 IBL 3D Sensors

3D silicon sensors are manufactured on a standard 4” FZ p-type [77]. For the IBL project the option without wafer support has been preferred and chosen to keep the processing more reliable, since all the technological steps where, to this case, well established[15]. The remaining processing steps after electrodes etching

---

[15] The typically number of masks requested for the 3D process are between 12 (for the FBK) and 10 (for CNM). If once counts the entire subprocess needed could be above 150.

are identical to a planar silicon sensor: bump-bonding to the readout. Handling is also the same. In order to reduce the complexity of the development and increase the limited production capability of such a new technology from a single manufactures, four 3D processing facilities granted to combine their expertise for the production of the required volume of 450 (plus spares) sensors compatible to the IBL Front-End chip FE-I4. But, at the end, among all the several production facilities, only two of them have been selected for the IBL. Based on their established expertise in manufacturing 3D sensors with no wafer support, the Centro Nacional the Microelectronica (CNM-CSIC, Barcelona Spain [62]) and the FBK, Trento Italy [63] were selected.

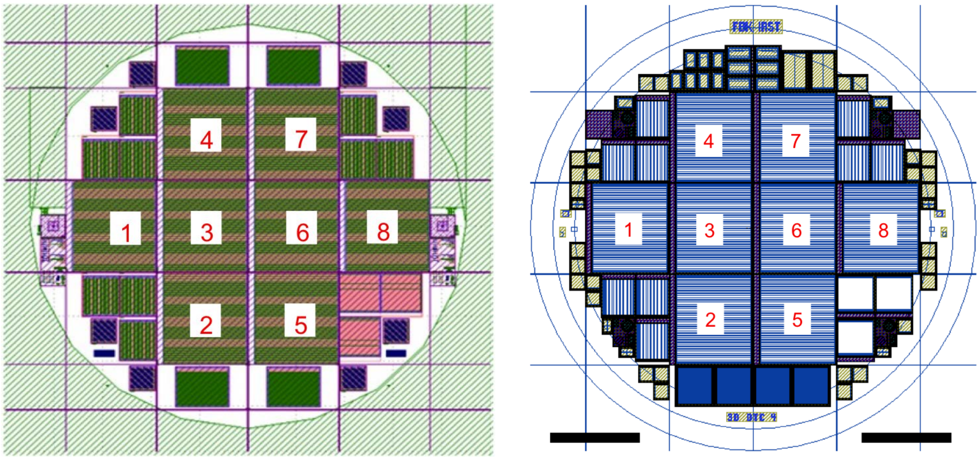

Figure 4.17: Common 3D wafer layout: schematic of a processed wafer (a) CNM (Barcelona), (b) FBK (Trento) [48]. The numbers in red represent the eight 3D sensor which will be bump-bonded with FE-4 for the IBL project.

The CNM and FBK decided to create a similar wafer layout, shown in Figure 4.17, basically with the same core (central part of the wafer layout), and with small differences around it. In fact, it contains: eight FE-I4 single chip tiles numbered from 1 to 8[16]; nine FE-I3 single chip sensors; three CMS pixel sensors.

It must be stressed that to monitor the technological parameters and to perform preliminary tests to the batch, just at the wafer periphery are present a number of test structures, which are different for CNM and FBK. The design specifications are common and are listed in Table 4.3.

As Figure 4.15 shows, the columns of the 3D-CNM do not completely penetrate the entire sensors thickness. They are 210 μm deep isolated on the read-out side (front side in the FBK sensors) with p-stop implants. Therefore, they terminate at 20 μm to the opposite side of the wafer. In addiction, the edge isolation is accomplished with a combination of a n$^+$ 3D guard ring which is grounded and fences which are at the bias voltage potential. No wafer sensor support is present (as already mentioned) and so the ohmic side - p$^+$ electrodes are shorted together and connected as well to the power supply. Both types of columns are in part

---

[16] The wafer layout for the 3D-FBK sensors has been renamed after ATLAS07 where the numbering was different: from the 1,2,3,4,5,6,7,8 of the ATLAS07 to the 4,7,1,2,3,6,8,2,5 of Figure 4.17 and the official document [77], to unify the CNM and FBK naming.

Tile type	single
Number of columns per 250 μm pixel	2
Sensor thickness	$230 \pm 20\ \mu m$
Columns overlap	$\geq 200\ \mu m$
Sensor active area	18860×20560 (+scribe line) μm^2
Dead region in Z	200 μm guard fence + ∼25μm cut (see Figure 4.13)
Wafer bow after processing	$< 60\ \mu$m
Front back alignment	$< 5\ \mu$m
Alignment marks	as specified for stave loading (see Figure 4.13)
Bias Voltage Pads	for the sensors specifications (see Figure 4.13)

Table 4.3: 3D design specifications with FE-I4 [77].

filled with polysilicon[17] which on the front side is used as metal contact. While for the 3D-FBK, the columns are complete empty, but a n$^+$-implantation is used to create the metal contact similarly to the p$^+$-columns. The columns are isolated on the front side, junction side, with the other technique of the p-spray technique. A 200 μm long ohmic fence isolates the pixel area from the edges: p$^+$ columns are etched between the last n$^+$-row of electrodes and the border, to reduce the electric field and "stop" the depletions region preventing the diffusion through the edge. Of course, these slight differences create advantages and disadvantages: for example FBK has a larger sensitive active area close to the edge, as presented in [78]. From simulations, it seems that this dead area can be possibly reduced reduce to 100 μm.

4.5.1 IBL 3D Sensor Specifications

Since each 3D sensor device has a different behavior and history, the 3D sensors community has defined a list of the electrical specifications required to qualify a device as properly functioning [77]. These specifications are reported in the following:

1. Operation at room temperature (20-24°C)
2. V_{depl}[18] $\leq 15\ V$
3. $V_{op} \geq V_{depl} + 10V$ where V_{depl} is the full depletion voltage.
4. Current at 20 - 24° C at operation voltage: $I\ (V_{op})\ < 2\mu A$ per tile
5. For guard-ring (GR) measurement (CNM) bump-bonding: $I_{GR}\ (V_{op})\ l < 200\,nA$ per tile
6. Breakdown voltage: $V_{bd} > 25V$
7. Slope: $[I(V_{op})/I(V_{op} - 5V)] < 2$

---

[17] The center part of the columns is empty.

[18] with *depl* = full depletion, *op* = operational and *bd* = breakdown voltage

Each listed specification above refers to an IV measurement performed directly on the wafer on each tile detector at the wafer scale (with a probe station by the manufacturer): either by using a removable temporary metal or by probing the guard-fence current. The first parameter, the room temperature (around 20° C), specify the environmental conditions to operate and test the devices in the laboratory. An upper voltage threshold of 15 V indicate the maximum voltage when 3D sensors are fully depleted. An operational voltage defined as $\mathrm{V}_{depl} + 10V$ identifies the power supply be applied to the 3D sensors. A value of ten volts higher then the depletion voltage was considering enough to operate the detector, while the current measurement at the operational voltage (at room temperature) should be below 2 μA per tile (Figure 4.18 shows an example of the measurement done by the FBK). On the contrary a current below 200 nA per tile is required. The breakdown voltage is different for each batch but a lower threshold of 25 V is required to define a 3D as a good sensor. The last parameter is related to the slope of the IV (current vs voltage) measurement (at the operational point and at 5 V less) which has to be less than 2.

A well defined list of sensor selection criteria [77] has been prepared and it will be applied to each sensor.

After some years of working, the 3D sensors will have accumulate a certain dose of radiations. In particular, as already mentioned in Chapter 3, Section 3.4, the IBL layer expected to withstand a non ionising fluence of 5×10^{15} $\mathrm{n}_{eq}/\mathrm{cm}^2$. Therefore, several 3D samples have been irradiated to the above fluence and have been studied afterwards. The following specifications and performances should be expected [77]:

1. Operation at -15°C
2. $V_{operation} \leq 180\ V$
3. Power dissipation $\leq 0.06\ Wcm^{-2}$
4. Tracking efficiency at 15° angle $> 97\%$

Where points (1) and (4) come from the IBL sensors specifications. The 3D sensor has to be operated at -15° C, with a power supply below 180 V due to the irradiation damage. The power dissipation has been estimated to be less than 0.06 Wcm^{-2} and the tracking efficiency at tilted angle of 15° above 97%.

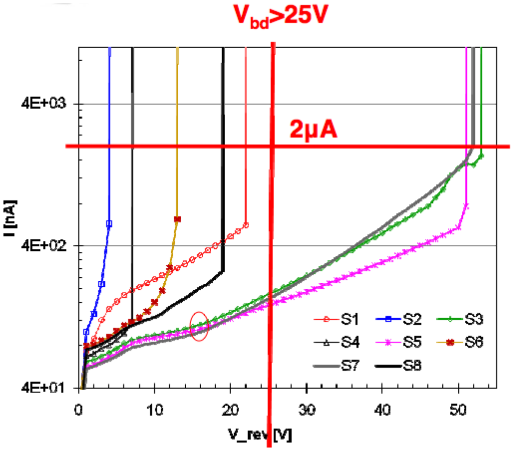

Figure 4.18: Example of IV measurement on the temporary metal directly on the wafer. Sensors 3, 5, 7 satisfy the IBL 3D specifications, while sensors 1, 2, 4, 6, 8 do not satisfy the specifications. Measurement done in Trento by the FBK [48].

4.6 Devices Under Test

In Table 4.4 are listed all the sensors (Devices Under Test) that will be described, tested and characterized in the next chapters. All of them belong to the so called ATLAS09 wafer batch, the batch used to test and characterized the full-3D FBK made in Trento for the IBL project. The sensors design is a 3D-DDTC n-in-p meaning that the read out columns are n^+ doped in a p^+ substrate. The substrate thickness is 230 μm. Moreover, after laboratory characterization, two samples, FK09 and FBK11 were sent to proton irradiation to Karlsruhe in Germany, in May 2011 [79] . In order to study the radiation tolerance of these sensors design they were irradiated with different target fluences with 25 MeV proton beam: respectively up to 2×10^{15} and 5×10^{15} n_{eq}/cm^2. Using the NIEL hypothesis [12], with hardness factors of 1.85, 0.62 and 0.88 for 25 MeV protons, 24 GeV protons, and reactor neutrons, respectively. The uncertainty in the irradiation fluences is lower than 10%. After irradiation, the two detectors were sent back to CERN for a 2 hours annealing at 60° C, and cooled to prevent further annealing, even if for short time, during handling and preparations for measurement setup.

The sensor named GE_CNM4_101, is a 3D-CNM sensor made by CNM in Barcelona, which will be used to compare the charge collected with a respect to a non-irradiated FBK, see Section 5.5.3.

SCC is the Single Chip Card, and it is the board where the sensor is mounted to test it and to read out the data through the Front-End. A defined SCC number corresponds to a defined sensors and Front-End (more details are explained in next Chapter 5).

Sensor	Type	Wafer Batch	Wafer Thickness	Design	SCC	Fluence Irr. [n_{eq}/cm^2]
GE_FBK09	3D FBK n-in-p	ATLAS-09	230 μm	DDTC	90	2×10^{15}
GE_FBK11	3D FBK n-in-p	ATLAS-09	230 μm	DDTC	87	5×10^{15}
GE_FBK12	3D FBK n-in-p	ATLAS-09	230 μm	DDTC	104	
GE_FBK13	3D FBK n-in-p	ATLAS-09	230 μm	DDTC	105	
GE_CNM4_101	3D CNM n-in-p	2011_090	230 μm	DDTC	101	

Table 4.4: Devices Under Test.

Chapter 5

Laboratory Measurements

5.1 Introduction

The characterization of the 3D devices has been shared between three different laboratories: FBK (Trento), Genova and CERN. Most of the work has been done in Genova inside the INFN clean room, except for the first IV measurements on the wafers, which has been done directly inside the FBK facility.

Before studying the behavior of the 3D-FBK sensors at the beam test performed at the CERN SPS experimental area, as explained in Chapter 6, all 3D samples were studied in the laboratory of Genova (only very few of them were tested in Bonn) to make the tuning and the proper characterization of the Front-End and of the sensor design. In the following Chapter, the sensor characterization which I have been doing in the Genova clean room is described. I have done all the measurements reported, including the preparation of the setup. In addition, I have performed also the data analysis.

5.2 Laboratory Characterization in Genova

Tests were performed in a clean room (see Figure 5.1) where the devices were wire bonded to the Bonn motherboard with a proper machine. For each sensor, the wires have been checked with a microscope, to control the quality of their connections. After this first step, the USBpix system, (see Section 5.3.1) was used to check that the analog and digital circuits were not shortened.

The modules were identified by the number of the Single Chip Card (SCC[1], see Figure 5.2) on which they were mounted. This consists of a PCB board with one single sensor mounted onto it, matched to one FE-I4 read-out chip.

The detectors have been characterized via the following measurements[2] (Table 5.1):

1. Leakage Currents
2. V_{cal}

---

[1] http://icwiki.physik.uni-bonn.de/twiki/bin/view/Systems/USBpixTables

[2] https://twiki.cern.ch/twiki/bin/viewauth/Atlas/PixelUpgrade3DSystematicStudies

3. Analog & Digital Test
4. Tuning
5. Threshold and Noise vs HV
6. Noise Occupancy Scan vs HV
7. Response to γ and β radioactive sources (Am^{241}, Sr^{90})

Name	**SCC**	**IV**	**Irradiation**	**Beam**
GE_FBK4_3D_09	90	Genoa	$2\ 10^{15*}\ n_{eq}/cm^2$	CERN
GE_FBK4_3D_10	88	Genoa	-	-
GE_FBK4_3D_11	87	Genoa	$5\ 10^{15*}\ n_{eq}/cm^2$	CERN
GE_FBK4_3D_12	104	Genoa	-	-
GE_FBK4_3D_13	105	Genoa	-	CERN
GE_FBK4_3D_14	103	Genoa	-	-
BON_FBK4_3D_04	107	Bonn	-	-
BON_FBK4_3D_05	108	Bonn	-	-
BON_FBK4_3D_06	109	Bonn	-	-
BON_FBK4_3D_07	59	Genoa	-	-
BON_FBK4_3D_08	62	Bonn	-	-
BON_FBK4_3D_09	110	Bonn	-	-
BON_FBK4_3D_10	111	Genoa	-	-
BON_FBK4_3D_11	112	Genoa	-	-
BON_FBK4_3D_12	113	Genoa	-	-
BON_FBK4_3D_13	114	Genoa	-	-

Table 5.1: Code name for all the 3D-FBK detectors for the batch ATLAS09, for which the IV measurement was done, and the beam tests were performed.
* Irradiated with protons in Karlsruhe (Germany).

Tests have been performed at room temperature (20 - 25° C) for the unirradiated devices, and also inside a Binder climate chamber[3], showed in Figure 5.1), in order to reach low and high temperatures keeping the humidity under control. The climate chamber covers the temperature range between -40° C and 180° C for heat and refrigeration tests. To run all the measurements previously listed an experimental hardware setup and a dedicated software have been developed.

For all these measurements, with the exception of the V_{cal} one, a bias voltage had to be applied to the detector, and the module itself (sensor and SCC) had to be kept in the dark. Since the presence of light increases the measured current (light is made by photons which cross the sensor and leave a signal), it is necessary to remove it to not modify the measurement results. For this scope, a simple black cloth or an additional cardboard was used to cover the whole SCC.

---

[3] Binder MK 53 series

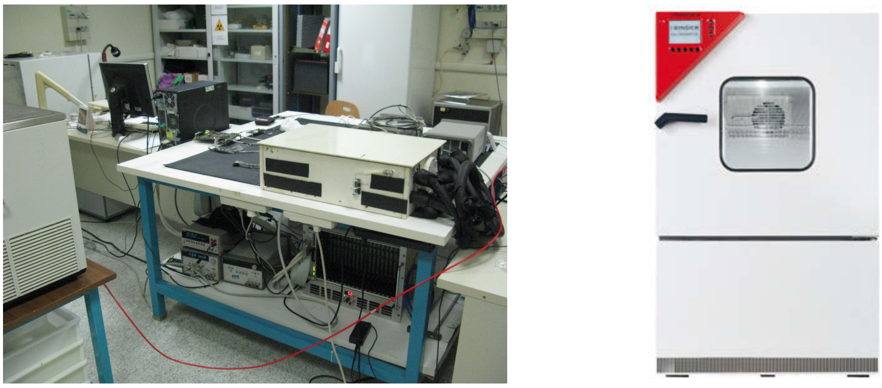

Figure 5.1: INFN Clean Room Laboratory in Genova (on the right), and climate Chamber Binder (on the left).

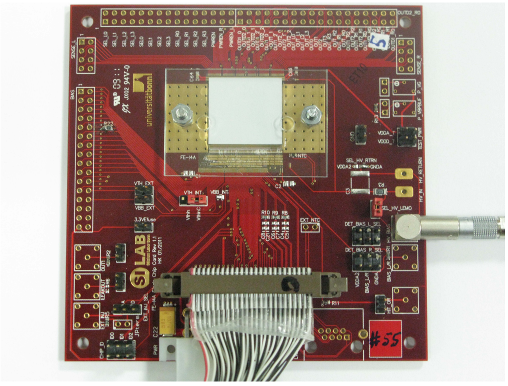

Figure 5.2: SCC board with the FE-I4 and a 3D-FBK sensor wire bonded on it.

5.3 Laboratory Setup

5.3.1 USBpix and FE-I4 adapter card Setup

The experimental setup used for all the detector tests and characterizations is the USBpix system [80]. The USB, based on the previous FE-I3[4] readout system was developed as an alternative to the common 'TurboDAQ'[5] (TPLL, TPCC) system by the SiLab [81]. Compared to the previous TurboDAQ test system it uses a very low level hardware components. The system has been designed to have a modular structure, and to serve the FE-I3 and the FE-I4 new systems. The USBpix hardware is based on a multipurpose IO-board (S3MultiIO) with a USB2.0 interface to a PC and an adapter card which connects the S3MultiIO to the Single Chip Adapter Card (SCC) where the FE and the sensor are mounted. The S3MultiIO system contains a programmable (Xilinx XC3S1000 FG320 4C) Field Programmable Gate Array (FPGA), which provides and handles all signals going to the FE; a microcontroller with a USB2.0 interface which establishes the data transfer to a PC is used as a high-speed device conform to the USB2.0 specifications. This controller provides various interfaces: high speed interface

---

[4] First chip readout system, actually present in Pixel Detector.

[5] Used mostly during the ATLAS Pixel production phase.

(8/16 bit fast data bus to the FPGA) interface to the μC core (8 bit data, 16 bit address) port bits, SPI serial interface, I2C serial interface; an asyncronous Static Random Access Memory (SRAM) to extend the internal FPGA memory capabiltiy with 16Mbit SRAM, a programmable clock generator which provide a clock signal from 80 kHz to 150 MHz attached to the FPGA. In addition there are an EEPROM[6] U3 (16kbyte) to store the microcontroller firmware and several LEMO connectors as well as one Ethernet connector. The card itself needs to be powered with 5 V and it can be configured to operate either as a bus-powered (USB) or a self-powered device (through a connector mounted on the main board). Onboard are present DC/DC converters to provide 3.3 V, 2.5 V, and the FPGA core voltage of 1.2 V, see [82] for more details. The Input-Output connections of the S3 Multi IO System are listed below:

- USB2.0 B-type as host interface
- Multi-IO-Connector with 80 user IO's (Vcc IO 1.2 V to 3.3 V)
- Agilent debug connector (1253-3620)
- JTAG[7] connection
- RJ-45 connector for 2 LVDS transmitter and 2 LVDS receiver
- Header with I^2C and SPI functionality
- Header with additional FPGA user IO's
- 3 buffered LVTTL outputs with LEMO
- 3 buffered LVTTL inputs with LEMO

The power supply is provided thanks to an external 5 V supply or via USB cable. The configuration capability is realized through JTAG or via USB2.0.

The USBpix provides the possibility to have as input an external generated Level1 triggers[8] to satisfy the beam test requests. The external triggers can be brought to the board using the LEMO connector RX0 or the Ethernet connector, which makes USBpix compatible to the EUDET telescope, described in Chapter 6. The external signal is synchronized, stretched and delayed in the logic generating internal Level1 triggers. It is also possible to use an internal self-trigger as the positive edge of the Hitbus by simply connecting the LEMO connector TX1 to the RX0. This case is useful and used for sources test, when every hit should be read, like for the Am^{241} source scan (see Section 5.5.3). The multi I-O board communicates with the FE adapter card via a 84 pins connector. The adapter card contains some support logic and also bias voltage regulators for the

---

[6] Electrically Erasable Programmable Read-Out Memory.

[7] Join Test Action Group.

[8] The ATLAS trigger and data-acquisition system is based on three levels of online event selection. Each trigger level refines the decisions made at the previous level and, where necessary, applies additional selection criteria. Level1 (LVL1) trigger makes an initial selection based on reduced-granularity information from a subset of detectors. See [83] for more details.

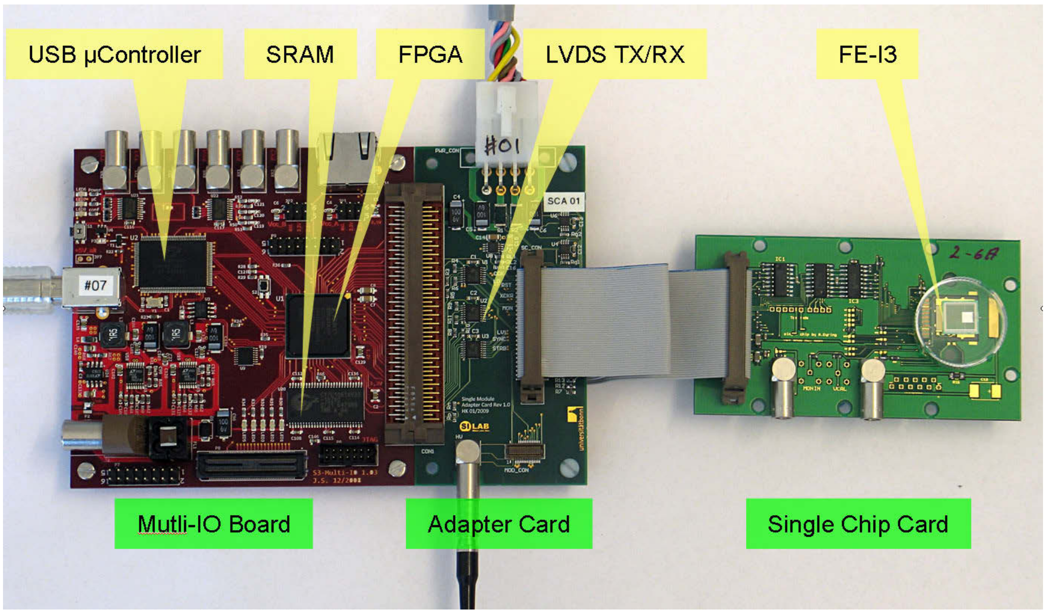

Figure 5.3: USBpix system for the FE-I3 single chip readout.

Front-End. The two analog and digital voltage supplies, respectively VDDA and VDD, with 2 V can be set via software on the PC. Commands, data and low bias voltages are sent via a flat cable from the adapted card to the single chip card in order to supply power to the Front-End (FE-I4).
The main hardware components are listed below:

- USBpix
- FE-I4 adapter card
- SCC board with the sensor
- Agilent E3634A 200W Power Supply, 25V, 7A or 50V, 4A: to provide the analog and digital power supply to the FE-I4
- Keithley 2400-LV Source Meter w/Measurements: to power supply the sensor through a Lemo connector cable to an SCC board
- PC equipped with Windows XP / Windows 7, 32-bit with Microsoft Visual Studio (Express) 2008[9]
- Climate Chamber to set the operational temperature.

The tuning and the data read out is done by a software application called STControl.

---

[9] For more specifications details see USBpix software section on:
$http : //icwiki.physik.uni - bonn.de/twiki/bin/view/Systems/UsbPix\#USBpix_software$

5.3.2 Software

The user interface to communicate easily the USBpix system is the STControl, whose control panel is shown in Figure 5.4. Thanks to it, one can configure the Front End and therefore operate with the system. It uses ROOT [84], a framework for data analysis, and QT[10] to implement a graphical user interface and it is based on the ATLAS PixLib package. It collects C^{++} classes originally developed to provide access to the ATLAS Pixel detector. The hardware specifics of this package have been adapted to access the FE pixel chips via the USB/FPGA card.

To perform a measurements[11], a particular configuration must be used which contains all the settings needed for the Frond-End. A standard configuration can be used to start, as shown in Figure 5.5. The C_{high} and C_{low} there are default parameters which belong to the Front-End pixel module and in this thesis are assumed constants[12]. The only parameter measured in each devices is V$_{cal}$. V$_{cal}$ is measured to have an accurate value of the tuning, as described in Section 5.4.1.

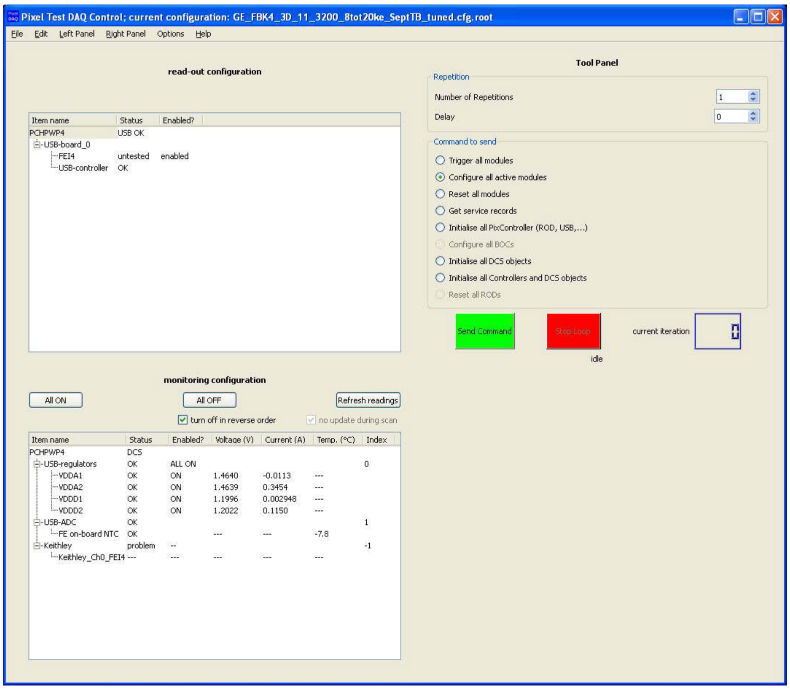

Item name	Status	Enabled?
PCHPWP4	USB OK	
USB-board_0		
FEI4	untested	enabled
USB-controller	OK	

Repetition

Number of Repetitions 1

Delay 0

Command to send

○ Trigger all modules
● Configure all active modules
○ Reset all modules
○ Get service records
○ Initialise all PixController (ROD, USB,...)
○ Configure all BOCs
○ Initialise all DCS objects
○ Initialise all Controllers and DCS objects
○ Reset all RODs

☑ turn off in reverse order ☑ no update during scan

Item name	Status	Enabled?	Voltage (V)	Current (A)	Temp. (°C)	Index
PCHPWP4	DCS					
USB-regulators	OK	ALL ON				0
VDDA1	OK	ON	1.4640	-0.0113	---	
VDDA2	OK	ON	1.4639	0.3454	---	
VDDD1	OK	ON	1.1996	0.002948	---	
VDDD2	OK	ON	1.2022	0.1150	---	
USB-ADC	OK					1
FE on-board NTC	OK		---	---	-7.8	
Keithley	problem	--				-1
Keithley_Ch0_FEI4	---	---	---	---	---	

Figure 5.4: STControl panel which configures and controls the Front-End of the sensors. The panel shows the configuration of the FBK11 tuned at 3200 e$^-$ at eight TOT for 20 ke$^-$ used during a laboratory measurement before the September Test Beam.

---

[10] QT is a cross-platform application framework that is used for developing application software with a graphical user interface (GUI), and also for developing non-GUI programs such as command-line tools and consoles for servers.

[11] The IV scan can be done without using the STControl software package.

[12] An interesting study could be to measure the capacitances before and after irradiation.

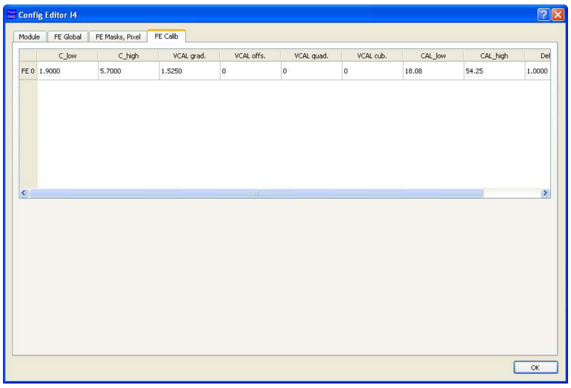

	C_low	C_high	VCAL grad.	VCAL offs.	VCAL quad.	VCAL cub.	CAL_low	CAL_high	Del
FE 0	1.9000	5.7000	1.5250	0	0	0	18.08	54.25	1.0000

Figure 5.5: STControl FE Configuration window: the figure shows the main parameters setting for the Front-End such as C_{high} and C_{low} and V_{cal} *grad.*, see Section 5.4.1.

5.4 Front-End Calibration: Tests and Tuning

Calibration measurements and tuning of the Front-End are important for different needs, mainly coming from the operation side of the detector itself or the offline analysis. In fact, to have a safe and stable operation of the detector, it is necessary to determine the needed interventions or to apply new and more detailed calibrations. On top of that, the determination of the correct calibration constants for the offline analysis can guarantee a constantly high quality of the reconstructed data: to reach this goal is important to uniform all the read out electronics in order for them to operate, receive and compare data starting from the same settings. For a reliable operation of the detector itself or, in this case, of a 3D sensor, the electronic thresholds have to be set to an appropriate value and adjusted pixel by pixel. For this, two different types of measurements are needed: the threshold scan, which measures the starting threshold of each pixel, and the threshold tuning, which adjusts the threshold of each pixel as close as possible to a desired target value [85]. In this Section it will be given a short explanation of the test and the measurements necessary for the final tuning, which makes it possible to work properly with the Front-End. For this reason the V_{cal} measurement, the analog and digital tests, the threshold and TOT verifications will be the first ones to be discussed. Later on, the tuning phase of the Front-End to be set at the target values for further tests with the sensors will be added. Before running all these scans and, in general, during the tuning process at the first zero step, the phase between the data rate and the clock rate has to be adjusted. For this synchronization, a “8b10b” pattern is used, see [28] for more details. The adjustment can be done by running the *rx delay scan* in the STControl every time the Front-End is switched on. The aim of this scan is to evaluate the error rate of the received pattern versus the phase shift. A standard and expected output result is shown in Figure 5.6.

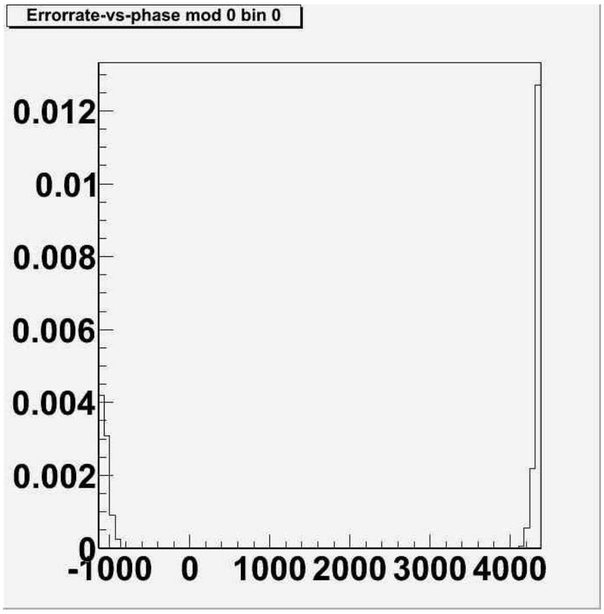

Figure 5.6: Example of rx delay scan output - FBK11.

5.4.1 V_{cal} measurement

As already wrote in Section 3.3.2, the Front-End has to be calibrated properly. To have a better and correct tuning, the V_{cal} voltage has to be measured. In fact, for each scan, a well defined amount of charge is injected several times from the PulserDAC using the injection capacitors (see Figure 3.7): C_{inj1}, C_{inj2} or C_{high}, C_{low}. The PulserDAC output voltage which is applied to the injection capacitors has to be known in order to derive the correct amount of charge from the eight-bit DAC value. On the SCC there are pins to measure the output voltage depending on the PulserDAC value: the EXT_INT_SEL pin"A" on SCC has to be connected to the positive side of the voltmeter input and the middle one to the ground but also to the GND (for example the AGND pin) on the SCC. Running a *dac tune scan*, on the STControl scans' lists, it is possible to scan from 0 to 1000 V of DAC steps. A typical result of the PulserDAC calibration is reported in Figure 5.7. The saturation at higher values has to be taken into account later on for the TOT tuning, since with a reference charge of more than 30000 electrons does not work. As shown in Figure 5.7, the result of the scan has a linear trend that can be fitted in the central part with a second order polynomial, with a defined value of the y-intercept and with a slope coefficient. The gradient obtained, which is the line slope, should be close to 1.5 mV/DAC and it has to be entered in the "FE calib" tab of the Front-End configuration, see Figure 5.5.

It should be stressed out that the V_{cal} grad. value, and consequently the amount of charge used for the Front-End calibration, changes after irradiation, showing an increase of around 2% for a proton fluency of 2×10^{15} n_{eq}/cm^2, and of around 9% for higher fluency (5×10^{15} n_{eq}/cm^2). Of course, this is not related with the type of sensor bump bonded but only with the Front-End. The irradiation plans have been done with the Front-End only, without the sensor, in

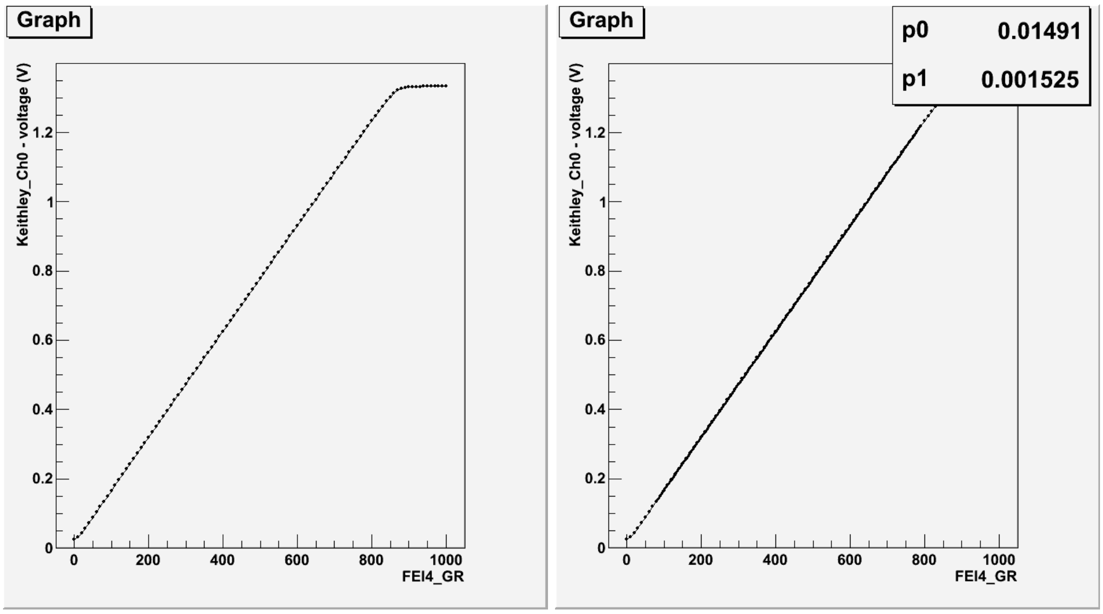

Figure 5.7: V_{cal} measurement of the FBK11 before irradiation. On the left V_{cal} curve. On the right: fit with a second order polynomial. p0 is the y-intercept while p1 is the slope of the line.

December[13].

Sensor	Fluence	V_{cal} grad.*	
	$[n_{eq}/cm^2]$	before irrad.	after irrad.
FBK11	5×10^{15}	1.525	1.66
FBK09	2×10^{15}	1.556	1.59

Table 5.2: V_{cal} grad. values for two sensors: comparison before and after irradiation. * The fit errors are negligible ($\sim \pm10^{-4}$) and therefore are not reported.

5.4.2 Analog and Digital Scan

Once that the charge is injected, to simulate the sensors detector response, it is important to test the Front-End. By doing an *analog and digital scan*, it is possible to study its the analog and digital response.

In these scans, a well defined charge is injected through the Front-End, for each single pixel, several times from the PulserDAC using the capacitance, and read back again (by default, the setting parameters are: C_{high}, V_{cal}=400, q = $400 \times V_{cal}\,\text{grad} \times q_{e^-}$, with a duration of 500 s and a frequency of 8 kHz with a number of events equal to 200). The analog and digital Front-End cells work fine if the same number of events which was injected is read back (200 for the analog scan and 250 for the digital). A good example of these two scans is given for FBK13 in Figure 5.8. The yellow indicates the maximum scale value. FBK13

---

[13] This happened on December 2011, at the Los Alamos National Lab, http://www.lanl.gov/.

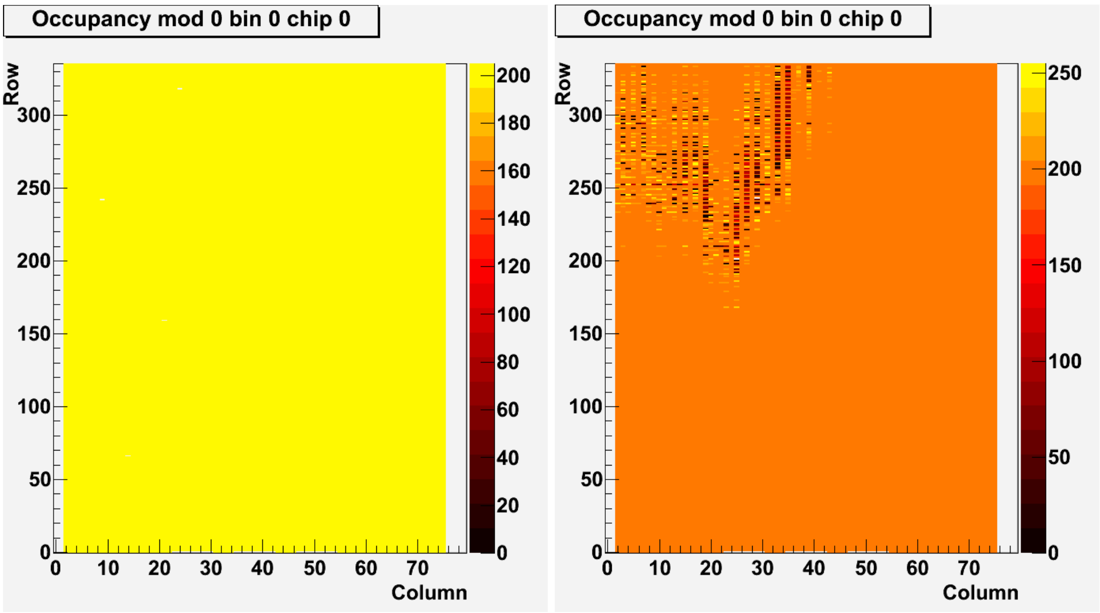

Figure 5.8: Analog (on the left) and digital (on the right) scan for FBK13.

was not irradiated neither with protons nor with neutrons, but the Front-End electronic does not have a perfect response. Both plots should present a uniform color (like from the analog scan) but for this sensor the digital scan shows a spot on the left top corner. At this stage, the reason can be a non optimal response of the Front-End. On the contrary, after proton irradiation, as shown in Figure 5.9 and Figure 5.10, respectively for FBK09 and FBK11, the Front-End suffers the increasing radiation dose. In fact, at a dose of $2 \times 10^{15}\,\mathrm{n}_{eq}/\mathrm{cm}^2$ the defects are still conteined, but already at the irradiation level which the IBL should suffer a larger number of Front-End pixels present problems. In particular, from these two irradiated sensors it seems that the analog part suffers more than the digital one, see Figure 5.10 (top right plot). This effect should be kept under investigation with more samples, since drawing conclusions from the test of only two prototypes is not possible. One different analog test consists in turning off the preamplifiers and switching off the analog circuit and most of the current. Therefore, if when running an analog scan the result is different from an "empty" plot, this means that the analog section of the Front-End is not working properly as shown in Figure 5.11 for FBK13. In fact, later on, doing a *threshold scan* it has been shown that the analog part of the Front-End is separated from the rest of the detector unit. The bump-bonding is disconnected, and the spot on Figure 5.11 is simply noise that goes throughout the Front-End. What is more important to underline indeed, is that for these two types of scan the sensors must be powered with at least 5 V[14] as a bias, to kill the noise, otherwise this goes through the analog part.

---

[14] At least it was notice for the 3D-FBKs sensors.

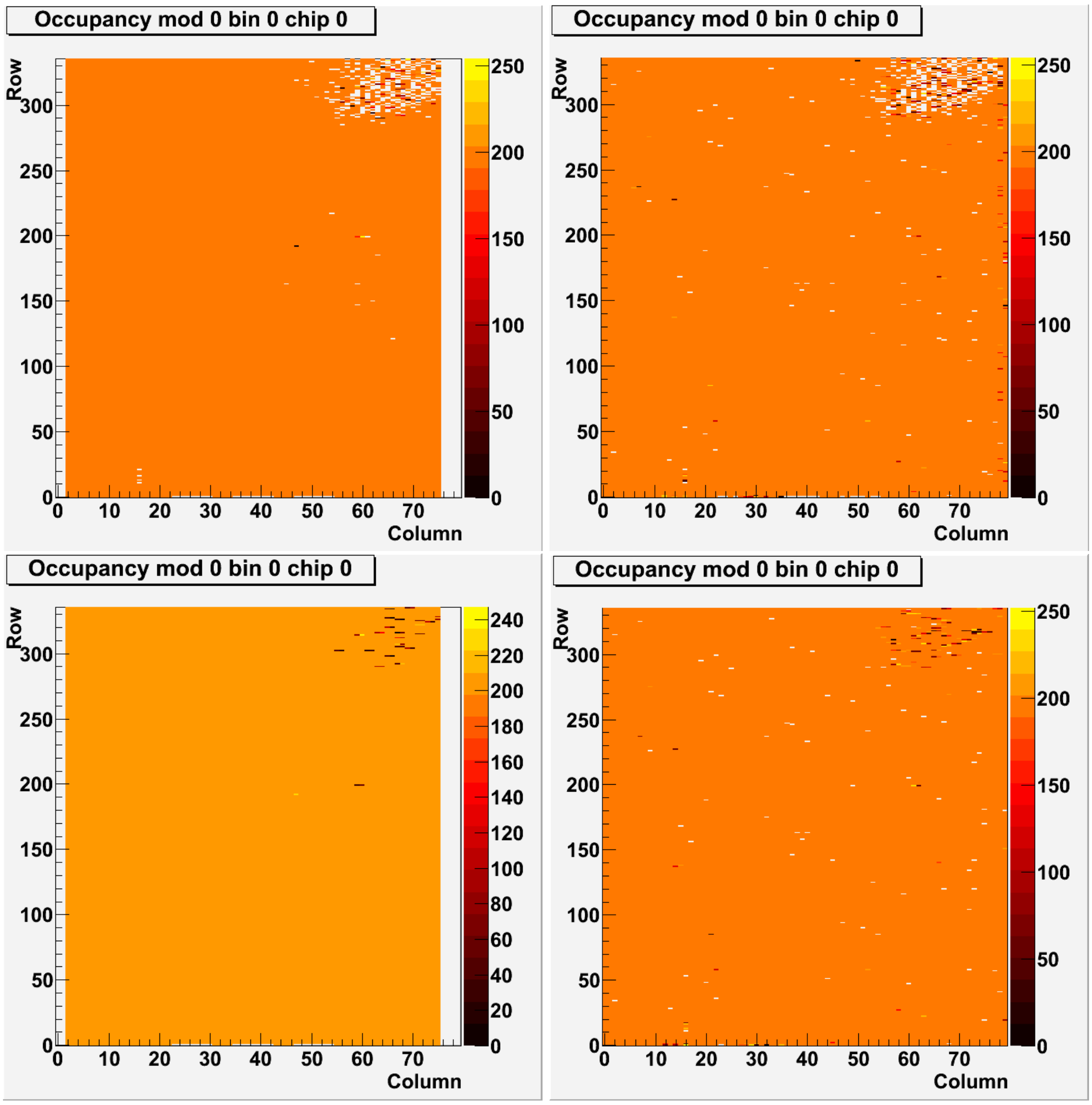

Figure 5.9: Analog (left) and digital (right) scan before (left) and after (right) irradiation for FBK09. At the bottom: digital scan before (left) and after (right) irradiation.

5.4.3 TOT and Threshold scan and Noise

These measurements have been performed at a high voltage of 20 V, after the procedures described in Section 5.5.1.

The *threshold scan* is a key step for the detector calibration and study: it performs a measurement of the threshold and noise of each pixel, in order to check the operation of the injection circuit and to detect disconnected bumps. Basically, it finds the minimum average charge value that can activate the discriminator. For each pixel, the charge released in the sensor substrate, when a particle pass through it, can be above or below a fixed threshold. If the collected charge is above the threshold at the input of the Front-End preamplifier, it is taken into account by the Front-End electronics and a hit is produced in the Front-End output, otherwise no signal is created. For each hit, the Front-End chips give

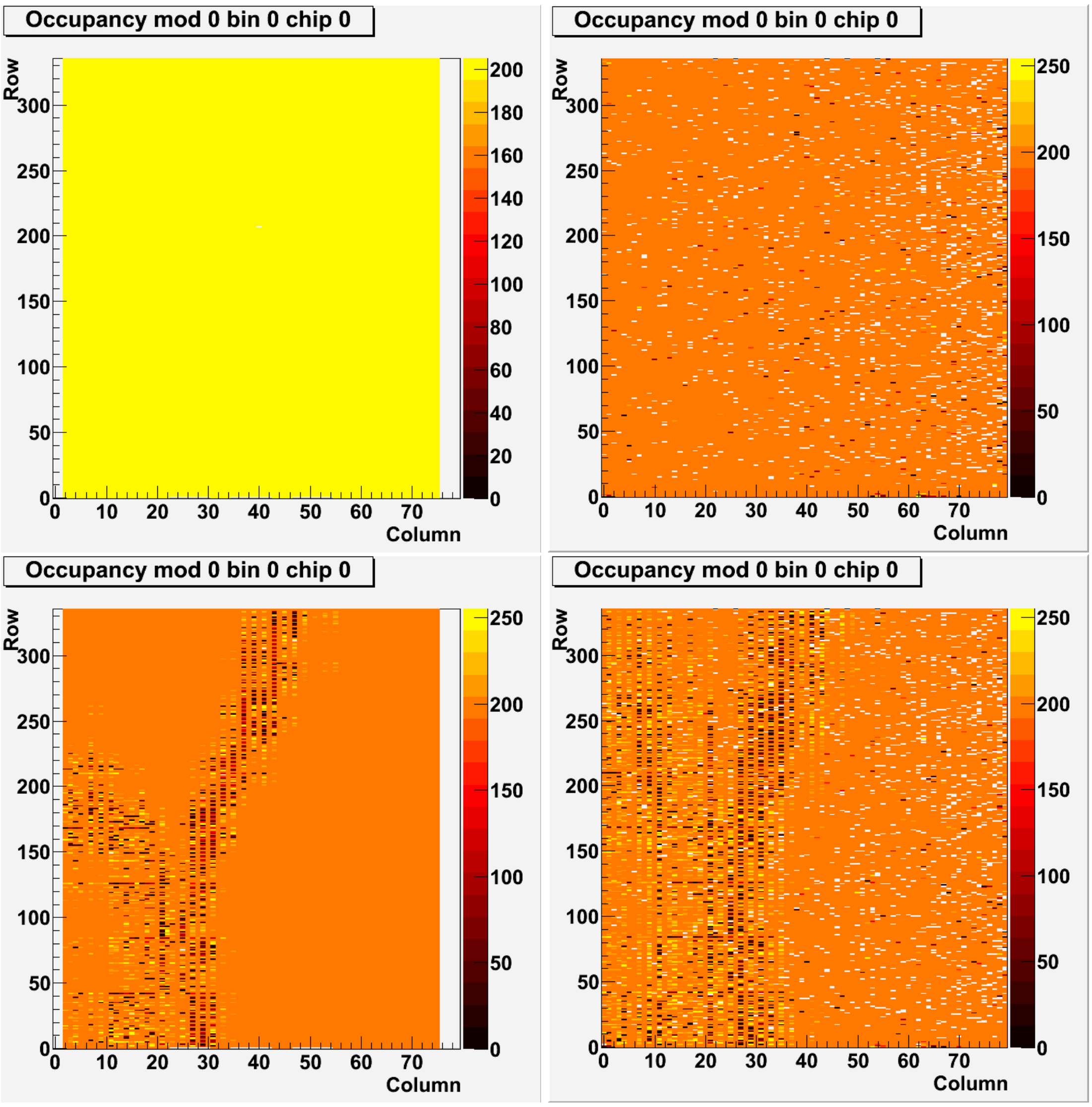

Figure 5.10: Starting from the top: analog scan before (left) and after (right) irradiation for FBK11. At the bottom: digital scan before (left) and after (right) irradiation.

a time-over-threshold (TOT) information, which can be used as a measure of the deposited charge. The TOT needs to be adjusted pixel by pixel to have a dependence on the charge as uniform as possible of the TOT. Due to the sensitivity of the feedback current to radiation damage, it is expected that the TOT changes significantly with time and radiation dose. In more details, what the scan does is to simply repeat 201 (by default, but it can be set to another value) injections per each pixel of a charge value between 0 e^- to 200 e^-. As for the analog and digital scan, the charge injected is controlled by the PlsrDAC pulser. The number of collected hits for each injected charge is recorded and at the end of the threshold scan a so called S-curve obtained (a fit of the error function is done for each pixel). The theoretical result should be as in Figure 3.8, but an example of a real S-curve is as shown Figure 5.12.

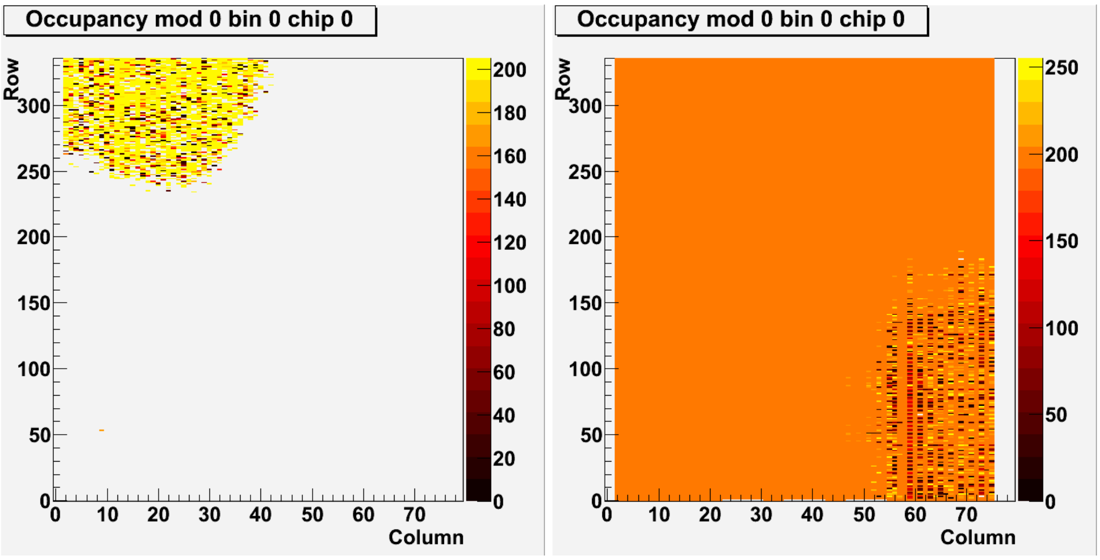

Figure 5.11: Starting from the top left: analog and digital scan for FBK13 turning off the preamplifiers and most of the current.

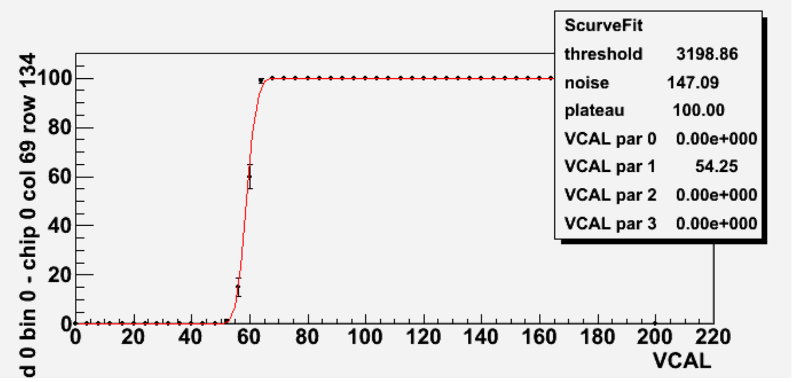

Figure 5.12: Example of a S-curve fir for one pixel: column 69, row 134 at targets values of 3200 electrons, eight TOT for deposited charge of 20000 electrons before irradiation. The S-curve fit belongs to the tuning shown in Figure 5.14.

As already described in Section 3.3.2, by changing the global registers, identified as three parameters inside the Front-End configuration, Vthin, VthinC and VthinAlt, different required threshold and TOT targets can be reached. Due to other priorities a proper study of the influence of these parameters has not been done a part from a first complete study of the dependence of the threshold to the Vthin parameters. However, having performed more scans it has been noticed that keeping Vthin_Coarse equal to zero and changing by 20 Vthin_AltFine, corresponds to changing the threshold of 600 e^-, with a directly proportional relationship; on the contrary with Vthin_Coarse equal to 1 and changing by 100 Vthin_AltFine, the threshold changes of around 1000 e^-.

In the FE-I4 one DAC for the "Coarse" and one DAC for the "Fine" setting of the threshold are implemented. To reach the threshold of around 3200 electrons, the Vthin_Coarse has to be set to zero and one has to adjust the Vthin_Fine value only. As examples, typical values to tune to a threshold around 3200 e^- are shown in Table 5.3.

	Threshold	TOT	FdacVbn	PrmpVbp	PrmpVbpf	Vthin_ AltCoarse	Vthin_ AltFine
FBK09	3200	8	30	43	15	0	114
FBK11	3200	8	30	43	15	0	113
FBK12	3200	8	30	43	15	0	170
	1000	8	30	43	30	0	80
FBK13	1500	8	15	20	5	0	46
	2500	8	15	20	5	0	60
	3200	8	10	40	15	0	85
FBK09*	3200	8	10	43	5	0	210
FBK11*	1500	8	30	25	5	0	95
	2500	8	20	43	10	0	150
	3200	8	20	43	10	0	185

Table 5.3: Main threshold and TOT parameters for the devices under test of 3D-FBK ATLAS09. The symbol * refers to values obtained after proton irradiation.

Unfortunately, not all the configurations before the irradiation of the two samples FBK09 and FBK11 are available, since these studies have been done only recently after irradiation. If one keeps, the FK13 as a good un-irradiated candidate, after proton irradiation the Front-End of the FBK11 sensor, to be able to reach the same target values as the non-irradiated FBK13 (1500, 2500, 3200 electrons) must have an increasing values of the FdacVbn and higher values of Vthin_AltFine as shown in Table 5.3. This means once again that the analog part of the Front-End, and in particular the preamplifier with the FDAC, has suffered and changed his behavior after irradiation, given that a higher current is needed for it to operate at the required working conditions. Another important consideration to mention is that the Vthin_AltFine DAC does not only influence the threshold but also the TOT information. The relationship is inversely proportional to the TOT: to an higher threshold corresponds a lower TOT, because of the falling edge of the analog signal. The measured influence of the Vthin_AltFine DAC on the TOT was studied in [34]. In fact, different parameters are involved to set the TOT. Usually the procedure is to set first the threshold and then try to reach the desired TOT (in Table 5.3 the TOT is equal to 8). To give some numbers as example: to have a TOT equal to 8 requires FDACVbn$=$ 20 (can be between 15 - 20)[15], with an PrmpVbpf $= 10$.

The second information that the threshold scan gives is the noise value. As expected, looking at Table 5.4, after irradiation the noise increase. The last information that the threshold scan provides is shown in Figure 5.13. In fact, the threshold scan for FBK13 shows a spot at the left top corner, darker than for the other pixels. This is due to the fact that this particular region of the Front-End is detached from the sensor as explained previously with the analog scan. Due to this problem, most probably caused by an incorrect step during the bump-bonding process or a transfer issue, the FBK13 has a higher noise value.

---

[15] FDACVbn by default is 30.

	HV	Threshold $[e^-]$	TOT $[e^-]$	Noise $[e^-]$
FBK13	20	1500 ± 33.2	8.5 ± 0.6	184.9 ± 9.6
	20	2496 ± 31.4	8 ± 0.5	176.8 ± 8.9
	20	3198 ± 29.7	8 ± 0.9	143.4 ± 9.8
FBK11*	160	1500 ± 236	8.20 ± 0.6	334.7± 82.6
	160	2503 ± 36	8.4 ± 0.5	193.9 ± 17
	160	3191 ± 35.3	8.1 ± 0.5	191.6 ± 16

Table 5.4: Bias voltage, threshold TOT and noise values for the un-irradiated FBK13, and for the proton irradiated to $5 \times 10^{15}\,\mathrm{n}_{eq}/\mathrm{cm}^2$ FBK11. The symbol * refers to values obtained after proton irradiation.

In particular, in Figure 5.13 which shows the noise as a function of the threshold values, for the three middle plots the small peak which corresponds to the noise, appears for this specific problem and starts to increase at around 100 e$^-$. The same figure, in the three upper plots, shows another interesting effect: the noise is basically concentrated at the column edges (0, 78, 79[16]). The *TOT verif scan* is the next step needed to check the TOT value used for the configuration. The TOT verification scan injects a defined reference charge and reads the corresponding TOT information.

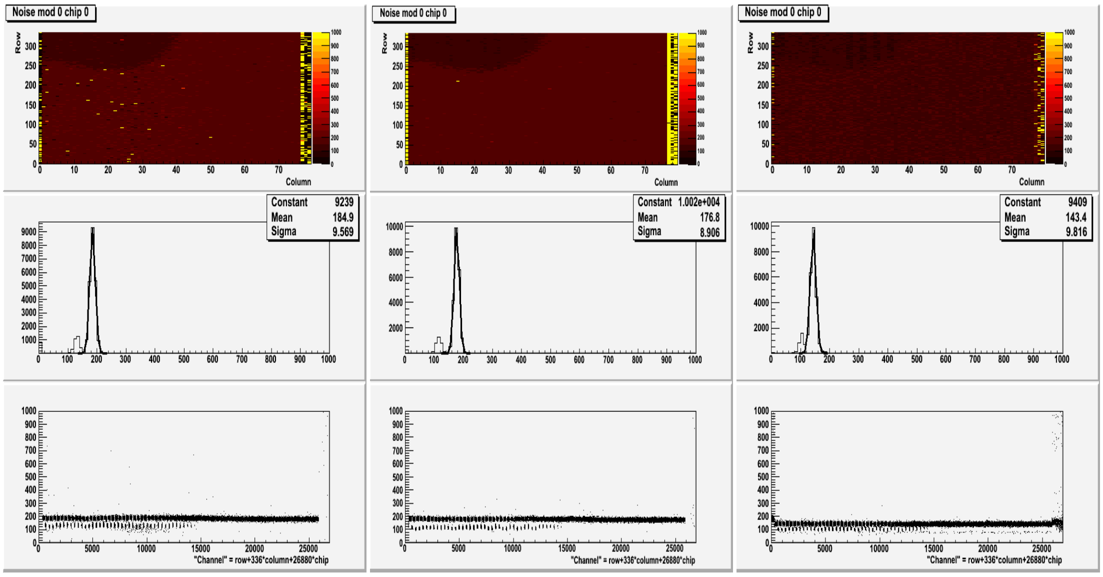

Figure 5.13: FBK13: noise as a function of the threshold. Starting from the left: $1500e^-$, $2500e^-$, $3200e^-$. From the top: noise occupancy for the FE-I4 channels, fit of the noise and average noise.

---

[16] Later on, the first and the last two columns, 0, 78, 79, will not be considered for the tuning. In fact, they are masked since the Front-End has special test structures right on these columns, to test the Front-End. In addiction the STControl software was not complete to perform the tuning for these zones.

5.4.4 Front-End Tuning

Once the starting threshold and the TOT untuned values are known, the procedure to get a certain target values of TOT and threshold consists simply in playing with the parameters listed in Table 5.3.

To be able to work as close as possible to the threshold and TOT desired values a tuning is necessary. To have the required TOT, then run the TDAC tune and the FDAC tune[17] and check the results with the STControl a special left panel has been created and dedicated to load and write a so-called *primlist*. The *primlist* is a list of scans that is possible to run in sequence one after the other, saving time. The *primlist* panel allows a fully automatic execution of a list of actions such as a scan or a "simple tool", like the controller initialisation. Each configuration scan can be edited to change the parameter settings inside, to personalize the scan itself. Currently, the default PixScans are supported and the complete list is available here [86]. Assuming that the threshold and the TOT are close enough to the expected value, the *primlist* used to tune the FE-I4 of 3D sensors is:

1. Rx scan
2. Analog scan
3. Digital scan
4. Threshold scan 1
5. TOT verif 1
6. FDAC tune
7. TDAC tune
8. Threshold scan 2
9. TOT verif 2
10. TOT calib

The first five steps are not mandatory since it can be assumed that the sensor is already connected to the STControl and that the analog and digital part have been tested, but for completeness they are listed. The FDAC tune optimize the TOT information: it will act on the FDAC 4-bit register by changing locally the preamplifier's feedback current. The results will change also the pixels' threshold current, therefore a TDAC tune is required after this scan. The TDAC tune using the PulserDAC injects different charge and checks from the S-curve the actual threshold: if this is higher or lower than the required threshold, another TDAC value for each pixel will be set. This affects only the local 5-bit register TDAC

---

[17] The typical steps to tune the FE-I3 with TurboDAQ are: a threshold scan to a change the GDAC, a FDAC Initial tune to change the TOT by modifying the IF parameter, a TDAC tuning and a FDAC tuning

for each pixel. Depending on the basic parameter values and on the computer system, this scan will take around 15-20 minutes[18] to obtain a threshold of 3200 electrons at eight TOT for a deposited charge of 20000 electrons. Before running the *primlist*, typical register values are TDAC = 7 and FDAC = 15 in the middle of the range of values. After the FDAC and TDAC tuning, two separate maps are created to satisfy the tune requirements. For information, the threshold dispersion for an untuned chip is around 600 electrons, which is too large for the chip to be used (some pixels have a lower threshold and many noise hits, while some others have higher threshold than desired). Figure 5.14 illustrates the effect of the tuning, showing the difference between the pre-tuning situation, a configuration with threshold almost at the desired value of 3200 electrons, and after the tuning. Clearly the tuning improves the accuracy of the threshold reducing the dispersion. Specifically, Figure 5.14 and Figure 5.15 refer to the FBK11 sensor, showing the threshold and the TOT.

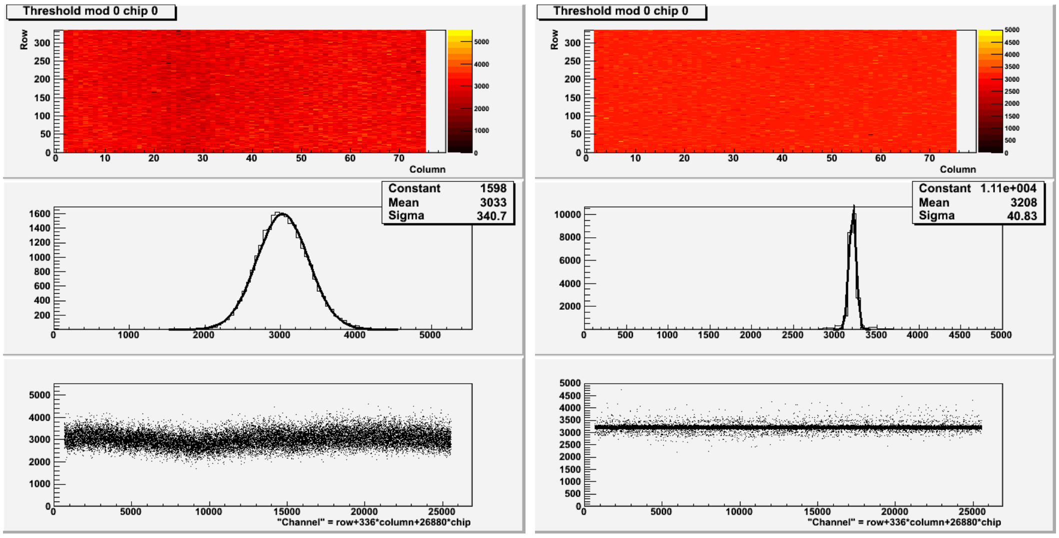

Figure 5.14: Threshold value and dispersion before (left) and after (right) the tuning. The upper plot shows the threshold values in 2D for all the FE-I4 channels, the middle one shows the fit of the threshold values and the lowest one shows is the threshold for all the channels in 1D.

The *primlist* listed above could be also more sophisticated. In fact, it requires to be already quite close to the desired values, otherwise the output result comes out to be not efficient at all. Usually this short *primlist* for the tuning takes one hour to be completed.

5.4.5 Front-End studies

A lot of studies have been done to gain a good understanding of the behavior of the FE-I4 bump-bonded on the 3D sensors. In particular, once the Front-End was tuned, its stability was tested as a function of the different bias sensor supply voltages applied, to confirm the independence of the Front-End from the

---

[18] Or even more if many points are requested to perform the fit.

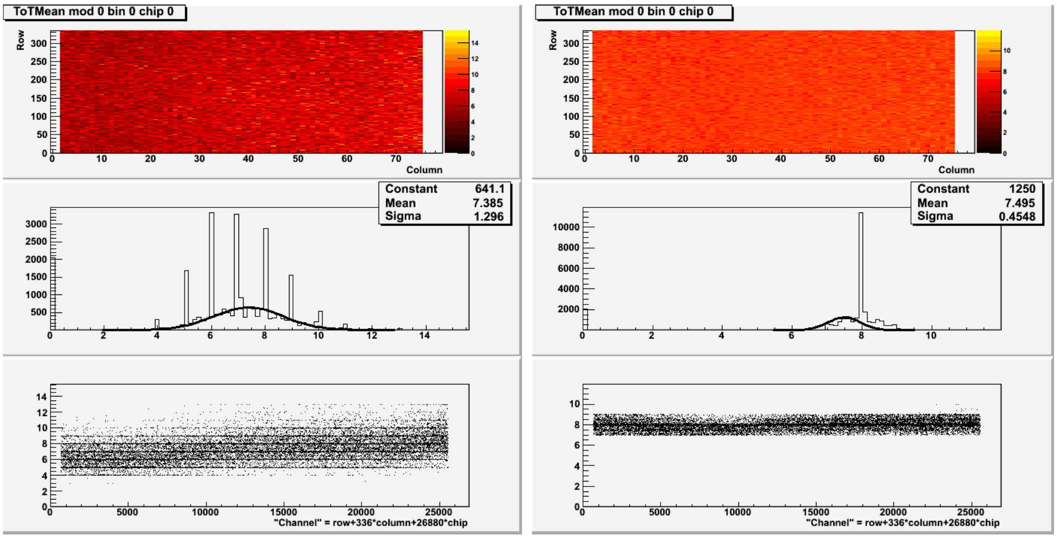

Figure 5.15: TOT value and dispersion before (left) and after (right) the tuning. In order from the top: noise in 2D for all the FE-I4 channels, fit and average noise for all the channels in 1D.

bias sensor. For this purpose, each sample has been tuned at 3200 electrons to eight TOT for a deposited charge of 20000 electrons at the bias voltage of 20 V. As shown in Figure 5.17, keeping constant this particular configuration, a threshold scan as a function of the voltage bias is performed: starting from 5 V up to 40-60 V, depending on the sensor's break down voltage (and leakage current). The same plot shows the threshold dependence after irradiation for the two FBK irradiated devices (FBK09, FBK11).

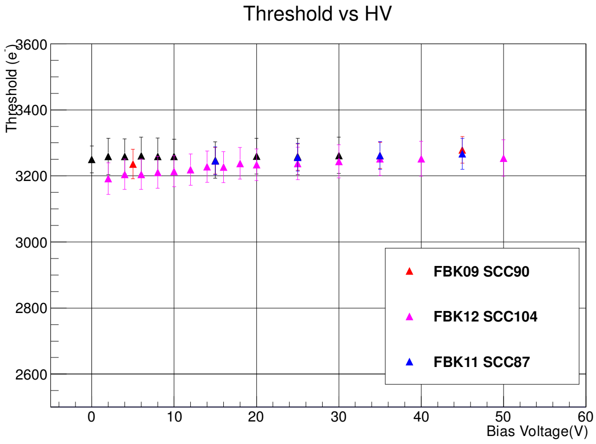

Figure 5.16: Threshold as a function of the applied power supply for un-irradiated samples.

As execked, the threshold does not vary when decreasing or increasing the power supply. This demonstrates the tuning independence from the bias voltage. In Figure 5.17 only three 3D FBK sensor are shown, but it can be assumed the same behavior also for the others. The threshold trend is basically constant, and the values are so close that the FBK09 has almost the same values (same points) as the others FBKs. The bars in the points represent the errors which consist in the dispersion of the threshold values: the larger are these bars, the higher is the dispersion, and the worst is the tuning used. In this case, the result shows almost constant bars which means that the tuning, once again done at 20 V, stay constant for lower and higher supply voltages.

The study has been repeated after the proton irradiation, to look at the effects of the irradiation on the sensors and on the Front-End. Figure 5.17 shows that the voltage range is changed, going to higher voltage values, but still keeping the bias voltage below the sensor's breakdown (see Section 5.5.2). The same considerations can be applied here: the threshold trend is basically constant for different bias voltages.

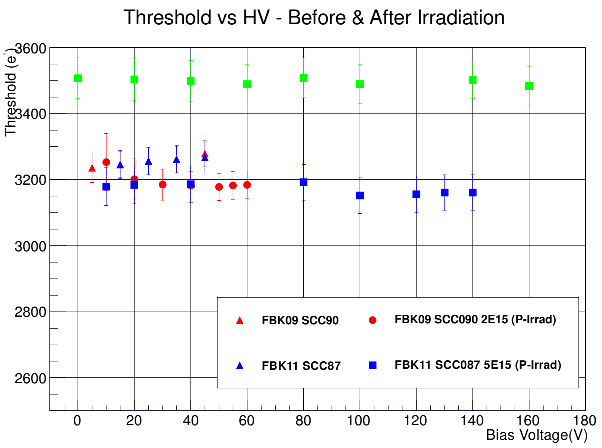

Figure 5.17: Threshold as a function of the applied power supply: comparison before and after proton irradiation for FBK09 (2×10^{15} n_{eq}/cm^2) and FKB11 (5×10^{15} n_{eq}/cm^2).

By doing a threshold scan, a noise scan is performed as well, whose results are reported in Figure 5.18 at the bias voltages, previously plotted in Figure 5.17. The noise is calculated as in Formula 3.2 (described in Section 3.3.2). This plot demonstrates that the noise is constant when varying the bias voltage. Indeed, what is more interesting is what Figure 5.18 shows: the FE-I4 noise study before and after irradiation. As expected, after irradiation the Front-End is more noisy: FBK09 passes from an average of about 150 e^- to around 160 e^-. FBK11, subjected to a higher irradiation fluency, has a higher noisy value (around 250 e^-) compared to 150 e^- before irradiation. The increasing noise is consistent with what expected from the theory: more irradiation implies more noise Front-End chips. It must be underlined that the result showed in Figure 5.18 has been obtained in Genova always using the same setup system. In fact, all the values presented here are related also with the laboratory setup (the same threshold scan repeated at CERN showed a lower noise value, around 190 e^-), however these fluctuations can be included in the error bars.

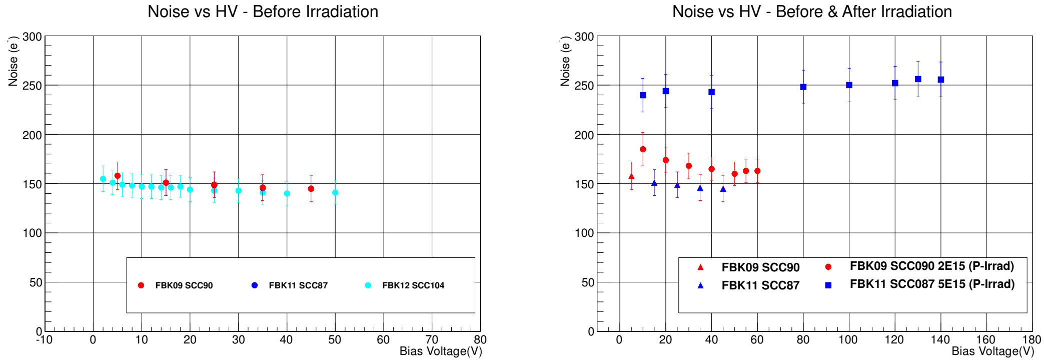

Figure 5.18: Noise as a function on power supply applied: comparison before (left) and after (right) irradiation.

5.5 Sensor Characterization

5.5.1 IV Measurements

Most of these measurements, as well as the previous bump-bonding, have been done at the INFN Genova and, just few of them at in the Bonn University. To identify where the wire bonding has been done, a prefix 'Ge' or 'Bon' is used respectively to identify the Genova or Bonn devices, see Table 5.1.

The measurements described in this section consist in evaluating the output current as a function of the given voltage (IV curves). The main aim of these measurements is to know where is the breakdown voltage of the detector, keeping the FE-I4 chip off. Once this value is known, the operation working point can be decided: the sensor has always to be operated at voltages well below the breakdown in order to work in safety conditions without risking a damage or to break it. Another important outcome from this measurement is the possibility to check for sensor damages after dicing and flip chipping. The IV curve provides the better bias voltage to be applied for working in conditions full depletion (and under thermal stability), to collect more particles having a uniform electric field between the columns. Therefore, at the end, the IV measurement, together with the other scans, can give a precise description of the sensor itself.

An overview of all the IV curves for 3D-FBK detectors from the ATLAS09 batch is shown in Figure 5.19, where the breakdown occurs at a voltage between -35 to -45 V for the majority (eight sensors which are considered as good devices), and lower than -20 V for few of them (seven sensors). As it has been already described in Section 4.5.1, the 3D sensors normally present a breakdown voltage higher than 20 V. If some of them are below this value, this can be related to the presence of local defects likely occurred during the assembly.

The voltage range used to plot the IV curve has been fixed to be between 0 to -60 V (at -20 V is the expected breakdown as predicted by the simulations), with voltage steps of 2.5V and with 10 seconds of waiting time between measurements. This time parameter was decided in order to have the current value as much stable as possible during the increase of the supply voltages. In fact, when starting from 0 V and increasing the voltage, the sensor becomes warmer and

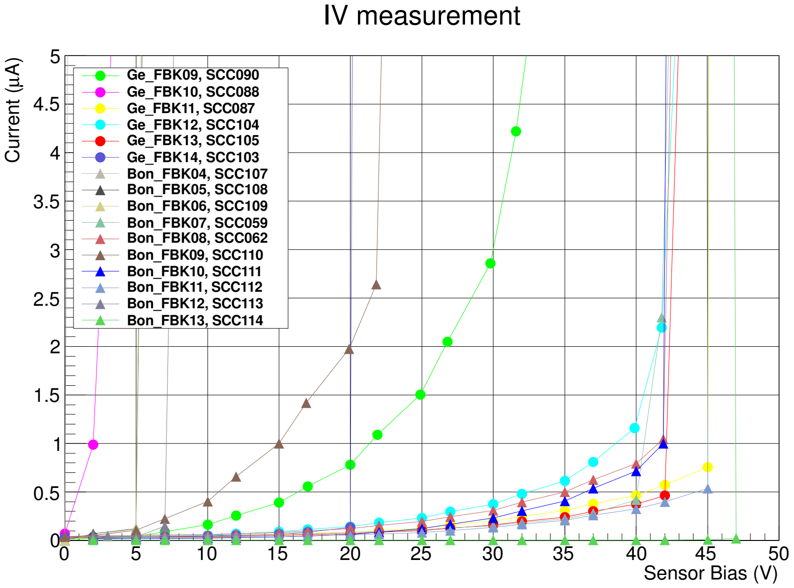

Figure 5.19: IV curves for 3D-FBK detector from the full ATLAS09 batch at 20°C: the prefix "Ge" or "Bonn" is used to identify where the measurement has been done: Genova or Bonn respectively.

this affects the measurement of current making hard its stabilization. Moreover, the measurement was repeated until two consecutive readings where differing by less than 1%. The compliance current was set to 200 μA (using the source meter Keithley 2010). As a matter of fact, other 3D sensors, like SINTEF, showed a change of the current measured with the waiting time. On the contrary, for the FBK sensors no such effect appeared. The IV curves have been obtained at the same temperature conditions: 20° C inside the climate chamber, since the current is temperature depending, as requested by the specifications. An example is given for one device, FBK12[19] (see Figure 5.20). The measurements were done also at different temperatures, from -20° C to 20° C, and the trend does not change so much since the devices were not irradiated. In fact, the biggest component of the leakage current of a module before irradiation is the surface current: the temperature is not so critical. A leakage current of the order of 0.5 μA is acceptable. An early breakdown was noticed for some devices, six, and this was related to the fabrication process.

All these measurements were done keeping the Front-End off. Indeed, switching on the Front-End, an increase of the current to about 100 μA was noticed. It is important to stress that a resistance, identify as R3, of 100 kΩ is mounted on the SCC, in serie with the detector. Therefore, the current read is the real one, but to have the real voltage applied one has to subtract the voltage drop on the resistance R3. All the plots shown here, have the effective real voltage applied across the sensor[20].

For comparison, to underline the improvement of the ATLAS09 with respect

---

[19] For all the other detectors the same behavior was observed.

[20] $V_{det.}$ = HV - I$*$R3.

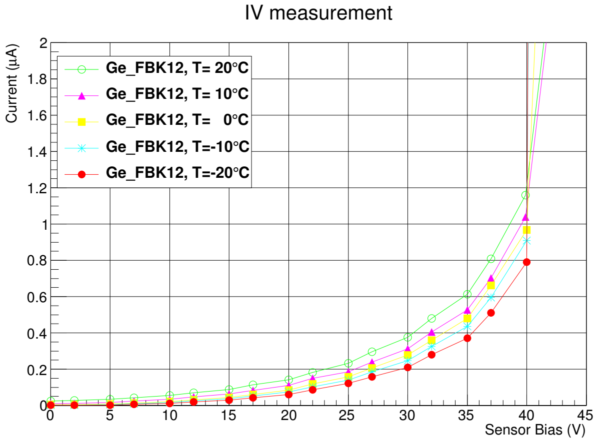

Figure 5.20: IV measurement for FBK12 with FE-I4, for the batch ATLAS09. Example for an un-irradiated sensors at different temperatures.

to the previous version, the IV measurement of the sensors belonging to batch ATLAS07, is shown in Figure 5.22. Looking at this figure, it is clearly visible an extremely low break down voltage for all the sensors. As already explained in Chapter 4, Section 4.3, this is related to the p-spray dose which was too high causing as expected a lower breakdown voltage. Due to the restricted time available, there are not additional studies performed on this batch.

5.5.2 IV Measurements of the Irradiated devices

There were two irradiated 3D-FBK sensors irradiated with protons in Karlsruhe (Germany) up to 2×10^{15} n_{eq}/cm^2 (FBK09) and another one up to 5×10^{15} n_{eq}/cm^2 (IBL fluency, FBK11), see Table 5.1. The parameter setting for the current measurements was different with respect to the un-irradiated devices, as described in the previous Section. The IV measurement, always done with the Front-End chip Low Voltage (LV) off, has been taken at different temperatures: -40°, -30°, -20°, -10°, 0° C. The reason for this differences is due to the fact that the irradiated devices have a higher leakage current. Consequently, to be able to operate in a safe mode the operational temperature has to be low. The temperature was kept under control in a climate chamber. In addition a NTC resistance was left 'open-air' inside the climate chamber to double check the air temperature. The real temperature on the sensor itself (keeping off the Front-End chip) has been estimated as being around the air temperature plus 10° C[21].

The voltage was set from 0 to 200 V, with 500 μA as current compliance, and with voltage steps of 5 V due to the irradiation damage effects on the substrate. As before, the waiting time between different measurements was of ten seconds, see Figure 5.23. Figure 5.23 shows a very similar behavior, and the breakdown is clearly visible at 60 V for the FBK09 and between 120-160V for the FBK11 at -20° C. Once again, at higher temperature the current is higher and the breakdown,

---

[21] Value estimated by reading the temperature during the Beam Test, where the temperature monitoring was performed closer to the sensor, see Figure 6.4 in Chapter 6.

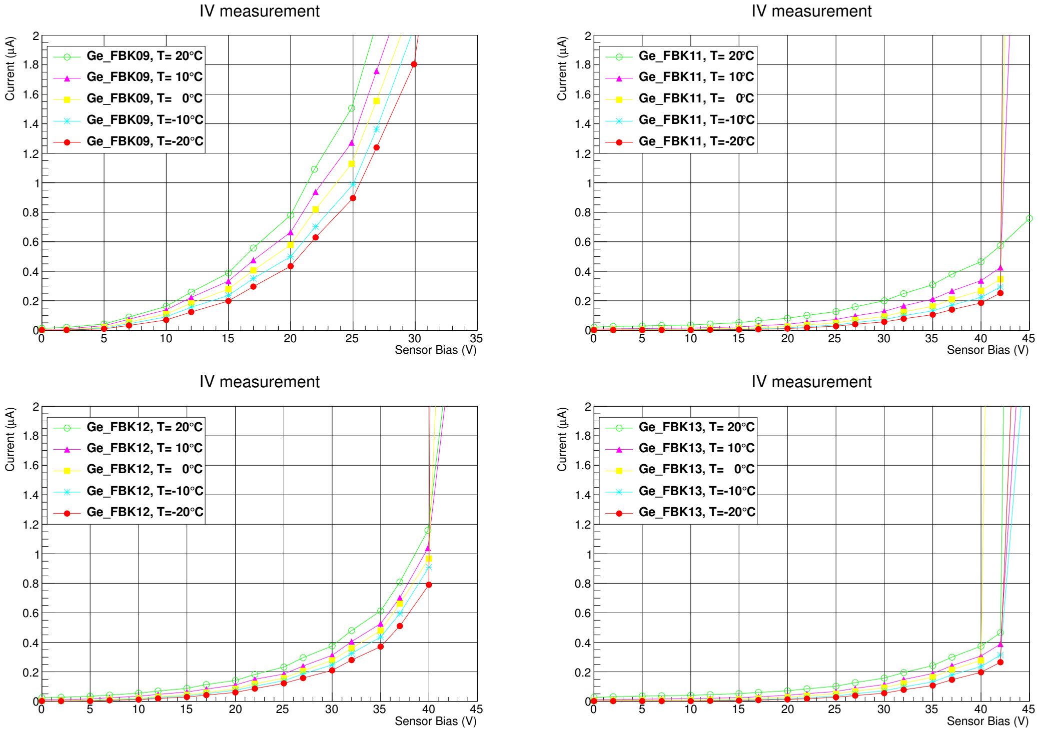

Figure 5.21: IV measurement for four un-irradiated sensors (FBK09, FBK11, FBK12, FBK13) at different temperatures.

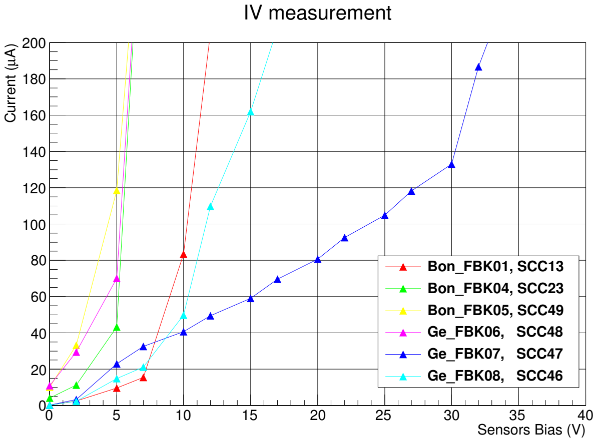

Figure 5.22: IV measurement for batch ATLAS07 after bump-bonding. Batch with FE-I4, measurement at 20° C.

for temperatures higher then -10° C, is not visible due to the compliance value set to 500 μA, to prevent possible damages.

The high-current level which appears after irradiation is mostly induced by bulk damages which may cause thermal runaway, as already discussed in Section 1.8. The current increases and the consequent operational voltage leads to an increasing power dissipation (which heats the sensor, increasing once again the current, with a positive feedback). Moreover, the high current drives local

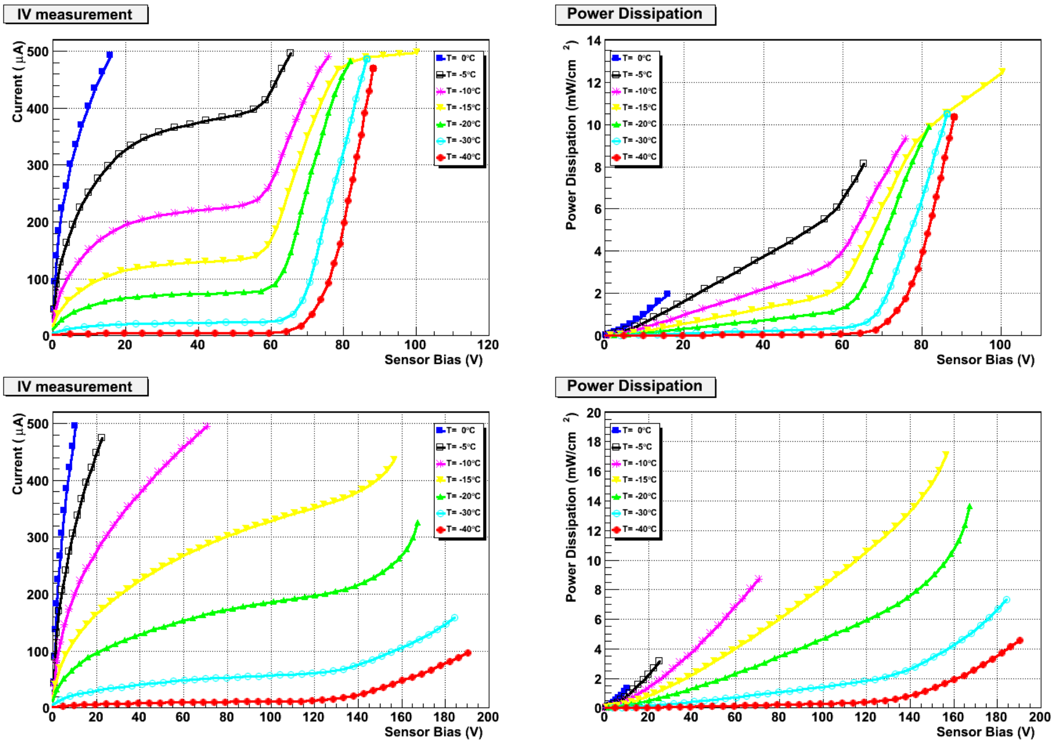

Figure 5.23: IV measurement and power dissipation for the two FBK proton irradiated. Top: FBK09 proton irradiated to $2{\times}10^{15}\, n_{eq}/cm^{-2}$. Bottom FBK11 proton irradiated $5{\times}10^{15}\, n_{eq}/cm^{-2}$.

electrical breakdowns (sometimes referred to as microdischarge) which create a current increase in some local restricted detector areas. The interested parts are a restricted number of channels that normally drive the Front-End preamplifier into saturation. This can be avoided by masking the noisy channels in order to them and not to extend the problem to the neighbor pixels. Usually, this is the region (“spot”) where the breakdown starts.

Figure 5.23 shows also the power dissipation on which there is one of the IBL requests to the sensors. However, for the 3D technology this is not such a critical restriction as for the planar technology, since the current is low enough not to be worried for for what concern the power dissipation. Another consideration involves the current: as expected, it is increasing with the irradiation fluence that the device has received. In this case, the FBK11 presents a higher current compared to the FBK09. Extrapolating this information, with the caution required because of the low statistics available, it possible to plot the operational voltage trend, as illustrated in Figure 5.24. Few remarks can be made looking at this plot: the current, not showed, as the voltages strongly depend on the voltage breakdown and moreover on the environment and sensors temperature. It is not unrealistic to say that with other irradiated sensors the trend could be a bit higher or lower but should maintain an almost linear behavior.

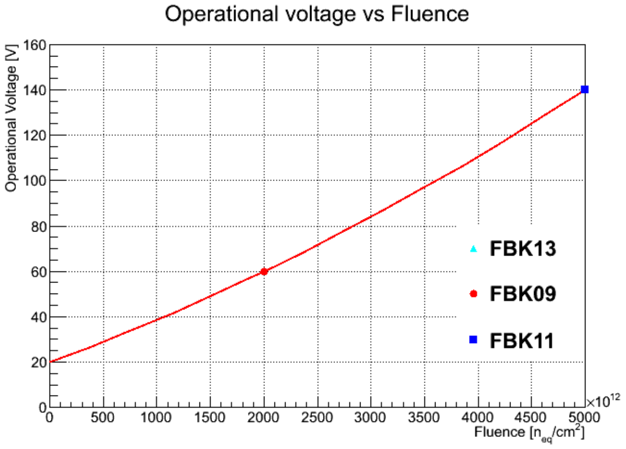

Figure 5.24: Operational voltage as a function of the irradiated fluence.

5.5.3 Charge Collection

After having measured the IV curve, defined the working point and tuned the Front-End, the next step is to perform a source scan. Thanks to this, it is possible to test the sensor functionality by measuring how much charge can collect the sensor if hit by particles of known energy emitted by a radioactive source. Here the Am^{241} γ-source and the Sr^{90} β-source have been used.

In more details, the Americium source is used to check the tuning of the devices while with the Strontium source scan it is possible to estimate how much charge can collect the sensor. In fact, with the Sr^{90}, it is possible to have a laboratory simulation of the charge collection during a test beam, as explained in Chapter 6.

To study the charge collection of 3D sensors with these two sources, two specific setups have been built up. For the Am^{241} measurement, the self-triggering of the USBpix has been used. As described in Section 5.3.1, on the Multi-IO Board the RX0 LEMO connector was shorten with a TX1 LEMO connector to use the hitbus as external trigger signal. The Am^{241} source was sitting on a holder placed right above the SCC centered to the sensors to align the source with the sensors on the SCC. On the contrary, for the source scan with Sr^{90} the trigger was taken from a scintillator placed below the devices under test (see sketch of the setup in Figure 5.25). The scans have been performed in Genova with the γ-source, where no external trigger was requered, and in Barcelona for the β-source, which instead was requiring an external scintillator system for triggering.

All the ATLAS09 sensors have been tested with Am^{241} (10 mBq[22]) in Genova, before sending the samples to irradiation (FBK09, FBK11). At the beginning, running this scan with the STControl, no masks have been applied for the noisy pixels. In fact, to determine these noisy pixels a source scan with a low number of event (less than 5000) is run. In addition, the STControl provides an independent scan called *stuck pixel scan*, which identify the pixels with this problem,

---

[22] Becquerel SI-derived unit of radioactivity defined as the activity of a quantity of radioactive material in which one nucleus decays per second.

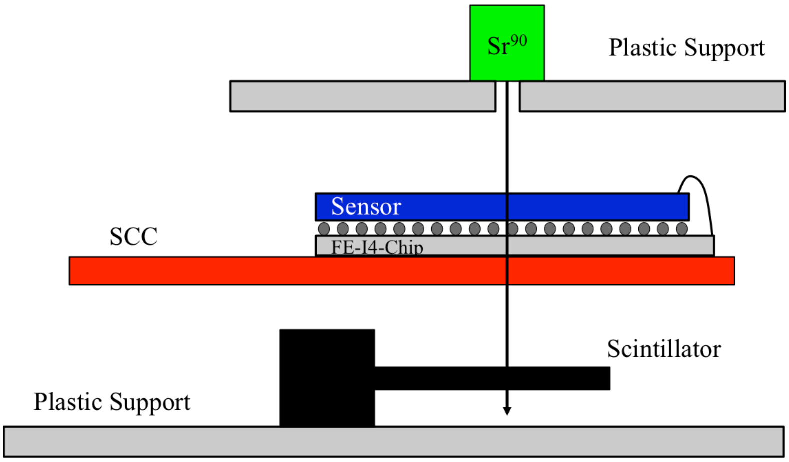

Figure 5.25: Sketch of the Sr^{90} source scan setup as done in Barcelona. The figure is not in scale.

so that it is possible to mask them. Once these pixels are identified and masked inside the configuration, a typical hit map of an un-irradiated sensors is shown in Figure 5.26. In general, for source scan, 500000 events are enough to have a good statistics[23]. It must be stressed that since the USBpix is relatively new and the Front-End studies together with the STControl software development are just started, no conversion from TOT to charge is available (all the plots here reported will be in TOT not in charge). The sensor configuration used to run a source scan for un-irradiated devices is the following: 3200 electrons for eight TOT for a deposits charge of 20000 electrons. Looking at the results reported in Figure 5.27 it is not possible to give an exact charge number to establish how much charge a 3D sensor can collect. Assuming a perfect tuning of the sample, which is not true in the real case, a TOT equal to 5 - 5.5 is shown for the Am^{241} source assuming that a charge around 12500 electrons is collected. From the theory around 16.5 ke^- are expected for the γ-source. For the 3D-CNM the sensor the output is a bit higher since at high voltages, more than 30V, a TOT of 5.6 is reached. This means, about $14ke^-$. In Table 5.5 a summary of the results is listed.

The results shown in Figure 5.27 are affected to by some uncertainties, like the TOT errors from fitting, not perfect and equal calibration. Figure 5.28 shows a good example of the fitting charge (TOT) plot. It shows a source scan result with Am^{241} for the FBK13 at a bias voltage equal to 35 V.

The result for the γ-source scan is reported in Figure 5.29 which shows a comparison of the charge collection for FBK13 and CNM10[24]. The charge collected is once again in TOT units, and a Sr^{90} (2 MeV electrons) is used with a scintillator trigger. Both devices where tuned in the same way: threshold of 1500 electrons, 10 TOT for a deposited charge at 20 ke^-. The environmental conditions were the same (i.e. temperature and set-up instrumentation), but it must be underlined that some unknown factors with the TOT calibration occur in the measurement (like TOT errors from fitting, not perfectly equal calibrations

---

[23] 500000 events/(80×336 pixels) = 18.6 ∼ 20 hits per pixel

[24] The measurements for CNM101 where done in IFAE-Barcelona.

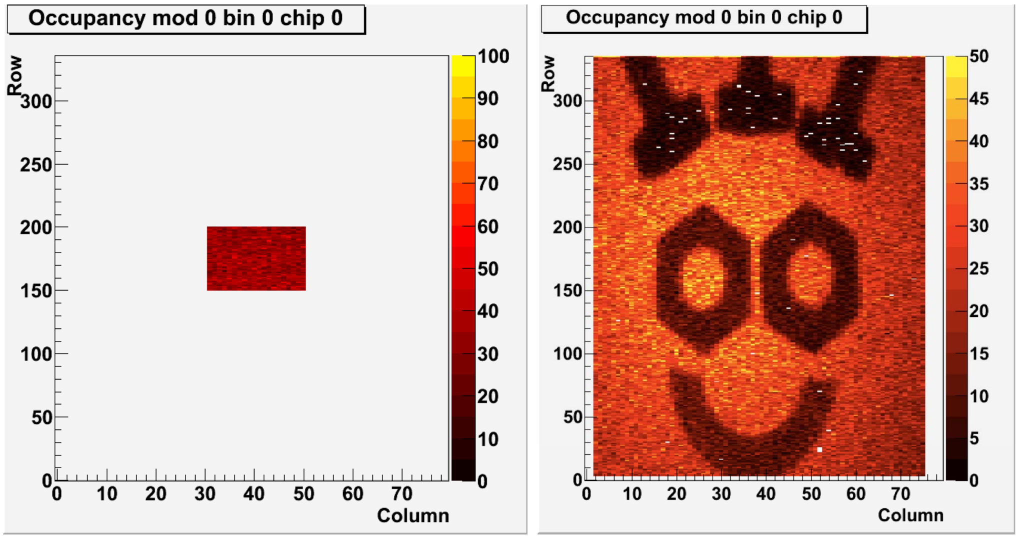

Figure 5.26: Source scan with Am^{241} for the un-irradiated FBK11 and FBK13. The left plot shows the FBK11 case, where a mask was applied to the Front-End to enable only the central part of the sensor. Due to a STControl problem it was not possible to run a source scan with more than 30000 events per time without crashing the system. The plot on the right shows the FBK13 case, where a newest version of the STControl, without the old problems, was available. The face represents the scan of some metal pieces placed above the Front-End (three screws, two nutcase and half part of a spacer). It is also possible to see the spot of the source in the middle of the sensor (yellow part).
Both scans were done at 20 V with the Am^{241} source.

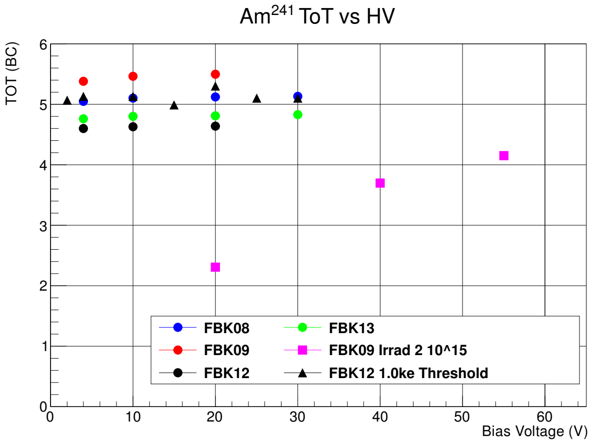

Figure 5.27: Collected charge as a function of the bias voltage for the 3D-FBK devices.

etc.). Unfortunately, the test was done with only one FBK, but the plot shows an interesting result. In general, the 3D-FBK layout with full columns can reach the signal saturation at lower charge compared to the 3D-CNM (with IBL layout, see Figure 4.15). The FBK specification demonstrates a saturation already at 6-7 V that is compatible with is shown in Figure 5.29. In fact, this can be explained

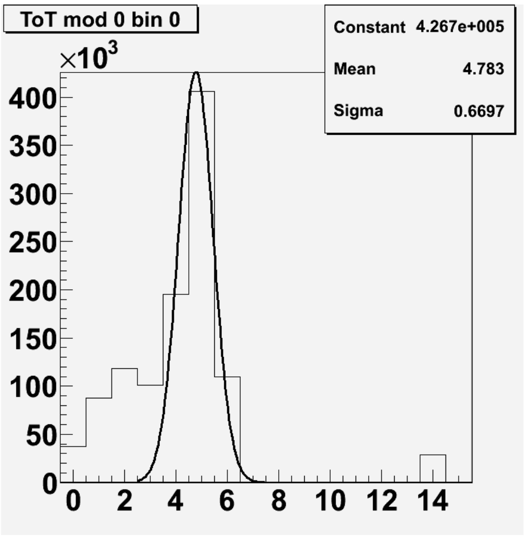

Figure 5.28: Example of a fit for a source scan output where one can see the peak of the charge (in TOT units) for an Am^{241} source. The plot shows the precision of the fit itself for a FKB13 un-irradiated tuned at 3200 electrons, with eight TOT for 20ke$^-$ at a bias voltage equal to 35 V. The entries at a TOT equal to 14 represent the overflow values.

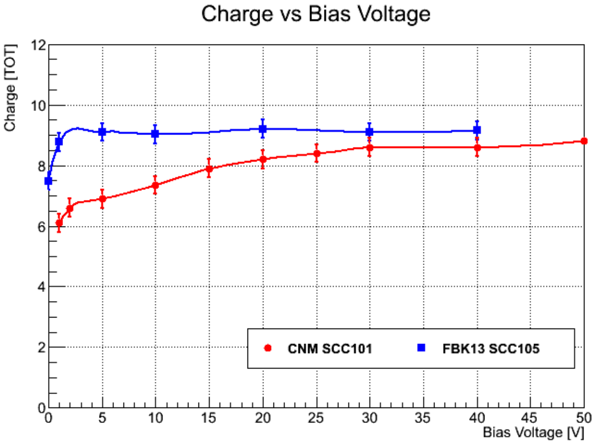

Figure 5.29: Collected charge (in TOT units) as a function of the bias voltage for 3D-FBK13 compared with 3D-CNM101.

by the column depth of the sensors. It is easier to achieve the full depletion region between columns with the full passing through columns (remind that the CNM columns are shorter and stops at around 10 μm to the opposite wafer side). However, at high voltages, the difference in the collected charge at the saturation is very low, as expected from simulation.

5.5.4 Noise Occupancy Studies

To detect the noisy pixels is important, as well as to mask them and avoid bad performance of the detector, keeping active only the good part of the Front-End.

	HV [V]	Threshold [e^-]	TOT [BC]	Peak of Am^{241} [TOT]
FBK12	30	1003	8	5.3
	30	3244	8.0	4.6
FBK13	30	3218	8.0	4.8
Bon_FBK08	20	3200	8.0	5.1
Bon_FBK09	20	3200	8.0	5.5

Table 5.5: Am^{241} source scan results. Since no TOT to charge conversion is available, the comparison is in TOT units. The TOT values are the fit to the TOT verification scan obtained at the end of the corresponding tuning, while the TOT Am^{241} peak is the TOT fit from the result of the Americium source scan.

Inevitably, each sensor and Front-End comes out with a certain number of noisy pixels. Due to these, which create noise hits, the tracking efficiency of the Pixel detector decreases and if not masked the noisy pixels have the effect to limit the data bandwidth with a consequent decrease of the tracking performance. Another consequence is that the informations linked to a real particle passage, can be hidden or partially covered. This leads to a failure in the measured impact of the particles due to the wrong measured track. Measuring the noise occupancy per pixel, which is the number of noise hits per bunch crossing, is the most realistic test noise since all the possible sources are involvedand the area where the noise appears can be detected [87]. The FE-I3 was designed with the aim to have less than 10^{-6} noise hits per bunch crossing and pixel [21]. This is even undershot by the FE-I3, which has a noise occupancy of 10^{-7} per pixel in the full module configuration, with a threshold of 4000 electrons [88].

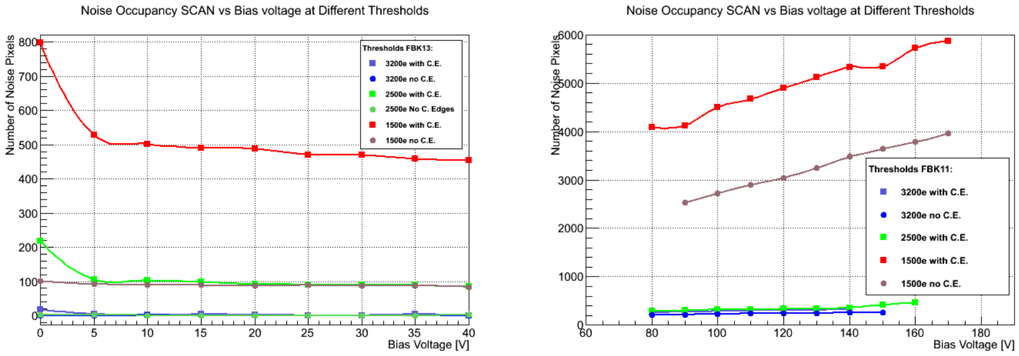

Figure 5.30: Noise occupancy scan for un-irradiated FBK13 (left) and proton-irradiated FBK11 (right).

This analysis is different from what already reported in Figure 5.18. In fact, the *noise occupancy scan* uses the positive edges of the Hitbus to generate the

Level1 trigger requests to the Front-End: every hit detected is read and the number of hits is counted for every pixel. Therefore, the noise occupancy is given by the possible number of noise hits over the number of bunch crossing over the time, or rather:

$$NoiseOcc = \frac{\text{number of hits in the pixel}}{\text{time[bunch crossings]}} \tag{5.1}$$

With this method, all the pixels are taken into account simultaneously and every noise hit is read. Therefore, the sensors were kept in the darkness to limit any possible external sources of noise (i.e. light).

The scans have been performed at CERN for the FBK11 and the results are reported in Figure 5.30. The sensors were tuned at three thresholds comparing three different configurations: 1500 e$^-$, 2500 e$^-$, 3200 e$^-$ at eight TOT, which in turn have been split in those with or without the column edges enabled. Apart for the three configurations with disabled column edge (columns: 0, 78 and 79), the scan was done taking enabled all the pixels, in order to insert all the possible causes of noisy pixels. To perform a noise occupancy scan a number of events equal to 10^7 is enough. The distribution of the number of noisy pixels as a function of the bias voltage for the three different thresholds, is shown in Figure 5.30. The noisy pixel decrease with a higher threshold, while the effect of the edges is more marked at a lower threshold. Moreover, as expected, the noise increases with the bias voltage at low threshold, but it is basically constant at 3200 e$^-$. After irradiation, at the threshold of around 1500 e$^-$, the number of noisy pixels starts to rise with the bias voltage. Due to the low threshold, more noise is generated by the sensor which goes throughout the Front-End and therefore is readout. With a threshold equal to 2500 e$^-$ the number of noisy pixels is much lower than 1500 e$^-$ which, comparable with a higher threshold of 3200 e$^-$, represents a good compromise between the two extremes. These results were taken in to account to select threshold values and therefore decide the best configuration for the charge collection studies at the beam tests, in order to have a good compromise between noise and signal.

Chapter 6

Beam Test Measurements

To qualify the performance of the 3D devices, a lot of beam test measurement have been performed at the CERN, and DESY (Hamburg, Germany) laboratories. Since 2009, dedicated 3D beam tests were organized twice per year at CERN, while starting from the last months of 2010 a combined IBL beam test studying 3D and planar sensors together have been performed. During 2011, four beam tests where set up for the IBL Sensor Qualification procedure: the first FE-I4 Planar Pixel Sensors (PPS) assemblies, as well as some FE-I3 PPS and 3Ds, were tested between February 16th and March 3rd, the second with only FE-I4 devices in April (4th - 22nd). These two beam tests were organized at the DESY laboratory while the remaining two at CERN in June (6th - 18th), at point H8, and in September (September 26th - October 2nd), in point H6. In this Chapter, only the results of the analysis of the last two IBL beam tests for the 2011 at CERN that I have done, are presented. The June beam test was critical to test irradiated devices to the nominal IBL fluence (5×10^{15} MeV $\mathrm{n}_{eq}/\mathrm{cm}^2$) for both the planar and 3D technologies.

6.1 Beam Test Instrumentations

3D silicon sensors were tested and characterized in data-taking at the Cern SPS[1] North Area. The IBL beam test used the H6 and H8 beam lines with a 120 GeV/c π^+ beam and the European Detector (EUDET) beam telescope [89] to reconstruct the tracks. The setup is shown schematically in Figure 6.1.

The Super Proton Synchrotron (SPS), a circular proton-proton accelerator of 2 km diameter with an energy in the center of mass of 450 GeV[2] it has several beam lines to extract particles for the beam tests which can be modified by properly adjusting magnets and collimators depending on the experiment's requests. Its main functionality is to inject protons and heavy ions into the LHC, it can also provide its own beam lines for fixed-target experiments. Since there is not only one experiment, the order of injections and ejections is arranged in the so called SPS super cycle. The number of triggers per spill is of the order of 4000 - 5000

---

[1] Super Proton Synchroton - protons at 400 GeV

[2] Operated in the past as proton-antiproton collider and also to accelerate electrons and positrons injected into the Large Electron Positron Collider (LEP).

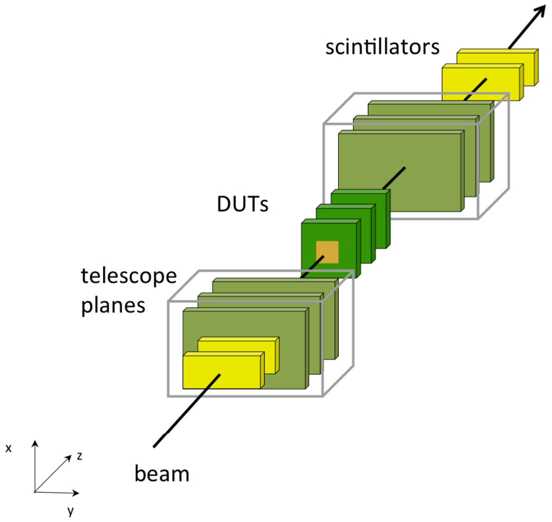

Figure 6.1: Schematic view of the EUDET test beam setup.

spill (a spill length or spill repetition frequency is 10 seconds long repeated almost every 45 seconds[3] [90]).

The EUDET Pixel Telescope, consists of six planes separated by about 40 cm, distributed before and after the Devices Under Tests (DUTs). The core of the telescope is the Mimosa26 pixel sensor, characterized by a pitch of 18.5 μm. Each sensor has 576 × 1152 pixels covering an active area of 10.6 × 21.2 mm^2. Triggering was achieved by the use of two up- and two down- stream sets of 1 × 2 cm^2 scintillators positioned at 90° with respect to each other and connected to the EUDET data acquisition (EUDAQ) system. DUTs were located between the two telescope arms and mounted on remotely controlled rotating stages. The EUDET tracking resolution has been estimated to be about 3 μm. The trigger rate was of the order of 200-300 Hz during normal operation. The sensors Front-End chips were readout with the USBPix system. Tracks were built with the EUTelescope reconstruction package [91]. The purpose of this telescope is to characterize the Front-End and sensors performance before and after irradiation at different tilted angles with the usual figures of merit, i.e.: tracks efficiency, cluster size.

To be able to operate with irradiated devices, a cooling system was implemented. In order to isolate the DUTs at a low temperature and shield them from the light which comes from the environment, the so called Dortmund cooling box was used. Thanks to this system it is possible to reach almost -50° C, a temperature lower than the IBL working temperature. As Figure 6.3 shows, the cooling box is basically splitted in two compartments: one for the DUTs, and another one for the dry-ice. These have been separated so that when the dry-ice evaporates, it is possible to make a refill without touching the DUTs. On the DUT side, the SCC boards are attached to the so called L-mount, in order for the devices to be aligned or tilted. In fact, the L-mount is either screwed directly to an aluminum base plate on the cooling box or to a wedge, to tilt the devices under test in the ϕ direction. The plate is also dotted with rotation spacers to tilt the assembly in

---

[3] With maximum particle intensity 2×10^8 particles per spill.

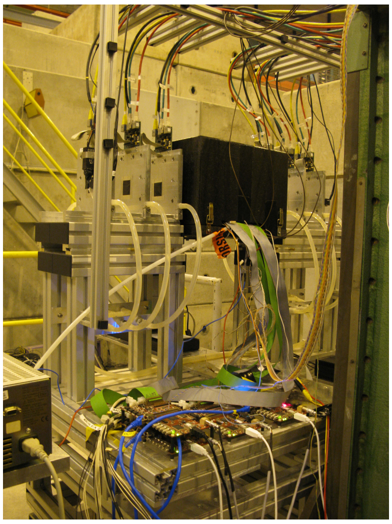

Figure 6.2: Layout of the 3D and planar samples at 0° during an IBL beam test (September 2011).

the η direction, in order to simulate the outer most parts of the IBL. In fact, the aim of the September IBL beam test was to study the behavior of the samples at large η (the results obtained are not reported here because are still under investigations). On the DUT side the box is flushed with nitrogen or dry air to avoid condensation on the electronics which could cause malfunctions or, even worst, short circuits.

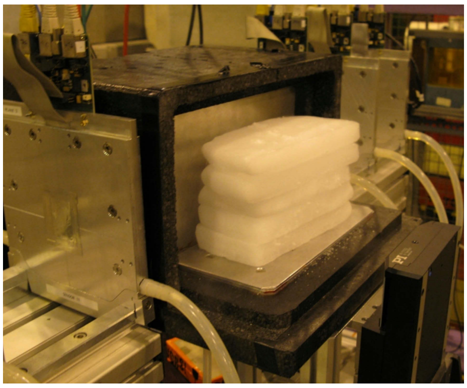

Figure 6.3: Detail of the Dortmund Cooling Box with dry-ice. The closed black part is where the samples under test are mounted.

6.2 Devices Under Test and Run Plan

Two 3D-FBK sensors were used as devices under test for the June beam test, for a total of 10 DUTs, and two for the September beam test period for a total of 9 DUTs[4]. For the June beam test there were two irradiated 3D devices. The beam

---

[4] Plus one planar sensor for each period as sensor reference.

test aim was to test sensors having the IBL-type design under IBL conditions (angle, field, temperature) with the focus to provide results for the Sensor Review. For this reasons the FBK11 proton-irradiated sensor has been tested up to 5×10^{15} n_{eq}/cm^2 (IBL fluency) and as well the FBK09 proton irradiated up to 2×10^{15} n_{eq}/cm^2. The September beam test instead, was planed to study the sensor behavior at large η. For this purpose FBK11 and the un-irradiated FBK13 sensors were tested. As already mentioned in Section 4.6, all the three sensors belong to the same layout design and wafer batch called ATLAS09. The complete list of the planar and 3D devices, CNM and FBK, under test which have been used during tho two periods is available at the referred wikipage [92].

Due to the large number of samples to be tested, the beam test period was divided in several batches, to be able to compare the results under the same environment and setup conditions (ϕ angle, η, cooling temperature etc.). Table 6.1 summarizes the batch number where the 3D-FBK sensors which were tested, the tilt angle with respect to the beam direction (along z) and the power (HV) supplied to each sensors. In addiction, the Table presents the configuration information since it must be stressed that the sensor's performance strongly depend on the configuration settings. In fact, as for the planar sensors, the 3D samples were tested and tuned few days before the beam test at CERN in laboratory. In June tests both FBK devices were tuned at 3200 electrons, at eight TOT for a deposit charge of 20000 electrons, while in September two configuration have been used: 1500 for FBK13 and 2000 electrons for FBK11. To be more precise, due to the different setups, cables, environments and power supplies (including differrent lengths of the power supply cables) it was find out that the tuning done in the laboratory was different from the expected configuration at the beam test area. At the beginning the problem did not show up, due to leak of time needed for the debugging of the system. Later, during a beam-stop, the problem was spotted and all the sample were retuned with a fast procedure[5]. This is why, as shown in Table 6.1 the threshold was set at 3100 and 2400 electrons (different values from the ones used in the laboratory tests).

Thanks to the experience learned in June, in September a specific time was allocate to check the configuration and in the worst case to tune again the devices under test. As mentioned above, for the irradiated devices a L-aluminum plate was applied to increase the efficiency of the cooling system. Figure 6.4 shows the L-mount for the FBK11 (front view) and the L-aluminum plate (back side). To keep under control the temperature, a NTC PT1000[6] was glued to the aluminum on the front side of the SCC as close as possible to the sensors and Frond-End without taking the risk to damage them. A transparent glass was left mounted on the front to protect the sensor itself and the wire bonding from possible accidental damages during the assembly.

---

[5] No time to reach the wanted tuning targets, and it has been accepted not perfect tunings.

[6] Thermal sensors for high-precision temperature measurement.

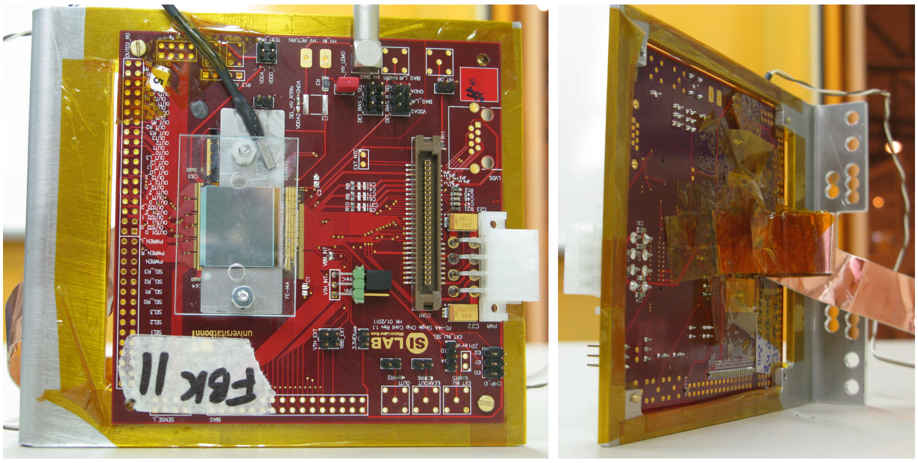

Figure 6.4: FBK11 sensor at the beam test: front and back view.

6.3 Results

The data taken during the two periods of test beam were reconstructed using the EUDET reconstruction package[7]. Then the data obtained were saved as root file [93], in a format that the so called *tbmon* software package is able to process for the further analysis. Tbmon is a program software, based on C^{++}, born, developed and grown inside the 3D community. Later it was officially chosen by the sensors communities to be the official program to use to provide in a standard way the analysis.

The data collection was split into runs which typically have the size of 100k accepted triggers. The length of a run varying and depends on the beam characteristic (especially intensity). Only the triggers related to a particle that pass throughout all the telescope planes are used for the track reconstruction. Moreover only the track that pass through the DUT are used for the analysis. In the next following sections it is will be explain the results obtained during the beam test, in terms of tracking efficiency and cluster size.

6.3.1 Tracking Efficiency

The tracking efficiency is calculate using tracks reconstructed with the telescope and extrapolated to the DUT where matching hits are checked for. Knowing that the integration time of the telescope is different from the read out time of the USBPpix system (from the DUTs), it is defined an expected hit as a hit that was detected by the telescope (through all the six telescope planes). In order to remove possible biases due the edge effect, only the central part of the sensor have been considered. In addiction, to be identify as an hit, in order to remove fake tracks (example noise), a hit in (any[8]) other device is required. The efficiency therefore is defined as the ratio between the total number of tracks and the tracks with an associated cluster:

---

[7] By Matthias George, Igor Rubinsky and Sh. Tsiskaridze.

[8] At least one.

$$Efficiency = \frac{\text{Number of track with associated cluster}}{\text{Number of Total Tracks}} \tag{6.1}$$

The definition request at least one match hit on any other DUTs and the tracks with associated cluster has to match. Noise and dead pixels are not taken into account since they are masked out from analysis. In all the configurations all the FE-I4 channels were abled. This is particular important for irradiated sensors where the active area could be limited by the dead Front-End channels. In general, the efficiency depends on:

(i) the angle incidence of the detector respect to the track particle incidence

(ii) the particle realize a certain amount of charge in the active sensors area

(iii) the effective active area depends on the electric field on the substrate

(iv) the charge collected is above the threshold set on the Front-End

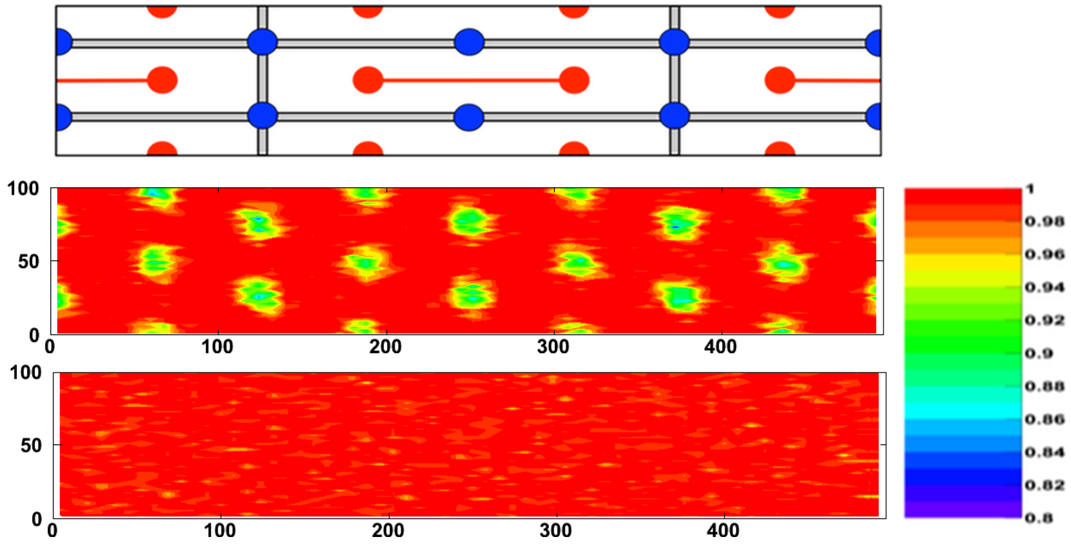

Figure 6.5: From the top: (a) mask detail centered on one cell and extending to half a cell in both directions; two-dimensional efficiency map for un-irradiated FBK13: (b) at 0°; (c) at 15°. Both configurations tuned at 1500 e^-, at eight TOT, see Table 6.1.

The angle incidence influences the efficiency in particular for the 3D sensors. In fact, as it will show later, in the 3D sensors a hit that goes all the way through the electrode is not collected: the electrodes does not belong to the active area of the sensors because there is no electric field there. On the contrary, if a particle realize not enough charge that is able to pass the threshold cut (of the preamplifier of the Front-End), no hit is readout by the Front-End. In addiction, the active area depends where the electric field is present and on its intensity. For the

3D sensors the electric field between the columns is crucial: higher is the electric field, higher has to be the bias voltage applied to the sensor. Therefore, acting on the threshold tuning and on the bias voltages the efficiency change.

Several sensors configuration were used to study the charge collection of the sensors under tests, previously tuned in the laboratories. An overview of the results from the different beam test is summarized in Table 6.1.
The FBK13 is an example of 3D-FBK un-irradiated. At 0° the efficiency is around 98.8%, while at a tilted angle of 15° it reaches 99.4%. As said before, this was expected: the efficiency loss at normal incidence is due to the less charge collected in the electrodes. As Figure 6.5 (b) reports, the efficiency is lower when the tracks pass near or through the 3D clomuns causing a lower charge collected (no electric field is present - the columns are empty). In fact, for 3D devices the electrodes are considered as dead regions and do not collect charge. On the contrary, at 15° the efficiency is fully recovered: the tracking path length inside the electrodes is significantly reduced and therefore the dead area is decreased. It must be stressed that the efficiency values obtained is related to the threshold used: usually a higher threshold is used for testing the devices (i.e. in the laboratory at 3200 electrons). In this case, the threshold for FBK13 was equal to 1500 electrons and thanks to this a few percent of efficiency was gained. In principle, the threshold should be as lower as possible to increase the charge collection and the efficiency. Comparing the Front-End FE-I4 to the previous version FE-I3 is possible to reach very lower thresholds, almost around 500 electrodes. On the contrary, lower threshold values give a higher noise. The threshold set to 1500 electrodes allows a good compromise and safety margin to ensure low noise levels. This is emphasized for the irradiated sensors, which have a higher noise (as reporter in Chapter 5 Section 5.4.3). Figure 6.6 shows the efficiency map for the FBK11 tested at 15°. To study the effect of the threshold on the efficiency, two threshold settings have been used: 2400 electrons[9] and 2000 electrons. This had the effect to increase (a very few percentage) the efficiency, passing from 95.3% to 95.6%[10]. In addiction, for the configuration of 2000 electrons, it was applied a higher bias voltage to have a higher electric field between the electrodes. Figure 6.6 (d) shows the efficiency of another irradiated sample: the FBK09 irradiated to $2 \times 10^{15}\,\mathrm{n}_{eq}/\mathrm{cm}^2$, at 15°. The lower irradiation is clearly visible: the efficiency map does not show the lower efficiency around the electrodes (compared to the FBK11 case, the electrodes are not visible) and the efficiency is 99.8%.

6.3.2 Cluster Size

When a particle pass throughout the sensor thanks to the ionization process it realizes charge (free charge carries) in the silicon, that, under the electric field, are collected at the electrodes (already explained in Chapter 1 Section 1.3). In

---

[9] The unusual threshold value is due to the different tuning from the laboratory and the beam test area.

[10] It has to underline that with the proton irradiation, the Front-End suffers a lot. Therefore, it is difficult to assign the cause of the not complete efficiency: if it is related to the sensors itself or either (but more probably) to the dead channels of the Front-End.

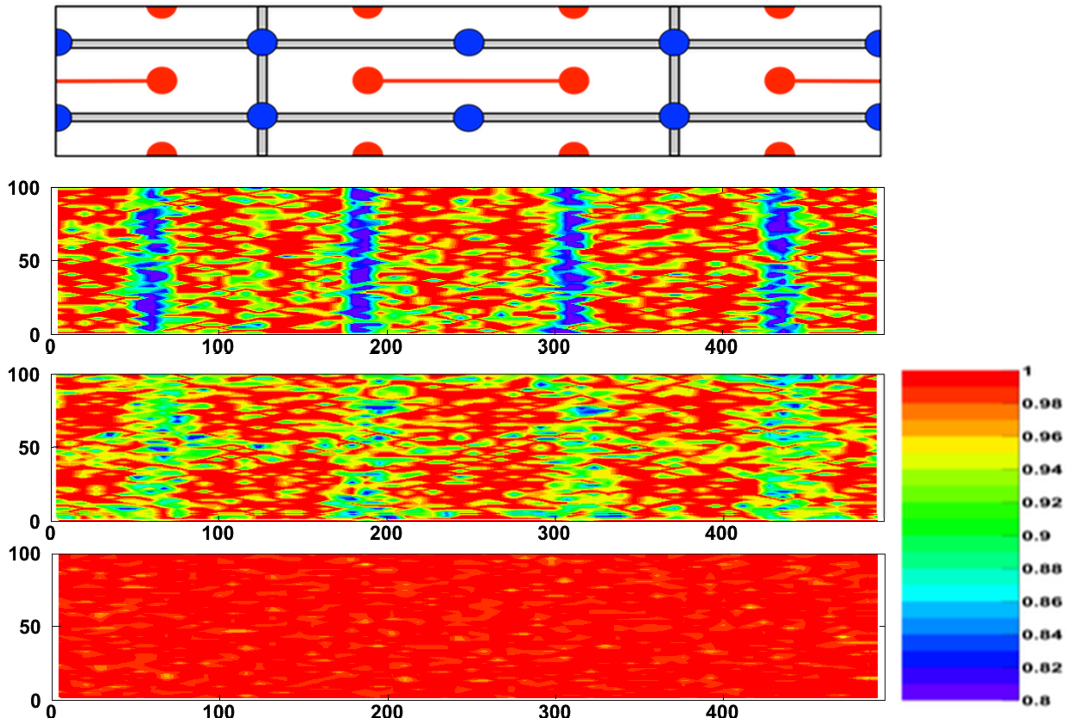

Figure 6.6: Efficiency maps reconstructed from the Eudet data for the 3D sensors after proton irradiation. From the top: (a) mask detail centered on one cell and extending to half a cell in both directions; two-dimensional efficiency map for proton-irradiated FBK11 ($5\times10^{15}\,\mathrm{n}_{eq}/\mathrm{cm}^2$) at 15° with threshold equal to: (b) 2400 e^-, (c) 2000 e^-. (d) Proton-irradiated FBK09 ($2\times10^{15}\,\mathrm{n}_{eq}/\mathrm{cm}^2$) at 15° with threshold equal to 3100 e^-.

most of the cases, more than one readout electrode collects the free charge carries, see Figure 4.2. Depending on the pixel sensor design, threshold, bias voltages, hit position and track angle there is a certain probability that a m.i.p. will active more than one pixel channel to collect the charge above the threshold. Due to these effects, instead of considering single pixel hits, it is preferable to use cluster of pixel with hits. 'Clusters of pixel' are simply defined as neighboring pixels which detect hits: if a pixel has a hit is added to the cluster, then only the neighboring pixels fired with a hit are added into the same cluster. Therefore a cluster contain only pixels in the proximity of the track to avoid noise sources.
Figure 6.9 and Figure 6.10 shows the cluster size of the FBK13 and FBK11 at the beam tests at the four different settings. Main data are also summarized in Table 6.2. The mean cluster size at normal incidence is a bit more than one and half (depending on the setting, setups, multiple scattering), while increasing the tilt angle, due to the inclination of the track, the mean cluster size is around 2-2.5.
Table 6.2 summarized as well the mean cluster charge collected (in TOT units[11]) for the two sensors during the two beam tests, (results also shown in Figure 6.7 and Figure 6.8). The Table confirm what already explained in the previous Section 6.3.1. The signal charge for the un-irradiated FBK13 at 15° is higher

---

[11] Once again, no TOT to charge is available.

Sensor	Beam Test	Batch	Fluence [n_{eq}/cm^2]	HV [V]	Threshold [e^-]	ϕ	Hit efficiency [%]
FBK09	June	4	2×10^{15}	60	3100	15	99.8
FBK11	June	3	5×10^{15}	140	2400	15	95.3
	Sept	1		160	2000	15	95.6
FBK13	Sept	4	-	20	1500	0	98.8
	Sept	6	-	20	1500	15	99.4

Table 6.1: 3D-FBK devices under test in June and September 2011 beam test.

than at 0° in according with the increased mean cluster size (2.52) and efficiency (99.4%). For the proton irradiated FBK11 the signal charge is higher increasing the bias voltage (from 140 V to 160 V) and decreasing the threshold (from 2400 to 2000 electrons): mean cluster charge of 8.56 for an efficiency of 95.6% with a cluster size of 2.21.

Sensor	Fluence [n_{eq}/cm^2]	HV [V]	Threshold [e^-]	ϕ	Mean cluster charge	Mean cluster size
FBK11	5×10^{15}	140	2400	15°	5.5	1.94
		160	2000	15°	8.56	2.21
FBK13	-	20	1500	0°	9.4	1.71
	-	20	1500	15°	11.1	2.52

Table 6.2: The average cluster charge and size are summarized for FBK13 and FBK11.

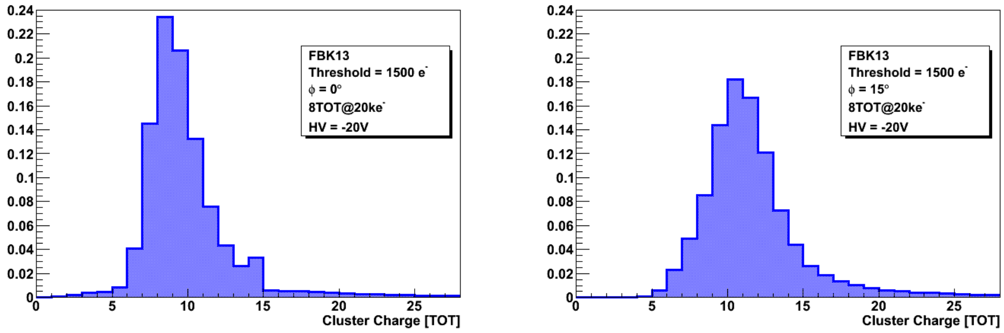

Figure 6.7: Cluster charge in TOT units for FBK13: (left) at 0°and (right) at 15°.

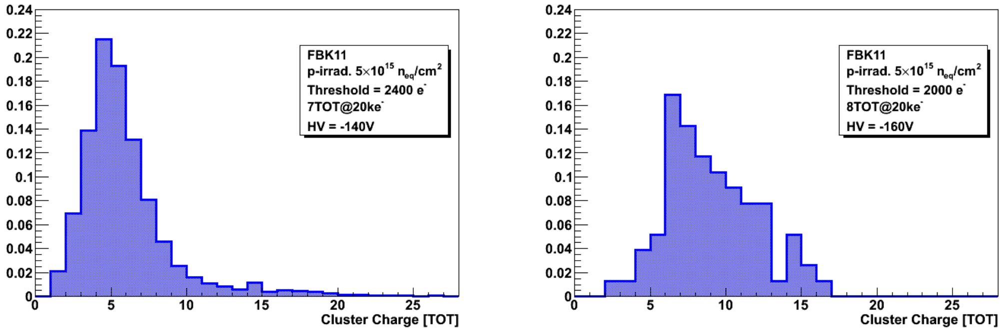

Figure 6.8: Cluster charge in TOT units for FBK11 proton irradiated ($5 \times 10^{15}\, \mathrm{n}_{eq}/\mathrm{cm}^2$, at 15°) at different thresholds and bias voltage: (left) 2400 e$^-$ at -140V, (right) 2000 e$^-$ at -160V.

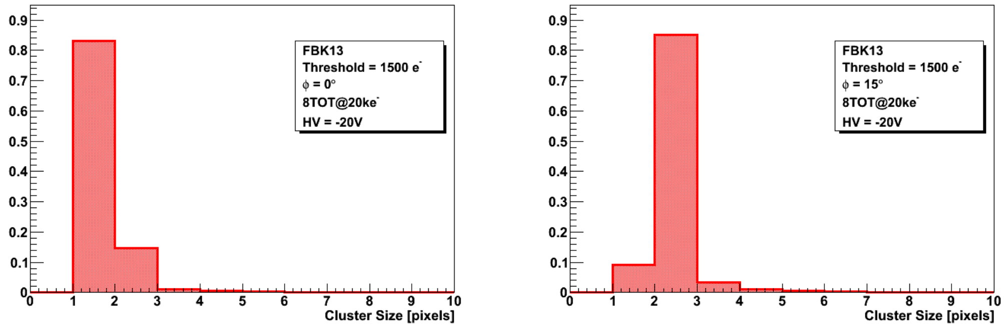

Figure 6.9: Cluster size for FBK13: (left) at 0°and (right) at 15°.

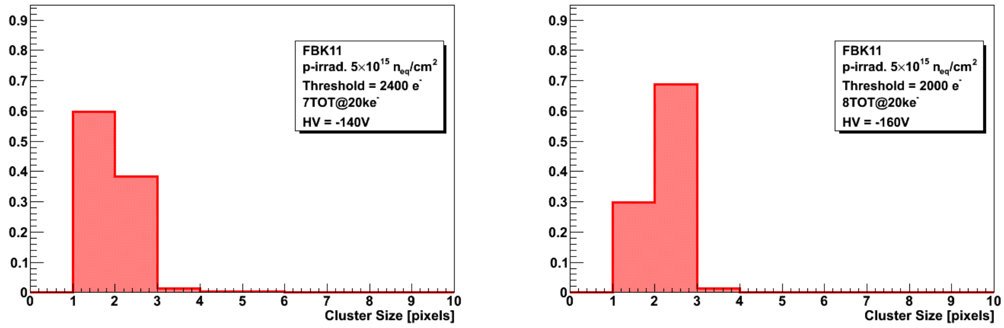

Figure 6.10: Cluster size for FBK11 proton irradiated ($5 \times 10^{15}\, \mathrm{n}_{eq}/\mathrm{cm}^2$, at 15°) at different thresholds and bias voltage: (left) 2400 e$^-$ at -140V, (right) 2000 e$^-$ at -160V.

Chapter 7

Conclusions

In this thesis, the 3D sensors developed for the ATLAS Pixel Detector upgrade project (Insertable B-layer or IBL) have been presented. Their particular characteristics have been described, together with the performance of some of the prototypes produced by FBK. After three years of research a lot of work have been done, exspecially during the last year, when the last batch, the so called ATLAS09 (fabricated in Trento), was produced. In fact, it has been chosen to report here the result from this batch only. However, to be able to arrive to this 'state of the art' a lot of analysis has been done in the past. In fact, only the batch ATLAS09 have the new Front-End chip bump-bonded on the 3D-FBK sensors, the FE-I4 (the Front-End which will be used for the IBL).

During the last year enough studies have been performed, to complete the understanding of the full 3D technology (with full passing through columns), and its behavior together with the Front-End.

The 3D sensor performances have been studied in laboratory, where the electrical and source (charge collection) measurements have been done, as well as in beam tests periods. This PhD project has been mainly focused on the laboratory characterization but keeping a strong relationship whit the beam test studies and analysis. Without the laboratory tests no sensors pre-selection or study criteria would have been possible. In fact, along the years, these studies helped the sensor developers to better understand the new 3D technology.

The studies reported here could be divided in three phases: the first one to study the Front-End chip response, the second one, to study the sensors behavior and the third and last one to study the combination of the two. Certainly the third phase has been the most complex one since, to improve the performance, one has to have clear in mind the other two. For the future, more studies could be planned (some of them are already): after sample irradiation (proton and neutron), to better understand the radiation hardness features, the charge collection (using propers sources) and comparing the FBK and CNM layout technology, are only few examples.

The results of my work, together with other studies from the ATLAS 3D sensors community, were presented at the ATLAS Sensor Review to prove the good performance of the 3D technology and were useful to show to the experts that the 3D technology was finally ready to be used inside the Pixel Detectors.

Here are reported the highlights from the 3D sensors review:

"[...] There has been significant progress in the production of 3D wafers and a yield of around 50% has been achieved for a relatively small number of wafers. [...] The Panel notes that there is an opportunity to use the 3D technology to populate the forward region where the tracking could take advantage of the electrode orientation to give a better z-resolution after heavy irradiation. The IBL should proceed to full production of the planar sensors required to build 100% of the IBL, and the current production of 3D should be completed (3 batches from each of CNM and FBK). If the yield is sufficient, then up to 50% of the modules (in the forward regions) can be made using 3D sensors."

At the end, the planar and 3D communities agreed to have a 25% of 3D sensors on the outermost part of IBL. Therefore, thanks to my work and contribution inside the 3D community, the 3D sensors will be used for the IBL project. This will be the first time ever that the 3D sensors technology will be used inside a pixel detector for high energy physics. A new interesting scenario just started.

Bibliography

[1] G. Lutz, *Semiconductor Radiation Detectors, Devices Physics, Springer*, 2nd ed., Spinger, Ed. Springer, 1999.

[2] L. Rossi et al., *Pixel Detectors: From Fundamentals to Applications (Particle Acceleration and Detection).* Springer, Mar. 2006.

[3] R. C. Alig et al., "Struck scattering by ionization and photon emission in semiconductors," *Nuclear Physics B*, vol. B22, no. 0, p. 5565, 1980. [Online]. Available: http://www.ba.infn.it/~mazziot/phyrevb22_5565.pdf

[4] S. Ramo, "Currents Induced by Electron Motion," *Proceedings of the IRE*, vol. 27, no. 9, pp. 584 – 585, Sept. 1939.

[5] H. Bichsel, "Straggling in thin silicon detectors," *Rev. Mod. Phys.*, vol. 60, pp. 663–699, Jul 1988. [Online]. Available: http://link.aps.org/doi/10.1103/RevModPhys.60.663

[6] J.F. Bak et al., "Large departures from Landau distributions for high-energy particles traversing thin Si and Ge targets," *Nuclear Physics B*, vol. 288, no. 0, pp. 681 – 716, 1987. [Online]. Available: http://www.sciencedirect.com/science/article/pii/0550321387902343

[7] D. A. Dobos, "Commissioning Perspectives for the ATLAS Pixel Detector," Ph.D. dissertation, Univ. Dortmund, Dortmund, 2007, presented on 1 Sep. 2007.

[8] The ATLAS Collaboration, "ATLAS pixel detector electronics and sensors," *Journal of Instrumentation*, vol. 3, no. 07, p. P07007, 2008. [Online]. Available: http://stacks.iop.org/1748-0221/3/i=07/a=P07007

[9] J. M. et al., "Technology development for SOI monolithic pixel detectors," *Nuclear Instruments and Methods in Physics Research Section A: Accelerators, Spectrometers, Detectors and Associated Equipment*, vol. 560, no. 1, pp. 26 – 30, 2006, proceedings of the 13th International Workshop on Vertex Detectors VERTEX 2004. [Online]. Available: http://www.sciencedirect.com/science/article/pii/S0168900205023284

[10] A. Micelli et al., "3D-FBK pixel sensors: Recent beam tests results with irradiated devices," *Nuclear Instruments and Methods*

in Physics Research Section A: Accelerators, Spectrometers, Detectors and Associated Equipment, vol. 650, no. 1, pp. 150 – 157, 2011, <ce:title>International Workshop on Semiconductor Pixel Detectors for Particles and Imaging 2010</ce:title>. [Online]. Available: http://www.sciencedirect.com/science/article/pii/S0168900210030111

[11] G. Lindstr*öm* et al., "Radiation hardness of silicon detectors - a challenge from high-energy physics," *Nuclear Instruments and Methods in Physics Research Section A: Accelerators, Spectrometers, Detectors and Associated Equipment*, vol. 426, no. 1, pp. 1 – 15, 1999. [Online]. Available: http://www.sciencedirect.com/science/article/pii/S0168900298014624

[12] M. Moll, "Radiation damage in silicon particle detectors: microscopic defects and macroscopic properties. oai:cds.cern.ch:425274," Ph.D. dissertation, Hamburg Univ., Hamburg, 1999, presented on 30 Nov 1999.

[13] ——, "Radiation Tolerant Sensors for Solid State Tracking Detectors," 2008, lHC and Beyond - Research Training Course in Detector Technology, Helsinki Institute of Physics, Helsinki , December 2. [Online]. Available: http://indico.cern.ch/getFile.py/access?resId=0&materialId=0&confId=46820

[14] C. Piemonte, "Device simulations of isolation techniques for silicon microstrip detectors made on p-type substrates," *Nuclear Science, IEEE Transactions on*, vol. 53, no. 3, pp. 1694 – 1705, June 2006.

[15] I Gorelov et al., "Electrical characteristics of silicon pixel detectors," *Nuclear Instruments and Methods in Physics Research Section A: Accelerators, Spectrometers, Detectors and Associated Equipment*, vol. 489, no. 1-3, pp. 202 – 217, 2002. [Online]. Available: http://www.sciencedirect.com/science/article/pii/S0168900202005570

[16] A. Zoboli, "Development of radiation detectors with three-dimensional electrodes for future high energy physics experiments," Ph.D. dissertation, DISI - Universit'a degli Studi di Trento, Trento, March 2009.

[17] F. Hirsch, "Online-Monitoring of the Atlas-Pixel-Detector," Master's thesis, Technische Universit'́at Dortmund Experimentelle Physik IV, 44221 Dortmund Germany, Otto-Hahn-Str. 4, Zufahrt Nr. 29, 2007.

[18] Marco Olcese, "ATL-IP-EP-0004, Pixel Detector Active Area Layout," CERN, Geneva, Tech. Rep. CERN-LHCC-2010-013. ATLAS-TDR-019, aug 2004. [Online]. Available: https://edms.cern.ch/document/107600/7

[19] The ATLAS Collaboration, "The ATLAS Experiment at the CERN Large Hadron Collider," *Journal of Instrumentation*, vol. 3, no. 08, p. S08003, 2008. [Online]. Available: http://stacks.iop.org/1748-0221/3/i=08/a=S08003

[20] Ivan Perić et al., "The FEI3 readout chip for the ATLAS pixel detector," *Nuclear Instruments and Methods in Physics Research Section A: Accelerators, Spectrometers, Detectors and Associated Equipment*, vol.

565, no. 1, pp. 178 – 187, 2006, proceedings of the International Workshop on Semiconductor Pixel Detectors for Particles and Imaging PIXEL 2005, International Workshop on Semiconductor Pixel Detectors for Particles and Imaging. [Online]. Available: http://www.sciencedirect.com/science/article/pii/S0168900206007649

[21] K. Einsweiler, "ATLAS On-detector Electronics Architecture," 2003, lBNL, Draft V3.0, 12.9.2003. [Online]. Available: http://icwiki.physik.uni-bonn.de/twiki/pub/Systems/WebHome/ATLASPixelFEChip_v3_0.pdf

[22] ——, "FE-I3 and MCC Documentation," 2011, information on the FE-I3 chip and module controller chip MCC 2.1. [Online]. Available: http://icwiki.physik.uni-bonn.de/twiki/bin/view/Systems/UsbPix#FE_I3_and_MCC_Documentation

[23] R. Beccherle, "The module controller chip (MCC) of the ATLAS pixel detector," in *Nuclear Science Symposium, 1998. Conference Record. 1998 IEEE*, vol. 1, 1998, pp. 69 –74 vol.1.

[24] Capeans, M et al., "ATLAS Insertable B-Layer Technical Design Report," CERN, Geneva, Tech. Rep. CERN-LHCC-2010-013. ATLAS-TDR-019, Sep 2010. [Online]. Available: http://cdsweb.cern.ch/record/1291633

[25] Nessi, M., "ATLAS Upgrade Report," CERN, Tech. Rep., 06 2011-Dec. 6 2011. [Online]. Available: https://indico.cern.ch/getFile.py/access?contribId=2&resId=0&materialId=slides&confId=164301

[26] C. Gemme, "The ATLAS insertable B-Layer (IBL) project," CERN, Geneva, Tech. Rep. ATL-INDET-PROC-2011-018, Sep 2011.

[27] M. Garcia-Sciveres et al., "The FE-I4 Pixel Readout Integrated Circuit," CERN, Geneva, Tech. Rep. ATL-UPGRADE-PROC-2010-001, Jan 2010.

[28] "FE-I4 summary," 05.04.2011, fE-I4 course - DESY. [Online]. Available: https://indico.cern.ch/getFile.py/access?contribId=4&resId=1&materialId=slides&confId=133174

[29] "S. Strandberg et al., pixel detector group wiki."

[30] C. Kenney et al., "Comparison of 3D and planar silicon detectors," in *Proc. 9th Meeting Div. Particles and Fields Amer. Phys. Soc.*, vol. 2, 1996, pp. 1342 – 1345.

[31] FE-I4 Collaboration, "The FE-I4 Integrated Circuit Guide," June 2011, Detailed reference of the FE-I4 integrated circuit.

[32] A. Vasilescu and G. Lindstroem, "Notes on the fluence normalisation based on the NIEL scaling hypothesis," June 2000, the ROSE Collaboration. Technical Note ROSE/TN/2000-02, CERN. [Online]. Available: http://rd48.web.cern.ch/rd48/technical-notes/rosetn00-02.ps

[33] M. A. et al., "The ATLAS silicon pixel sensors," *Nuclear Instruments and Methods in Physics Research Section A: Accelerators, Spectrometers, Detectors and Associated Equipment*, vol. 456, no. 3, pp. 217 – 232, 2001. [Online]. Available: http://www.sciencedirect.com/science/article/pii/S016890020000574X

[34] J. Jentzsch, "Characterization of Planar n^+-in-n ATLAS FE-I4 Single Chip Assemblies in Laboratory and Testbeam Measurements," Master's thesis, Technische Universit´at Dortmund Experimentelle Physik IV, 44221 Dortmund Germany, Otto-Hahn-Str. 4, Zufahrt Nr. 29, 2011, diploma Thesis. [Online]. Available: http://e4.physik.tu-dortmund.de/~jentzsch/diplom_jjentzsch.pdf

[35] S. Grinstein, "Overview of Silicon Pixel Sensor Development for the ATLAS Insertable B-Layer (IBL)," CERN, Geneva, Tech. Rep. ATL-INDET-PROC-2011-042, Dec 2011. [Online]. Available: https://cdsweb.cern.ch/record/1392925

[36] "CiS, Erfurt (Germany)." [Online]. Available: http://www.cismst.orgi/en/.

[37] J.J. Velthuis et al., "Radiation hard diamond pixel detectors," *Nuclear Instruments and Methods in Physics Research Section A: Accelerators, Spectrometers, Detectors and Associated Equipment*, vol. 591, no. 1, pp. 221 – 223, 2008, <ce:title>Radiation Imaging Detectors 2007</ce:title> <ce:subtitle>Proceedings of the 9th International Workshop on Radiation Imaging Detectors</ce:subtitle>. [Online]. Available: http://www.sciencedirect.com/science/article/pii/S0168900208004427

[38] C. Ilgner, "Implementation of a diamond-beam-conditions monitor into the LHCb experiment at CERN," in *Nuclear Science Symposium Conference Record, 2007. NSS '07. IEEE*, vol. 2, 26 Nov. 2007, pp. 1700 –1704.

[39] F. Rivero, "Charaterization of FBK-irst 3D Double Side Double Type Column Silicon Sensor," Master's thesis, DISI - Universit'a degli Studi di Trento, Trento, 2008-2009.

[40] C. Da Vià et. al., "3-D active edge silicon sensor test results," 2006, presented at the Sixth International"Hiroshima" Symposium on the Development and Application of Semiconductor Tracking Detectors, Carmel Mission Inn, California.

[41] A. Meikle et. al., "3-D GaAs radiation detectors," 1999, proc. of the 5th Int. Conf. on Position-Sensitive Detectors, London, U.K., 1999.

[42] Parker, S.I. et al., "Performance of 3-D architecture silicon sensors after intense proton irradiation," *Nuclear Science, IEEE Transactions on*, vol. 48, no. 5, pp. 1629 –1638, Oct. 2001.

[43] C. DaVia and S. Watts, "The geometrical dependence of radiation hardness in planar and 3D silicon detectors," *Nuclear Instruments and Methods in Physics Research Section A: Accelerators, Spectrometers, Detectors and Associated Equipment*, vol. 603, no. 3, pp. 319 – 324, 2009. [Online]. Available: http://www.sciencedirect.com/science/article/pii/S0168900209003994

[44] Kenney, C.J. et al., "Results from 3-D silicon sensors with wall electrodes: near-cell-edge sensitivity measurements as a preview of active-edge sensors," *Nuclear Science, IEEE Transactions on*, vol. 48, no. 6, pp. 2405 –2410, Dec 2001.

[45] Betta, G.D. et al., "Development of Active and Slim Edge Terminations for 3D and Planar Detectors," in *Nuclear Science Symposium Conference Record (NSS/MIC), 2011 IEEE*, 2011.

[46] C. Da Vià, "3D Silicon Detectors for High Energy Physics and Medical Applications," 2009, workshop, Cosenza, 7th May (2009). [Online]. Available: http://www.cs.infn.it/da_via.pdf

[47] Metcalfe, J.E. et al., "Capacitance Simulations and Measurements of 3D Pixel Sensors Under 55 MeV Proton Exposure," *Nuclear Science, IEEE Transactions on*, vol. 55, no. 5, pp. 2679 –2684, Oct. 2008.

[48] chaired by K. Tokushuku, "IBL Sensor Review," July 2011, cERN, 4th-5th.

[49] S.I. Parker et al., "3D - A proposed new architecture for solid-state radiation detectors," *Nuclear Instruments and Methods in Physics Research Section A: Accelerators, Spectrometers, Detectors and Associated Equipment*, vol. 395, no. 3, pp. 328 – 343, 1997, proceedings of the Third International Workshop on Semiconductor Pixel Detectors for Particles and X-rays. [Online]. Available: http://www.sciencedirect.com/science/article/pii/S0168900297006943

[50] Kenney, C. et al., "Silicon detectors with 3-D electrode arrays: fabrication and initial test results," *Nuclear Science, IEEE Transactions on*, vol. 46, no. 4, pp. 1224 –1236, aug 1999.

[51] "Sintef, Oslo, Norway." [Online]. Available: http://www.sintef.no

[52] C. Piemonte et al., "Development of 3D detectors featuring columnar electrodes of the same doping type," *Nuclear Instruments and Methods in Physics Research Section A: Accelerators, Spectrometers, Detectors and Associated Equipment*, vol. 541, no. 1-2, pp. 441 – 448, 2005, development and Application of Semiconductor Tracking Detectors Proceedings of the 5th International Symposium on Development and Application of Semiconductor Tracking Detectors (STD 5) Development and Application of Semiconductor Tracking Detectors. [Online]. Available: http://www.sciencedirect.com/science/article/pii/S0168900205001853

[53] Eranen, S. et al., “Silicon semi 3D radiation detectors,” in *Nuclear Science Symposium Conference Record, 2004 IEEE*, vol. 2, Oct. 2004, pp. 1231 – 1235 Vol. 2.

[54] “Technical Research Center of Finland (VTT), Information Technology Microelectronics, PO Box 1208, FIN-02044 VTT, Finland.”

[55] Lukas Tlustos et al., “Characterisation of a semi 3-D sensor coupled to Medipix2,” *Nuclear Instruments and Methods in Physics Research Section A: Accelerators, Spectrometers, Detectors and Associated Equipment*, vol. 580, no. 2, pp. 897 – 901, 2007, imaging 2006 Proceedings of the 3rd International Conference on Imaging Techniques in Subatomic Physics, Astrophysics, Medicine, Biology and Industry. [Online]. Available: http://www.sciencedirect.com/science/article/pii/S0168900207012855

[56] J. Kalliopuska, “Edgeless detector fabrication on 6 “soi-wafers at vtt”, presented at the 4th trento workshop on advanced silicon radiation detectors (3d and p-type technologies,” 2009, fBK - irst, Trento, Italy, Feb. 2009.

[57] Z. Li et al., “Development, simulation and processing of new 3D Si detectors,” *Nuclear Instruments and Methods in Physics Research Section A: Accelerators, Spectrometers, Detectors and Associated Equipment*, vol. 583, no. 1, pp. 139 – 148, 2007, proceedings of the 6th International Conference on Radiation Effects on Semiconductor Materials, Detectors and Devices RESMDD 2006. [Online]. Available: http://www.sciencedirect.com/science/article/pii/S016890020701916X

[58] Li, Z. et al., “Development of New 3d Si Detectors at BNL and CNM,” in *Nuclear Science Symposium Conference Record, 2006. IEEE*, vol. 3, 29 Nov. 2006, pp. 1445 –1451.

[59] G. Pellegrini et al., “First double-sided 3-D detectors fabricated at CNM-IMB,” *Nuclear Instruments and Methods in Physics Research Section A: Accelerators, Spectrometers, Detectors and Associated Equipment*, vol. 592, no. 1-2, pp. 38 – 43, 2008. [Online]. Available: http://www.sciencedirect.com/science/article/pii/S0168900208004828

[60] Dalla Betta, G.-F. et al., “New developments on 3D detectors at IRST,” in *Nuclear Science Symposium Conference Record, 2007. NSS ’07. IEEE*, vol. 2, 26 Nov. 2007, pp. 983 –987.

[61] “Stanford Nanofabrication Facility.” [Online]. Available: http://snf.stanford.edu

[62] “Centro National de Microelectrónica (CNM-IMB-CSIC), Campus Universidad Autónoma de Barcelona, 08193 Bellaterra, (Barelona), Spain.” [Online]. Available: http://www.imb-cnm.csic.es

[63] “Fondazione Bruno Kessler (FBK),” Via Sommarive 18, 38123 Povo Trento, Italy. [Online]. Available: http://www.fbk.eu/

[64] Parkes, C P et al., “3D detectors. Recent trends in 3D Detectors,” *PoS*, vol. VERTEX 2008, p. 039, 2008.

[65] A A Ayón et al., “Deep reactive ion etching: a promising technology for micro- and nanosatellites,” *Smart Materials and Structures*, vol. 10, no. 6, p. 1135, 2001. [Online]. Available: http://stacks.iop.org/0964-1726/10/i=6/a=302

[66] Betta, G.D. et al., “Development of modified 3D detectors at FBK,” in *Nuclear Science Symposium Conference Record (NSS/MIC), 2010 IEEE*, 30 Nov. 2010, pp. 382–387. [Online]. Available: http://ieeexplore.ieee.org/xpl/freeabs_all.jsp?arnumber=5873785

[67] A. Zoboli et al., “Double-Sided, Double-Type-Column 3-D Detectors: Design, Fabrication, and Technology Evaluation,” *Nuclear Science, IEEE Transactions on*, vol. 55, no. 5, pp. 2775 –2784, Oct. 2008.

[68] G. and Kramberger, “Recent results from CERN RD50 collaboration,” *Nuclear Instruments and Methods in Physics Research Section A: Accelerators, Spectrometers, Detectors and Associated Equipment*, vol. 583, no. 1, pp. 49 – 57, 2007, proceedings of the 6th International Conference on Radiation Effects on Semiconductor Materials, Detectors and Devices RESMDD 2006. [Online]. Available: http://www.sciencedirect.com/science/article/pii/S0168900207019134

[69] C. Da Vià, “Progress with 3D detectors for the IBL,” 2012. [Online]. Available: https://indico.cern.ch/getFile.py/access?contribId=1&sessionId=3&resId=0&materialId=slides&confId=161493

[70] M Povoli et al., “Slim edges in double-sided silicon 3D detectors,” *iWoRID2011, Zürich Switzerland*, Jul. 2011.

[71] “Medipix.” [Online]. Available: http://medipix.web.cern.ch/medipix/index.php

[72] D. Pennicard et al., “Design, simulation, production and initial characterisation of 3D silicon detectors,” *Nuclear Instruments and Methods in Physics Research Section A: Accelerators, Spectrometers, Detectors and Associated Equipment*, vol. 598, no. 1, pp. 67 – 70, 2009, instrumentation for Collding Beam Physics Proceedings of the 10th International Conference on Instrumentation for Colliding Beam Physics. [Online]. Available: http://www.sciencedirect.com/science/article/pii/S0168900208011923

[73] D. Pennicard et al, “Charge sharing in double-sided 3D Medipix2 detectors,” *Nuclear Instruments and Methods in Physics Research Section A: Accelerators, Spectrometers, Detectors and Associated Equipment*, vol. 604, no. 1-2, pp. 412 – 415, 2009, PSD8 Proceedings of the 8th International Conference on Position Sensitive Detectors. [Online]. Available: http://www.sciencedirect.com/science/article/pii/S0168900209002058

[74] D. Pennicard et. al., “Radiation Hardness Tests of Double-Sided 3D Detectors,” *Nuclear Science, IEEE Transactions on*, no. 19, 2008.

[75] G. Pellegrini et al., “3-D active edge silicon sensor test results,” 2006, Second Trento Workshop on Advanced Silicon Radiation Detectors. [Online]. Available: http://tredi.itc.it/S

[76] P. Grenier et al., “Test beam results of 3D silicon pixel sensors for the ATLAS upgrade,” *Nuclear Instruments and Methods in Physics Research Section A: Accelerators, Spectrometers, Detectors and Associated Equipment*, vol. 638, no. 1, pp. 33 – 40, 2011. [Online]. Available: http://www.sciencedirect.com/science/article/pii/S0168900211003524

[77] M. Olcese, “3D IBL Sensor Technical Specifications - Technical Specifications and Acceptance Criteria for the 3D Sensors of the ATLAS IBL,” ATLAS project, Geneva, Tech. Rep. CERN ATU-SYS-QC-0004, sept 2011, quality ControlRecord (QC), EDMS Id 1162203. [Online]. Available: https://edms.cern.ch/file/1162203/1/3D_IBL_Sensor_Technical_Specifications.v1.pdf

[78] G.-F. Dalla Betta et al., “Development of 3D-DDTC pixel detectors for the ATLAS upgrade,” *Nuclear Instruments and Methods in Physics Research Section A: Accelerators, Spectrometers, Detectors and Associated Equipment*, vol. 636, no. 1, Supplement, pp. S15 – S23, 2011, <ce:title>7th International “Hiroshima” Symposium on the Development and Application of Semiconductor Tracking Detectors</ce:title>. [Online]. Available: http://www.sciencedirect.com/science/article/pii/S0168900210009332

[79] “Karlsruher Institut für Technologie (KIT) Institut für Experimentelle Kernphysik.” [Online]. Available: http://129.13.102.249/index.php?lang=en

[80] “USBPix Systems, University of Bonn.” [Online]. Available: http://icwiki.physik.uni-bonn.de/twiki/bin/view/Systems/UsbPix

[81] “University of Bonn.” [Online]. Available: http://www3.uni-bonn.de/

[82] J. Schneider, et al., “S3 Multi IO System, S3 Multi IO USB Card Version V1.03,” Universit´at Bonn Physikalisches Institut - Silab, Tech. Rep., Jan 2010, prof. Dr. Norbert Wermes Nußallee 12, 53115 Bonn. [Online]. Available: http://icwiki.physik.uni-bonn.de/twiki/pub/Systems/WebHome/S3_Multi_USB_V1.03_Documentation.pdf

[83] ATLAS Level-1 Trigger Group, *ATLAS level-1 trigger: Technical Design Report*, ser. Technical Design Report ATLAS. Geneva: CERN, 1998.

[84] “Root, cern.” [Online]. Available: http://root.cern.ch/drupal/

[85] “Pixel detector calibration,” 2007, draft v1.0 December 17, 2007. [Online]. Available: https://twiki.cern.ch/twiki/pub/Atlas/PixelDetectorGroup/PixelCalibration_v1_2007_12_17.pdf

[86] P. Morettini, “PixLibScans,” 2011, last update 21 Jun 2006. [Online]. Available: https://twiki.cern.ch/twiki/bin/viewauth/Atlas/PixLibScans

[87] M. Backhaus, “Development of an USB-based test system for the FE-I3 readout chips of the ATLAS pixel detector and Noise Occupancy Studies,” Master’s thesis, Physics Institute of Bonn University, Nussallee 12 53115 Bonn Germany, 2009, thesis. [Online]. Available: http://hep1.physik.uni-bonn.de/fileadmin/Publications/ATLAS_Pixels/Dipl/backhaus_diplomarbeit.pdf

[88] J. Weingarten, “System Test and Noise Performance Studies at The ATLAS Pixel Detector,” Ph.D. dissertation, Bonn Univ., Bonn, 2007, presented on 19 Sep 2007.

[89] “D. Haas Proc of the LCWS2007,” 2007. [Online]. Available: http://www.eudet.org

[90] E. Gschwendtner, “Overview on CERN Test Beam Facilities and Plans for Tests for Non-Collider Experiments,” 2009, cERN, plus MEMORANDUM http://spsschedule.web.cern.ch/SPSschedule/old/request/memo_2.html. [Online]. Available: https://indico.cern.ch/getFile.py/access?contribId=115&sessionId=8&resId=1&materialId=slides&confId=51128

[91] “EUDET - JRA1 - Users Information,” 2011. [Online]. Available: http://www.eudet.org/e13/e21/e727/

[92] “IBL,” November 2011, atlas Upgrade IBL. [Online]. Available: https://twiki.cern.ch/twiki/bin/viewauth/Atlas/IBL

[93] “Root,” 2011. [Online]. Available: http://root.cern.ch/drupal/